

The influence of structure on the electronic properties of π -conjugated systems

Citation for published version (APA):

Ruit, van de, K. (2013). *The influence of structure on the electronic properties of π -conjugated systems*. [Phd Thesis 1 (Research TU/e / Graduation TU/e), Applied Physics and Science Education]. Technische Universiteit Eindhoven. <https://doi.org/10.6100/IR751884>

DOI:

[10.6100/IR751884](https://doi.org/10.6100/IR751884)

Document status and date:

Published: 01/01/2013

Document Version:

Publisher's PDF, also known as Version of Record (includes final page, issue and volume numbers)

Please check the document version of this publication:

- A submitted manuscript is the version of the article upon submission and before peer-review. There can be important differences between the submitted version and the official published version of record. People interested in the research are advised to contact the author for the final version of the publication, or visit the DOI to the publisher's website.
- The final author version and the galley proof are versions of the publication after peer review.
- The final published version features the final layout of the paper including the volume, issue and page numbers.

[Link to publication](#)

General rights

Copyright and moral rights for the publications made accessible in the public portal are retained by the authors and/or other copyright owners and it is a condition of accessing publications that users recognise and abide by the legal requirements associated with these rights.

- Users may download and print one copy of any publication from the public portal for the purpose of private study or research.
- You may not further distribute the material or use it for any profit-making activity or commercial gain
- You may freely distribute the URL identifying the publication in the public portal.

If the publication is distributed under the terms of Article 25fa of the Dutch Copyright Act, indicated by the "Taverne" license above, please follow below link for the End User Agreement:

www.tue.nl/taverne

Take down policy

If you believe that this document breaches copyright please contact us at:

openaccess@tue.nl

providing details and we will investigate your claim.

The Influence of Structure on the Electronic Properties of π -Conjugated Systems

PROEFSCHRIFT

ter verkrijging van de graad van doctor aan de
Technische Universiteit Eindhoven, op gezag van de
rector magnificus, prof.dr.ir. C.J. van Duijn, voor een
commissie aangewezen door het College voor
Promoties in het openbaar te verdedigen
op maandag 15 april 2013 om 16.00 uur

door

Kevin van de Ruit

geboren te Dordrecht

Dit proefschrift is goedgekeurd door de promotor:

prof.dr.ir. R.A.J. Janssen

Copromotoren:

dr.ir. C.F.J. Flipse

en

dr.ir. M. Kemerink

A catalogue record is available from the Eindhoven University of Technology library.

ISBN 979-90-386-3359-6

This research is supported by Nanoned, AGFA-Gevaert and the Holst Centre.

Voor mijn vader die mijn interesse in techniek gewekt heeft.

Contents

1. Introduction:	1
Introduction	2
π -Conjugated Systems	6
Graphene.....	8
PEDOT:PSS	13
Variable Range Hopping	15
This thesis.....	17
2. Giant inelastic tunneling in epitaxial graphene mediated by localized states	23
Introduction	24
Results and Discussion	24
Conclusions	33
Experimental.....	34
3. An STM study: from C₆₀ to graphene formation	37
Introduction	38
Results	39
Conclusions	49
Experimental.....	50
Appendix	51

4. Quasi-one dimensional in-plane conductivity in filamentary films of PEDOT:PSS.....	53
Introduction	54
Results and discussion.....	56
Conclusions	73
Experimental.....	74
Appendix	76
5. The curious out-of-plane conductivity of PEDOT:PSS.....	83
Introduction	84
Results	85
Discussion.....	90
Conclusions	97
Experimental.....	99
Appendix	101
6. A systematic study to universal scaling of the out-of-plane conductivity of thin films of PEDOT:PSS	109
Introduction	110
Results	112
Discussion.....	117
Conclusions	122
Experimental.....	123
Summary	127
Samenvatting.....	131
Curriculum vitae	136
List of publications	137
Dankwoord / acknowledgements.....	138

Chapter 1:

Introduction

Introduction

Functional electronic materials play a major role in shaping everyday life. Probably the most famous functional electronic material is silicon, the material used for computer chips such as shown in Figure 1a. More than 40% of the people in the Netherlands work with computers on a regular basis. Other, lesser known but widespread applications of silicon are the micro-electro-mechanical systems (MEMS) found in most smart phones. They are responsible for many sensors such as the accelerometer that is able to detect the orientation of the smart phone as shown in Figure 1b. A literally more visible and increasingly popular application of silicon is in large area solar cells for rooftop mounting shown in Figure 1c. Although these have recently passed the threshold of being not only ecologically but also economically profitable, the use of silicon in solar cells is not per se evident: because of the indirect band gap optical absorption in silicon is low, and thick high-purity layers are needed to harvest most of the sunlight. Also the band gap is below the optimum for a single-layer solar cell. Light emission from silicon is virtually impossible due to the indirect band gap.¹ Summarizing, its inherent properties make silicon an excellent material for electrical and mechanical applications but less so for opto-electronic applications. Since silicon is an elemental semiconductor, the range over which most of its properties can be tuned is limited.

Carbon-based functional materials have the potential to overcome the limitations of silicon, largely because they are available in many different forms. There many pure, elemental forms or allotropes of carbon: (i) fullerenes (Buckyballs, C_{60}) which have superconducting properties in combination with alkali metals, but are also efficient electron acceptors in organic solar cells; (ii) nanotubes, which come in conducting and semiconducting variants with superior electronic and mechanical properties; (iii) graphene, a one atom thick sheet of carbon, which is both interesting for theory and applications due to its peculiar charge carrier dynamics, causing for instance a high mobility; (iv) graphite, consisting of stacked graphene layers, which are loosely bounded by Van der Waals-forces used in electrodes and batteries; and (v) diamond, a large band gap semiconductor with possible applications in quantum computing. Next to carbon allotropes, there are a limitless different organic, i.e. primarily carbon-based, molecules with special optical or electrical properties. The field of organic chemistry provides an arsenal of ways in which to synthesize and structurally modify organic molecules. This way the properties of these molecules can be fine-tuned to their application. Moreover,

many of these molecules can be solution processed, which can greatly reduce manufacturing costs.

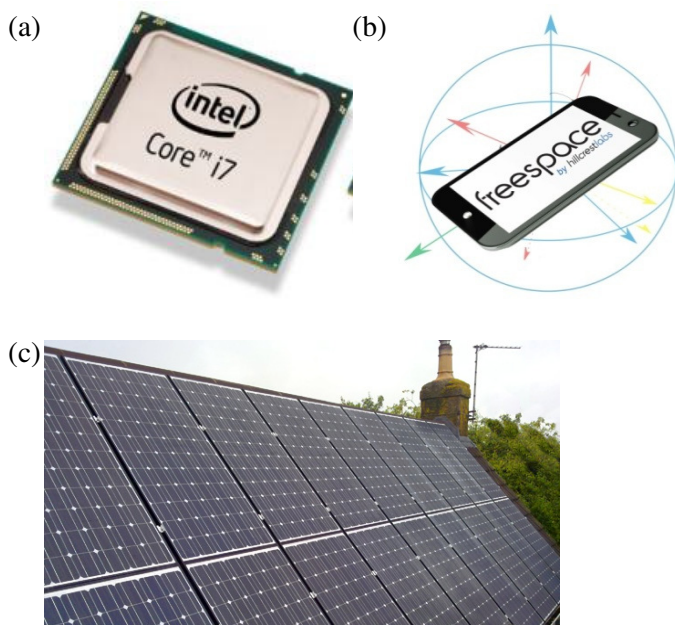


Figure 1. Applications of functional materials and techniques. (a) High speed computing using silicon technology. (b) Sensors and actuators in mobile phones. (c) Silicon solar cells on a rooftop.

Examples of the application of these carbon-based functional materials are shown in Figure 2. Panel (a) shows a high speed transistor using graphene. Due to superior electronic properties, graphene will possibly replace silicon in high-end applications such as computer processors.² Figure 2b shows a loudspeaker, a mechanical electronic application, based on the molecular conducting material poly(3,4-ethylenedioxythiophene):poly(styrenesulfonic acid) (PEDOT:PSS). PEDOT:PSS has also been suggested as a functional material for MEMS, where PEDOT:PSS offers much cheaper processing than the currently most used silicon structures. Figure 2c shows a solar cell located on the roof of a bus stop largely made from organic functional electronic materials. Next to the possibility of solution processing, which reduces the production costs of large area applications, organic solar cells offer the advantage of a tunable band gap. This way optimal use can be made of the spectrum of sunlight. This is especially so for tandem and even triple junction solar cells, which essentially stack two or more sub-cells with different band gaps. Single junction organic solar cells now reach efficiencies

slightly over 10%, but theoretically they can reach 20-25%,³ similar to the efficiency of the single crystalline silicon solar cells shown in Figure 1c.

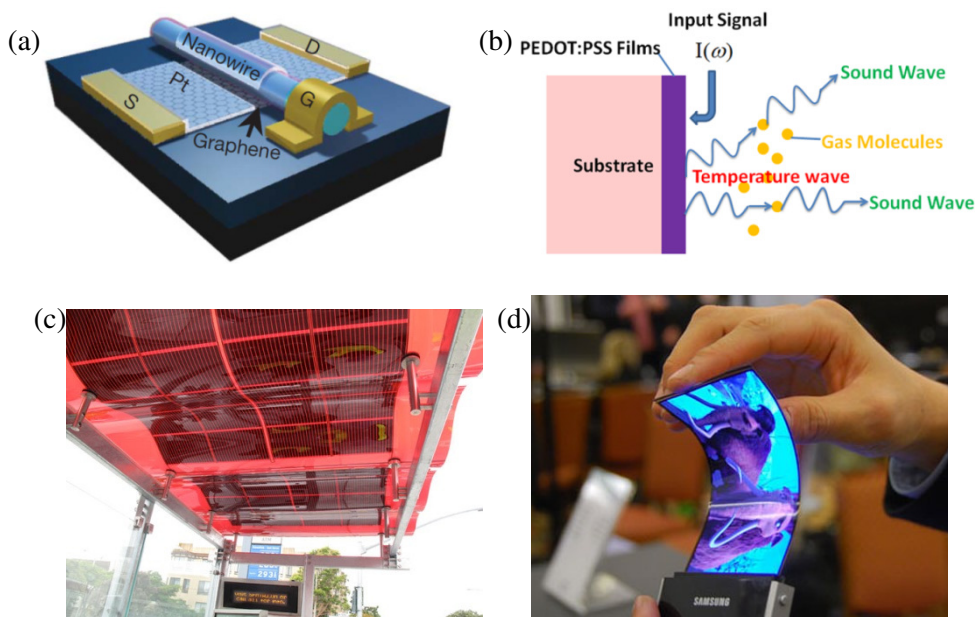


Figure 2. Carbon-based electronic devices. (a) Graphene high-speed transistor.⁸ (b) A simple speaker based on PEDOT:PSS.⁴ (c) Organic Solar cell on a bus stop.⁵ (d) Flexible organic display.⁶

Figure 2d shows a flexible organic light emitting diode (OLED) display. Contrary to computer chips, MEMS and solar cells, silicon's role in display technology has always been very small. Most available displays at the moment are liquid crystal displays (LCD), which operate using liquid crystalline organic materials that switch between transparent and opaque depending on the applied electric field. This technique has the disadvantage that a continuous light source needs to be present behind the LCD. Because of this, energy efficiency is hampered as well as the contrast, since LCDs can never be switched to completely opaque. OLED displays are able to overcome these obstacles since they are built out of arrays of small switchable light sources.

To conclude, the development of new functional electronic materials is crucial to advance the functionality of applications as shown in Figures 1 and 2. For these applications carbon-based materials are considered to have great potential. For different applications, different forms of carbon-based materials have the highest potential. For displays, mainly small molecules play an important role, while for

future solar cells small molecules as well as polymers are possible candidates. Polymers are also proposed for organic MEMS.⁷ These materials have the benefit that many different molecules can be designed on basis of theoretical evaluation or practical experience and can subsequently be synthesized and tested.

In this thesis two carbon-based functional electronic materials are studied: graphene and PEDOT:PSS. Currently graphene is mostly important for fundamental studies due to its special electronic properties. However, graphene also has potential as a functional material, such as the mentioned high speed transistors,^{8,9} as a gas sensor,¹⁰ as a transparent electrode¹¹ for OLEDs and solar cells, and as a resistance standard on basis of the quantum Hall effect.^{12,13} In many ways graphene is the next step following the carbon-based functional materials fullerenes and carbon nanotubes, where graphene offers the advantage of treatments to switch between metallic and semiconducting properties, for instance using hydrogenation.¹⁴

The other carbon based material studied in this thesis, PEDOT:PSS, is a system of two oppositely charged polymers which is both optically transparent and highly conductive. With proper additives it can reach conductivities above $3 \cdot 10^5$ S/m.⁵⁸ Therefore, PEDOT:PSS is particularly useful as a transparent electrode for OLEDs and solar cells, where it offers the advantage of being solution-processable which reduces manufacturing costs for large area applications. Other applications of PEDOT:PSS are its use as active material in electrochromic displays¹⁵, acoustical,⁴ mechanical transducers,⁷ actuators¹⁶, memories,^{17,18} and electrochemical transistors.¹⁹ Additionally, in the study of the conductivity of self-assembled monolayers (SAMs) PEDOT:PSS turned out to be a practical - it severely reduces the number of shorted devices- but also puzzling electrode material.²⁰

This thesis focuses on the influence of the structure on the electronic properties of π -conjugated systems, in this case graphene and PEDOT:PSS. For graphene, two cases are studied, namely graphene on silicon carbide and graphene on platinum. For these two cases there will be a focus on the structure of the interface layer, i.e. the top layer of substrate on which the graphene is grown. For PEDOT:PSS the conductivity is studied as a function of temperature and electric field, which strongly depends on the local structure of this material. The conductivity can be explained using a theory for conductivity in a system of randomly connected conductive elements, in this case PEDOT molecules.

The remainder of this chapter explains the concepts which form the basis of this thesis.

π -Conjugated Systems

The term π -conjugated system is typically used in reference to a class of electronic materials made from carbon. Although many people are aware of the versatile use of carbon in the form of plastics, fewer are aware that similarly easily produced carbon-based materials can be used in opto-electronics. This is probably related to absence of widespread use despite the fact that their (semi-)conducting properties were already discovered in the late 1970's.

The 'trick' to get carbon materials to be (semi-)conductive is related to how the carbon atoms are connected. Carbon has four valence electrons to make such connections. Given that these electrons are close to the positively charged nucleus, they are strongly bound and only able to interact with neighboring atoms by "sharing" an electron. This sharing is known as covalent bonding in which both atoms involved donate an electron to a state formed by the overlap of two orbitals of the neighboring atoms. These bonds are highly directional and for carbon are best described using linear combinations of s and p orbitals called hybridized orbitals. For carbon the two most important sets of hybridized orbitals are sp^2 orbitals, the mechanical building blocks of π -conjugated systems, and sp^3 orbitals, which give diamond its strength. Both are shown in Figures 3a and 3b. The different orbitals for the sp^2 hybridization shown in Figure 3b consist of three σ -orbitals which lay in a single plane with a mutual angle of 120° and a single π -orbital perpendicular to this plane. This hybridization takes place in graphite and graphene, where the three σ -orbitals connect each carbon atom to its three nearest neighbors. No bond is formed in the direction of the π -orbital. The sp^3 hybridization shown in Figure 3a consists of four σ -orbitals with a mutual angle of 109.5° . This hybridization takes place in diamond, where each carbon atom has a neighboring carbon atom in the direction of each of the σ -orbitals.

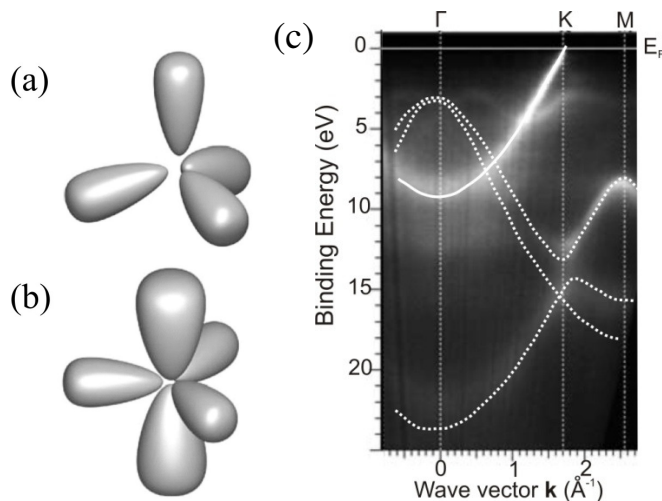


Figure 3. Schematic representation of (a) sp^3 and (b) sp^2 hybridized orbitals.²¹ (c) Band structure of graphene.³⁶ The π -states are highlighted by the continuous white line and the σ -states by the dashed white line.

This hybridization starts playing an important role when the energies of the electronic states are considered. In molecules and ultimately crystals, the electron eigenstates, or states, are linear combinations of the orbitals of the different atoms from which the molecule or crystal is built. This results in many states that extend over the entire molecule or crystal, which for crystals can be indexed by a wavevector, denoted by k . Figure 3c shows a band diagram, i.e. a plot of the energies of different states vs. wavevector, for graphene, measured by angular resolved photo-emission spectroscopy (ARPES). The valence electrons fill up all states below a certain energy called the Fermi energy, E_F . In Figure 3c, the π -states reach up to the Fermi level. The π -states continue directly above the Fermi energy, but the measurement technique used to measure the band structure in Figure 3c cannot show these states. The existence of extended states directly above and below the Fermi energy means that excited states exist at arbitrary small energy differences with respect to the ground state. Because of this, graphene can conduct electricity and is therefore metallic. The σ -states in Figure 3c are far away from the Fermi energy (approximately²² 3.5 eV, see Figure 3c) and therefore play practically no role in the electronic properties of graphene. The σ -states in diamond, although stemming from sp^3 hybridization, display a similar gap at the Fermi energy, which is why diamond cannot be easily used as an electronic material: it is a wide band gap semiconductor.

Summarizing, extended π -states are required to make electronic materials out of carbon. Two of these π -conjugated systems have already been mentioned: graphene and graphite, but there are many more materials in this class, namely any molecule with a backbone of alternating double and single bonded carbon atoms is a π -conjugated system. Since such molecules can be effectively tailored using synthetic chemistry, an immense search for molecular electronic materials is currently going on, yielding materials such as PEDOT:PSS with a conductivity up to $3 \cdot 10^5$ S/m. For comparison, copper has a conductivity of $6 \cdot 10^7$ S/m and the conductivity of graphene used as a transparent electrode reaches $8 \cdot 10^{-3}$ S \square per layer,¹¹ which corresponds to approximately $3 \cdot 10^7$ S/m.

Graphene

Graphene, a one atom thick layer of carbon, has proved itself as a new platform for performing solid state physics. Important advantages of graphene are that it is relatively inert, i.e. basic graphene physics is possible without high vacuum or glove boxes, and that the process of producing flakes of graphene from graphite is cheap and available to most research groups. From a theoretical perspective, graphene has much to offer. Importantly there is simplicity in having just two equivalent π -orbitals in the unit cell which accounts for nearly all of graphene's physics. Furthermore, carbon is in the far top right of the periodic table, where carbon is the material with the largest nucleic charge only screened by 1s electrons, while it is still able to form a solid state at room temperature. Because of this, electrons are tightly bound to the nucleus, and calculations of the electronic properties only need to take into account the overlap between orbitals of neighboring carbon atoms, a method called tight binding. Both the easy preparation as well as the textbook physics makes graphene physics accessible to nearly anyone with a degree in physics.

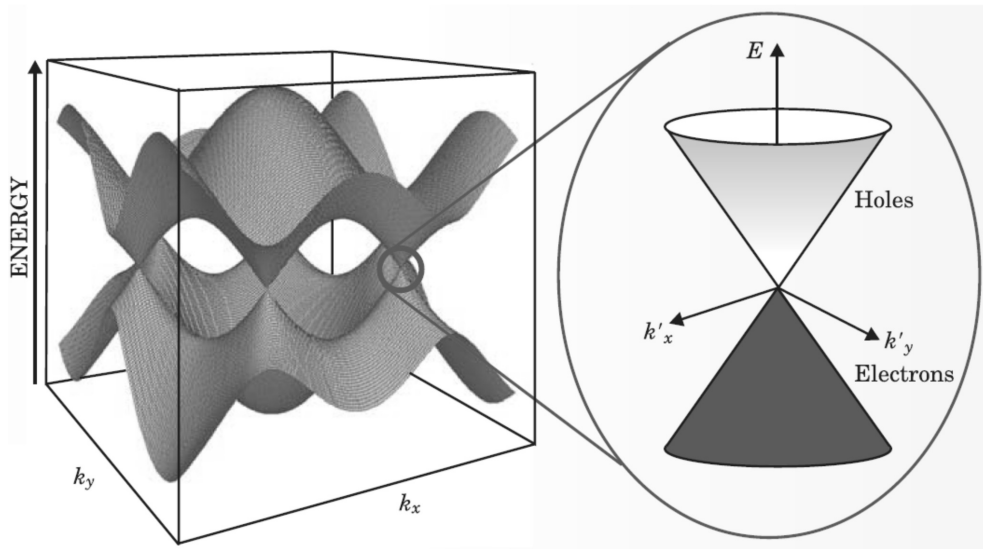


Figure 4. Graphene band structure, where the zoom-in shows the region close to the K point in the Brillouin zone.²³

Central to the physics of graphene is its band structure shown in Figure 4. The Fermi energy is located at the intersection of the two conical parts shown in the zoom-in. Although the left part of Figure 4 shows 6 such cones, due to the periodic symmetry of the Brillouin zone, the cones are threefold degenerate, the two inequivalent cones being called K and K'. Remarkable about the band structure is that the Fermi energy is located at the point in the band structure where the energy dependence on wavevector, k , is highly linear. This means that the group velocity of the electrons does not depend on energy. This is also why electrons in graphene behave similar to photons and are sometimes called massless electrons. In most materials, electrons behave as though they move in a vacuum, i.e. they have a quadratic relation between energy and velocity, albeit with a different 'effective' mass. This property of graphene is therefore special and leads to interesting possibilities such as focusing electrons in a Veselago lens.²⁴ The linear band structure also causes a peculiar tunneling behavior, where the tunneling probability is independent of the width of the barrier. This is called Klein tunneling.²⁵

Based on the same tight binding calculations which resulted in the band structure in Figure 4, another interesting property of graphene can be derived. Namely that the cones in the band structure at K and K' have the special property of having a Berry phase equal to π . In other words, if an external force moves an electron

adiabatically (slow enough to avoid distortions of the phase) in k -space around the K point once, the phase of the electron differs by π from the case if the electron had not moved. This Berry phase can be revealed by applying a magnetic field to the graphene layer so that the resulting Lorentz force causes electrons to move in loops. The quantum mechanical equivalents of such loops are the eigenstates called Landau levels. These Landau levels appear at energies such that the phase going around the loop equals multiples of 2π and sometimes cause oscillations in the conductivity as a function of magnetic field, called Shubnikov-de-Haas oscillations. The Berry phase results in a measurable shift of the positions of the maxima of these conductivity oscillations in as a function of magnetic field for graphene.²⁶

The existence of two inequivalent cones in the dispersion relation adds yet another dimension to the physics of graphene. Whether an electron is located in k -space on the K or K' cone is a conserved quantity, very similar to electrons with spin up and spin down. This leads to the concept of pseudo spin (sometimes called valley spin). In principle, this is not a very special property, since for most systems the k -vector is a conserved quantity. However, the discussed Berry phase of π causes the pseudo spin to be protected against long-wave disorder in graphene.²⁷ Another way of looking at this is that pseudo spin is related to the electron position on the two carbon atoms in the unit cell. Therefore, for disorder to scatter an electrons pseudo spin, the disorder needs to break the symmetry between the equivalent carbon atoms (usually called A and B) within the unit cell. This requires disorder with very short wavelengths. Since backscattering in graphene is related to the pseudo spin switching sign, backscattering in graphene is severely reduced resulting in very high mobilities.^{27,28}

To perform experimental test of these interesting properties on graphene, samples need to be produced. The first of these tests were performed using samples which had been produced by exfoliation of graphene.²⁹ Since graphite is basically a stack of Van Der Waals bonded graphene layers, single graphene layers can easily be extracted by sliding them out. Typically the layers are directly deposited on SiO₂, having the result that the varying local chemical potential of the SiO₂ causes electron and hole-puddles.³⁰ Suspending graphene by etching away the underlying SiO₂ results in much better mobilities,³¹ which illustrates the influence of the substrate. The size and shape of the graphene flakes produced by exfoliation is difficult to control, making this technique difficult to scale up. Alternatives are graphene growth by thermal decomposition of silicon carbide (SiC) or

decomposition of carbon molecules at metal interfaces. Both of these will be discussed in the following paragraphs.

Thermal Decomposition of Silicon Carbide

Epitaxial growth of graphene by thermal decomposition of the SiC(0001) interface is a promising route for creating large area graphene devices. The basic principle to producing graphene in this way is relatively easy and merely involves heating a SiC sample to temperatures around 1200 °C in a vacuum, as shown by an early low energy electron diffraction (LEED) investigation.³² Furthermore, SiC is a well-known material for high temperature / high power electronic devices, which is why high quality SiC wafers are easily available.³³ It is probably for these reasons that epitaxially grown graphene on SiC became the first alternative to exfoliated graphene.³⁴

Since the thermal decomposition of SiC allows macroscopic samples to be produced with large partial areas of graphene, many research techniques which were difficult to apply to exfoliated graphene could be applied. Figure 5a shows the result of an ARPES measurement of graphene on SiC. ARPES is able to directly measure the linear band structure of graphene and could even determine important interactions between charge carriers and collective modes such as phonons and plasmons.³⁵ ARPES has also been used to study the different stages of graphene growth, revealing that before the first layer with graphene properties is formed, another layer called the buffer layer is formed.³⁶ The produced fully conductive samples also allow scanning tunneling microscopy (STM) and spectroscopy (STS). STM reveals that dangling bonds of the SiC are interacting with the graphene layer, which provides a good starting point for analyzing the SiC/graphene interaction.^{37,38,39,40}

Remarkably, STS on graphene on SiC shown in Figure 5b typically reveals a density of states (solid line) that does not correspond to the expected behavior for graphene (dashed line).^{37,38,39,40} A similar observation is made in Refs. 41 and 42 on exfoliated graphene. In those experiments, a gate is used to change the doping level of the graphene, which is related to the position of the minimum in the expected STS, shown in Figure 5b. Independent of the doping, a minimum is observed at the Fermi level ($V = 0$ V in Figure 5b). The strongest mechanism causing this behavior is a phonon mode of the graphene at 63 meV. At voltages higher than 63 mV, i.e. $|V| > 63$ mV, the tunneling electrons are not only able to tunnel in the conventional way, but an additional tunneling channel opens up. Namely, the electron can excite

a phonon during the tunneling process. For graphene this additional channel is highly likely and causes a strong increase in tunneling current away from the Fermi level, leaving a minimum at $V = 0$ V.⁴¹

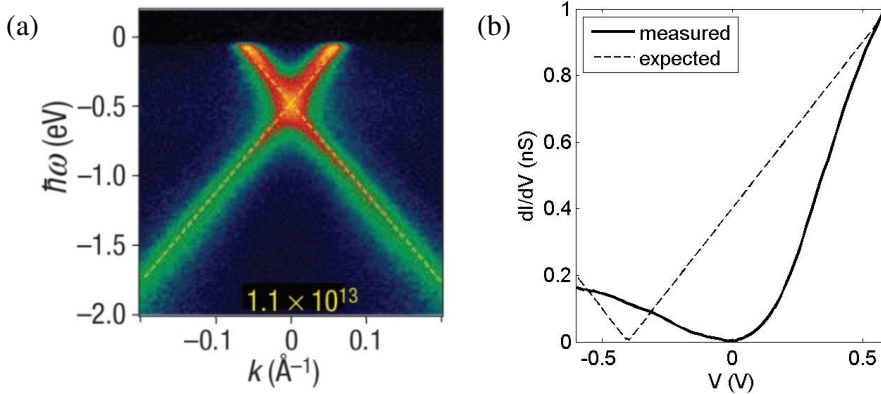


Figure 5. (a) Linear band structure of graphene on SiC(0001) measured by ARPES, revealing a doping by the substrate of $1.1 \cdot 10^{13} \text{ cm}^{-2}$.³⁵ (b) STS measurement on graphene on SiC(0001), showing large differences to the spectrum naively expected based on a) as indicated by the dashed line.

Growth of graphene on SiC in ultra high vacuum (UHV) results in a dense mix of graphene domains with different number of layers.⁴³ To resolve this issue, graphene preparation in argon at atmospheric pressures was shown to lead to domain sizes in the order of $10 \mu\text{m}$.⁴⁴ This resulted in an increase of the mobility to $2000 \text{ cm}^2/\text{Vs}$.⁴⁴ This is still about 100 times lower than for free standing graphene,²⁸ indicating that the effect of the substrate is still substantial for graphene on SiC. Hydrogen intercalation to passivate dangling bonds of the SiC interface has the following remarkable effect on graphene on SiC.⁴⁵ The previously mentioned buffer layer, which normally has a gapped density of states,^{36,38,40} starts showing graphene's linear band structure.⁴⁵ In Chapter 2 of this thesis, a detailed STS study of the interface states and their influence on electron-phonon coupling is presented.

Decomposition of carbon molecules at metal interfaces

Another popular route to large area graphene is graphene growth on a metal surface followed by a transfer of the graphene layer to another, typically insulating substrate.^{11,46,47,48,49,50} To demonstrate the potential of this method, a roll-to-roll process for the production of graphene on arbitrary flexible substrates as discussed in Reference 11 is shown in Figure 6. The resulting layer can be used as a transparent electrode for solar cells, OLEDs, and touch screens and is shown to

have the potential to outperform ITO.¹¹ Even though such an application of graphene is very useful, it cannot be considered to fulfill graphene's full potential. This is related to the limited electronic properties of graphene layers grown at metal interfaces.⁵⁰ The electronic properties are hampered because the typically high number of seeds at the surface during growth results in a graphene layer with a high density of differently oriented domains.⁵⁰

For graphene growth, the Pt(111) surface is of particular interest, since for this surface there is a low interaction between the metal surface and the graphene layer.⁴⁹ The mechanism of interaction can be studied by combining measurements with density functional theory, but this typically requires unit cells with a small number of atoms. The smallest known unit cell for graphene on Pt(111) is the $\sqrt{3}\times\sqrt{3}R30^\circ$ unit cell, which coincides with a particular Pt(111) reconstruction.⁵¹ To obtain the $\sqrt{3}\times\sqrt{3}R30^\circ$ unit cell, large polycyclic aromatic precursors such as C_{60} , or Buckyballs, are shown to give the largest yield.^{51,52} In Chapter 3 of this thesis this interaction is experimentally studied in detail, starting from the structures of the precursor, C_{60} , all the way to graphene formation.

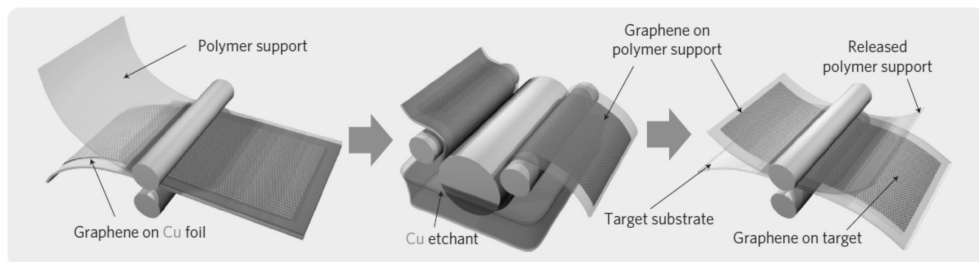


Figure 6. Process steps in the roll to roll process described in Reference 11. After graphene is grown on the copper foil, a polymer support is fixed on top of the graphene layer. The copper is then etched away using an acid, after which the graphene can be transferred to the desired substrate, for instance by a thermal treatment to remove the adhesive force of the polymer support.

PEDOT:PSS

PEDOT, shown at the bottom of Figure 7, is a π -conjugated system because PEDOT contains alternating single and double bonds between the carbon atoms along the chain. Contrary to graphene, PEDOT has a band gap due to the asymmetry between the single and double bonds. Therefore, for PEDOT to become conductive a shift of the Fermi level by making the PEDOT positively charged, is needed through a process called doping. In principle, the presence of such a positive charge can have a detrimental effect on the stability and lifetime of the

polymer. In PEDOT the positive charges are stabilized by the π -donating sulfur and oxygen atoms in the molecule.⁵³ The result is a highly conductive polymeric conductor that is fairly stable under ambient conditions when doped and appears transparent.⁵³

Unfortunately PEDOT itself is insoluble and therefore has to be polymerized in-situ or transferred,⁵⁴ which can be problematic for applications in solar cells and OLEDs. This problem can be solved by polymerizing the EDOT monomers in an aqueous solution of PSS, shown in the top part of Figure 7, which functions as a template. The negatively charged monomers of the PSS act as countercharge to the oxidized EDOT monomers,⁵⁵ as indicated in Figure 7 by the dotted lines. Moreover, since this way the PEDOT is bound to the water soluble PSS, an easy to process microdispersion is formed.⁵⁵

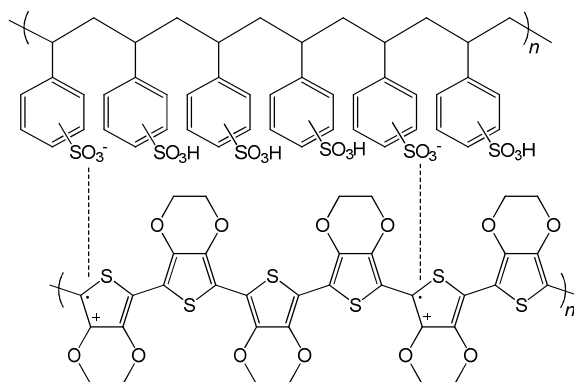


Figure 7: Schematic representation of PEDOT:PSS. PEDOT (below) and PSS (top) bound via the Coulomb attraction between charged monomers of both molecules, indicated by the dashed line.⁵⁶

The first application of PEDOT:PSS in OLEDs and solar cells has been as a hole injection layer on top of another transparent electrode, namely tin-doped indium oxide (ITO).⁵⁷ A major goal for PEDOT:PSS is to replace the ITO layer, which is both expensive and brittle. However, this requires high in-plane conductivities, which is lacking for native PEDOT:PSS ($\sim 10^3$ S/m). To overcome this, high boiling solvents (HBS) are added to the PEDOT:PSS dispersion in water, leading to dramatic improvements in the in-plane conductivity after film formation. Combined with other treatments the conductivity of PEDOT:PSS can reach over $3 \cdot 10^5$ S/m.⁵⁸ The performance of organic solar cells based on PEDOT:PSS with this treatment without ITO is close to that of a similar cell with ITO.⁵⁸

Variable Range Hopping

Charge conduction in PEDOT:PSS differs strongly from the charge conduction in graphene. Although in PEDOT:PSS there is some delocalization of the electronic states along the π -conjugated backbone, they are still localized. Such localization of electronic states stems from the inherent disorder on the microscopic scale,⁵⁹ as can be expected given that the long PSS chains can entangle similar to (al dente) spaghetti. Because of this localization, the Drude model⁶⁰ is no longer applicable, i.e. the charge carriers can no longer be described as having long straight trajectories from which they are occasionally scattered by impurities or vibrations causing resistivity. Instead, in these materials vibrations enable conductivity, as they provide the energy needed to overcome energy differences between neighboring localized states. To calculate the conductivity of such a material, it is necessary to include the statistics of the thermal vibrations and the distribution of electronic states with respect to energy and location. Mott's variable range hopping (VRH) theory⁶¹ takes these aspects into account and is able to explain the conductivity for many disordered systems. In this subsection the concepts of this theory will be explained.

Figure 8 shows a particular realization of localized states which are disordered in energy and space. To calculate the current for such a realization an expression is needed which relates the rate, Γ_{ij} , at which charge carriers hop between two sites, labeled i and j , to the distance between those two localized states and their energy difference. Miller and Abrahams derived such an expression for the rate between two overlapping hydrogen-like orbitals of dopants in a semiconductor, which can be simplified to:^{62,63}

$$\Gamma_{ij} \propto \exp\left[-\frac{r_{ij}}{\xi} - \frac{\Delta E_{ij}}{kT}\right], \quad (1)$$

where r_{ij} is the distance between the sites i and j , ξ the localization length related to the decay length of the state's wavefunction, ΔE_{ij} the simplified⁶³ energy difference, k the Boltzmann constant, and T the temperature. The current between the states i and j can be obtained by multiplying the hopping rate with the charge of the charge carriers in the system. This charge is typically e resulting in the current $I = e \Gamma_{ij}$.

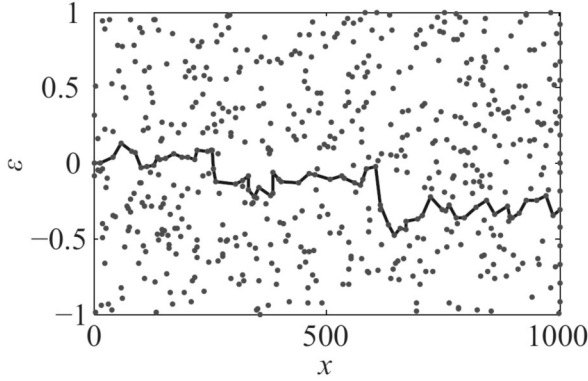


Figure 8. A particular realization of localized states in energy (vertical axis) and space (horizontal axis). The line shows the path of optimal conductivity based on Equation (1).⁶⁴

The line in Figure 8 shows the optimal connection between $x = 0$ and $x = 1000$ for a particular temperature. Typically most hops cross moderate distances and energy differences, but a few hops are much more difficult, such as at $x \approx 600$. Given the exponential dependence in Equation (1), these hops have much lower hopping rate. Therefore the entire conductivity is proportional to the hopping rate of this critical hop. If the optimal path would be constant with temperature, the temperature of the conductivity would therefore have a temperature dependence, i.e. $\sigma \propto \exp[\Delta E_{ij} / kT]$, which is also called activated behavior. Mott's theory, however, shows that the optimal path can be temperature dependent resulting in a much different behavior.

To main question to solve is now: what is the conductivity of the temperature dependent optimal path? Assuming that the entire conductivity is bottle-necked by a critical (lowest) conductivity, or hopping rate Γ_{crit} , the conductivity is simply the lowest critical conductivity for which there exists a connected path between the two electrodes, such that for each hop $\Gamma_{ij} < \Gamma_{\text{crit}}$. For each site i along the connected path there is a certain number of locations r_j and energies E_j such that hopping to such a site j complies with $\Gamma_{ij} < \Gamma_{\text{crit}}$. Naively one could expect a connected path to exist when within the volume defined by r_j and E_j there is on average one other site, or:

$$(\Delta r_{\text{max}})^d \Delta E_{\text{max}} g \approx 1, \quad (2)$$

where g is the density of states per unit energy and volume, d is the number of spatial dimensions, and Δr_{\max} and ΔE_{\max} are the maximum distance and energy difference that still comply with $\Gamma_{ij} < \Gamma_{\text{crit}}$. For a fixed g this equation gives provides $\Delta r_{\max}(\Delta E_{\max})$, inserting in Equation (2) gives $\Gamma = \Gamma(T, \Delta E_{\max})$. Finding the maximum with respect to varying ΔE_{\max} results in:

$$\sigma \propto \Gamma \propto \exp \left[- \left(\frac{T_0}{T} \right)^\alpha \right], \quad (3)$$

where $\alpha = (1+d)^{-1}$ and $T_0 = \beta / (g k \zeta^d)$ is the characteristic temperature with β the correction factor to the naïve Equation (2).

As will be discussed in Chapter 4, the in-plane conductivity in spin-coated films of PEDOT:PSS is well explained by Equation (3) so that the dimensionality of the conducting network can be analyzed. In Chapter 5 the influence of the percolative nature on the out-of-plane charge conduction in thin films of PEDOT:PSS will be discussed. Chapter 6 discusses in detail the temperature en field dependence of the out-of-plane charge conduction.

This thesis

This thesis discusses several π -conjugated systems in which the electronic properties are profoundly influenced by their structure. The studied systems are graphene, which is studied in Chapters 2 and 3, and PEDOT:PSS which is studied in Chapters 4, 5, and 6.

In Chapter 2 an STM and STS study of graphene on SiC is presented. It will be shown that the dangling bonds of the interface structure strongly affect the observed topography of graphene on SiC in STM as well as the observed spectroscopy in STS. Moreover in the neighborhood of structural defects in the graphene layer, electron-phonon coupling is severely enhanced.

In Chapter 3 the formation of graphene by the decomposition of C_{60} on Pt(111) is studied. It is shown that a subsurface missing platinum atom structure can be identified by combining STM and electronic structure calculations. It is revealed that subsurface missing platinum atom structures are already present before C_{60} decomposition and are related to the near-instability of the Pt(111) surface.

In Chapter 4 the in-plane conductivity of thin PEDOT:PSS films is studied as a function of temperature. Curiously the result is best described by quasi-1D VRH. Two independent measurements, namely a study of the conductivity variation for different PEDOT:PSS ratios and a transmission electron microscopy study, reveal that the observed quasi-1D VRH behavior is a consequence of the filamentary structure of PEDOT:PSS micelles in the film.

In Chapter 5 the out-of-plane conductivity of similar PEDOT:PSS thin films is studied, revealing a surprisingly strong dependence of conductivity on the layer thickness. This dependence is explained on basis of the structure of the percolating conduction network.

In Chapter 6 the field and temperature dependence of the out-of-plane conductivity of PEDOT:PSS are studied, revealing a power law dependence of conductivity on both field and temperature. The power-law dependence is studied for varying PEDOT:PSS ratios and varying device areas. The results are discussed in the context of recent theoretical work for thin quasi-1D systems, which therefore takes into account the local structure of the PEDOT:PSS system.

References

- ¹ This is not the case for all crystalline semiconductors. For example, GaAs has a direct bandgap and can be used for LED applications.
- ² S. Hertel, D. Waldmann, J. Jobst, A. Albert, M. Albrecht, S. Reshanov, A. Schöner, M. Krieger, H. B. Weber, *Nat. Commun.* **2012**, *3*, 957.
- ³ R. A. J. Janssen, J. Nelson, *Adv. Mater.* doi: 10.1002/adma.201202873
- ⁴ H. Tian, D. Xie, Y. Yang, T.-L. Ren, T.-T. Feng, Y.-F. Wang, C.-J. Zhou, P.-G. Peng, L.-G. Wang, L.-T. Liu, *Appl. Phys. Lett.* **2011**, *99*, 233503.
- ⁵ Bus stop in San Francisco: http://www.interiordesign.net/article/474238-Bus_Stops_by_Lundberg_Design_and_3Form_Generate_Power_for_San_Francisco.php
- ⁶ <http://androidheadlines.com/2012/09/featured-not-bendable-yet-samsung-amoled-displays-delayed-for-general-market.html>
- ⁷ U. Lang, P. Rust, J. Dual, *Microelectron. Eng.* **2008**, *85*, 1050.
- ⁸ L. Liao, Y.-C. Lin, M. Bao, R. Cheng, J. Bai, Y. Liu, Y. Qu, K. L. Wang, Y. Huang, X. Duan, *Nature* **2010**, *467*, 305.
- ⁹ M. E. Ramón, A. Gupta, C. Corbet, D. A. Ferrer, H. C. P. Movva, G. Carpenter, L. Colombo, G. Bourianoff, M. Doczy, D. Akinwande, E. Tutuc, S. K. Banerjee, *ACS Nano* **2011**, *5*, 7198.
- ¹⁰ F. Schedin, A. K. Geim, S. V. Morozov, E. W. Hill, P. Blake, M. I. Katsnelson, K. S. Novoselov, *Nat. Mater.* **2007**, *6*, 652.
- ¹¹ S. Bae, H. Kim, Y. Lee, X. Xu, J.-S. Park, Y. Zheng, J. Balakrishnan, T. Lei, H. R. Kim, Y. I. Song, Y.-J. Kim, K. S. Kim, B. Özyilmaz, J.-H. Ahn, B. H. Hong, S. Iijima, *Nat. Nanotech.* **2010**, *5*, 574.
- ¹² A. Tzalenchuk, S. Lara-Avila, A. Kalaboukhov, S. Paolillo, M. Syväjärvi, R. Yakimova, O. Kazakova, T. J. B. M. Janssen, V. Fal'ko, S. Kubatkin, *Nat. Nanotechn.* **2010**, *5*, 186.
- ¹³ A. J. M. Giesbers, G. Rietveld, E. Houtzager, U. Zeitler, R. Yang, K. S. Novoselov, A. K. Geim, J. C. Maan, *Appl. Phys. Lett.* **2008**, *93*, 222109.
- ¹⁴ A. Castellanos-Gomez, M. Wojtaszek, Arramel, N. Tombros, B. J. van Wees, *Small* **2012**, *8*, 1607.
- ¹⁵ J. Kawahara, P. A. Ersman, I. Engquist, M. Berggren, *Org. Electron.* **2012**, *13*, 469.
- ¹⁶ D. S. H. Charrier, R. A. J. Janssen, M. Kemerink, *Chem. Mater.* **2010**, *22*, 3670.
- ¹⁷ S. Möller, C. Perlov, W. Jackson, C. Taussig, S. R. Forrest, *Nature* **2003**, *426*, 166.
- ¹⁸ B. C. de Brito, E. C. P. Smits, P. A. van Hal, T. C. T. Geuns, B. de Boer, C. J. M. Lasance, H. L. Gomes, D. M. de Leeuw, *Adv. Mater.* **2008**, *20*, 3750.
- ¹⁹ D. Khodagholy, M. Gurfinkel, E. Stavrinidou, P. Leleux, T. Herve, S. Sanaur, G. G. Malliaras, *Appl. Phys. Lett.* **2011**, *99*, 163304.
- ²⁰ P. A. V. Hal, E. C. P. Smits, T. C. T. Geuns, H. B. Akkerman, B. C. D. Brito, S. Perissinotto, G. Lanzani, A. J. Kronemeijer, V. Geskin, J. Cornil, P. W. M. Blom, B. D. Boer, D. M. D. Leeuw, *Nat. Nanotech.* **2008**, *3*, 749.
- ²¹ S. Schols, *Device Architecture and Materials for Organic Light-Emitting Devices: Targeting High Current Densities and Control of the Triplet Concentration*; Springer, 2011.
- ²² A. Bostwick, K. Emtsev, K. Horn, E. Huwald, L. Ley, J. McChesney, T. Ohta, J. Riley, E. Rotenberg, F. Speck, T. Seyller, In *Advances in Solid State Physics*; Haug, R., Red.; Advances in Solid State Physics; Springer Berlin / Heidelberg, 2008; Vol. 47, pp. 159–170.

- ²³ M. Wilson, *Physics Today* **2006**, 59, 21.
- ²⁴ V. V. Cheianov, V. Fal'ko, B. L. Altshuler, *Science* **2007**, 315, 1252.
- ²⁵ M. I. Katsnelson, K. S. Novoselov, A. K. Geim, *Nat. Phys.* **2006**, 2, 620.
- ²⁶ Y. Zhang, Y.-W. Tan, H. L. Stormer, P. Kim, *Nature* **2005**, 438, 201.
- ²⁷ T. Ando, T. Nakanishi, R. Saito, *J. Phys. Soc. Jpn.* **1998**, 67, 2857.
- ²⁸ X. Du, I. Skachko, A. Barker, E. Y. Andrei, *Nat. Nanotech.* **2008**, 3, 491.
- ²⁹ K. S. Novoselov, A. K. Geim, S. V. Morozov, D. Jiang, Y. Zhang, S. V. Dubonos, I. V. Grigorieva, A. A. Firsov, *Science* **2004**, 306, 666.
- ³⁰ J. Martin, N. Akerman, G. Ulbricht, T. Lohmann, J. H. Smet, K. von Klitzing, A. Yacoby, *Nat. Phys.* **2008**, 4, 144.
- ³¹ X. Du, I. Skachko, A. Barker, E. Y. Andrei, *Nat. Nanotech.* **2008**, 3, 491.
- ³² A. J. Van Bommel, J. E. Crombeen, A. Van Tooren, *Surf. Sci.* **1975**, 48, 463.
- ³³ M. Willander, M. Friesel, Q. Wahab, B. Straumal, *J. Mater. Sci.: Mater. El.* **2006**, 17, 1.
- ³⁴ C. Berger, Z. Song, T. Li, X. Li, A. Y. Ogbazghi, R. Feng, Z. Dai, A. N. Marchenkov, E. H. Conrad, P. N. First, W. A. de Heer, *J. Phys. Chem. B* **2004**, 108, 19912.
- ³⁵ A. Bostwick, T. Ohta, T. Seyller, K. Horn, E. Rotenberg, *Nat. Phys.* **2007**, 3, 36.
- ³⁶ K. V. Emtsev, T. Seyller, F. Speck, L. Ley, P. Stojanov, J. D. Riley, R. C. G. Leckey, *Mater. Sci. Forum* **2007**, 556-557, 525.
- ³⁷ V. W. Brar, Y. Zhang, Y. Yayon, T. Ohta, J. L. McChesney, A. Bostwick, E. Rotenberg, K. Horn, M. F. Crommie, *Appl. Phys. Lett.* **2007**, 91, 122102.
- ³⁸ J. Červenka, K. van de Ruit, C. F. J. Flipse, *Phys. Rev. B* **2010**, 81, 205403. See also, Chapter 2 of this thesis.
- ³⁹ P. Lauffer, K. V. Emtsev, R. Graupner, T. Seyller, L. Ley, S. A. Reshanov, H. B. Weber, *Phys. Rev. B* **2008**, 77, 155426.
- ⁴⁰ G. M. Rutter, N. P. Guisinger, J. N. Crain, E. A. A. Jarvis, M. D. Stiles, T. Li, P. N. First, J. A. Stroscio, *Phys. Rev. B* **2007**, 76, 235416.
- ⁴¹ Y. Zhang, V. W. Brar, F. Wang, C. Girit, Y. Yayon, M. Panlasigui, A. Zettl, M. F. Crommie, *Nat. Phys.* **2008**, 4, 627.
- ⁴² V. W. Brar, S. Wickenburg, M. Panlasigui, C.-H. Park, T. O. Wehling, Y. Zhang, R. Decker, Ç. Girit, A. V. Balatsky, S. G. Louie, A. Zettl, M. F. Crommie, *Phys. Rev. Lett.* **2010**, 104, 036805.
- ⁴³ T. Ohta, F. El Gabaly, A. Bostwick, J. L. McChesney, K. V. Emtsev, A. K. Schmid, T. Seyller, K. Horn, E. Rotenberg, *New J. Phys.* **2008**, 10, 023034.
- ⁴⁴ K. V. Emtsev, A. Bostwick, K. Horn, J. Jobst, G. L. Kellogg, L. Ley, J. L. McChesney, T. Ohta, S. A. Reshanov, J. Röhl, E. Rotenberg, A. K. Schmid, D. Waldmann, H. B. Weber, T. Seyller, *Nat. Mater.* **2009**, 8, 203.
- ⁴⁵ C. Riedl, C. Coletti, T. Iwasaki, A. A. Zakharov, U. Starke, *Phys. Rev. Lett.* **2009**, 103, 246804.
- ⁴⁶ T. Kato, R. Hatakeyama, *Nat. Nanotech.* **2012**, 7, 651.
- ⁴⁷ X. Li, W. Cai, J. An, S. Kim, J. Nah, D. Yang, R. Piner, A. Velamakanni, I. Jung, E. Tutuc, S. K. Banerjee, L. Colombo, R. S. Ruoff, *Science* **2009**, 324, 1312.
- ⁴⁸ A. Reina, X. Jia, J. Ho, D. Nezich, H. Son, V. Bulovic, M. S. Dresselhaus, J. Kong, *Nano Lett.* **2009**, 9, 30.
- ⁴⁹ M. Gao, Y. Pan, L. Huang, H. Hu, L. Z. Zhang, H. M. Guo, S. X. Du, H.-J. Gao, *App. Phys. Lett.* **2011**, 98, 033101.

- ⁵⁰ Q. Yu, L. A. Jauregui, W. Wu, R. Colby, J. Tian, Z. Su, H. Cao, Z. Liu, D. Pandey, D. Wei, T. F. Chung, P. Peng, N. P. Guisinger, E. A. Stach, J. Bao, S.-S. Pei, Y. P. Chen, *Nat. Mater.* **2011**, *10*, 443.
- ⁵¹ G. Otero, C. González, A. L. Pinardi, P. Merino, S. Gardonio, S. Lizzit, M. Blanco-Rey, K. Van de Ruit, C. F. J. Flipse, J. Méndez, P. L. de Andrés, J. A. Martín-Gago, *Phys. Rev. Lett.* **2010**, *105*, 216102.
- ⁵² P. Merino, M. Svec, A. L. Pinardi, G. Otero, J. A. Martín-Gago, *ACS Nano* **2011**, *5*, 5627.
- ⁵³ G. Heywang, F. Jonas, *Adv. Mater.* **1992**, *4*, 116.
- ⁵⁴ F. Jonas, L. Schrader, *Synth. Met.* **1991**, *41*, 831.
- ⁵⁵ S. Kirchmeyer, K. Reuter, *J. Mater. Chem.* **2005**, *15*, 2077.
- ⁵⁶ L. Groenendaal, F. Jonas, D. Freitag, H. Pielartzik, J. R. Reynolds, *Adv. Mater.* **2000**, *12*, 481.
- ⁵⁷ S. A. Carter, M. Angelopoulos, S. Karg, P. J. Brock, J. C. Scott, *Applied Physics Letters* **1997**, *70*, 2067.
- ⁵⁸ Y. Xia, K. Sun, J. Ouyang, *Adv. Mater.* **2012**, *24*, 2436.
- ⁵⁹ P. W. Anderson, *Phys. Rev.* **1958**, *109*, 1492.
- ⁶⁰ P. Drude, *Ann. Phys.* **1900**, *306*, 566–613.
- ⁶¹ N. F. Mott, E. A. Davis, *Electronic Processes in Non-Crystalline Materials*; Clarendon Press, 1979.
- ⁶² B. I. Shklovskii, A. L. Éfros, *Electronic properties of doped semiconductors*; Springer-Verlag, 1984.
- ⁶³ Equation (1) stems from Equation (4.2.32) in Reference 62, where the localization length $\zeta = 2a$, with a the effective Bohr-radius and $\Delta E_{ij} = \varepsilon_{ij} = \frac{1}{2} (|\varepsilon_i - \varepsilon_j| + |\varepsilon_i - \mu| + |\varepsilon_j - \mu|)$, where ε_i and ε_j are the energy levels at sites i and j and μ is the chemical potential.
- ⁶⁴ A. S. Rodin, M. M. Fogler, *Phys. Rev. B* **2009**, *80*, 155435.

Chapter 2:

Giant inelastic tunneling in epitaxial graphene mediated by localized states

Abstract

Local electronic structures of nanometer-sized patches of epitaxial graphene and its interface layer with SiC(0001) have been studied by atomically resolved scanning tunneling microscopy and spectroscopy. Localized states belonging to the interface layer of a graphene/SiC system show to have essential influence on the electronic structure of graphene. Giant enhancement of inelastic tunneling, reaching 50% of the total tunneling current, has been observed at the localized states on a nanometer-sized graphene monolayer surrounded by defects.

Published as:

J. Červenka, K. van de Ruit, C. F. J. Flipse, *Phys. Rev. B* **2010**, *81*, 205403.

Introduction

Epitaxially grown graphene on SiC offers one of the most promising platforms for applications in high-speed electronic devices that might replace silicon in future.¹ However, the quality of the two-dimensional (2D) electron gas in epitaxial graphene on SiC still falls behind the electronic quality of mechanically exfoliated graphene.^{1,2} While the maximum charge-carrier mobility of epitaxial graphene on SiC(0001) is in the order of $1000 \text{ cm}^2/\text{Vs}$ at room temperature,² the mobility reaches 2 orders of magnitude higher values in exfoliated graphene.³ Therefore a great deal of interest is focused on the understanding the differences between the electronic structure of exfoliated and epitaxial graphene and the consequences for potential applications. Since the crystallographic quality of both graphene layers seems to be equivalent,² the interaction with the substrate remains the biggest unknown. This is mainly because of the complicated structure and electronic properties of the carbon-rich graphene/SiC interface layer, which is situated between the top of the SiC and the first layer which behaves as graphene.^{4,5,6}

In this chapter, we present a local study of electronic and vibrational properties of nanometer-sized areas of a graphene monolayer grown on SiC(0001) and its $6\sqrt{3} \times 6\sqrt{3} R30^\circ$ interface layer by scanning tunneling microscopy (STM). Local scanning tunneling spectroscopy (STS) and inelastic electron-tunneling spectroscopy (IETS) measurements have revealed unexpected phenomena in epitaxial graphene that could not be observed in spatially averaged measurements, which are usually reported in literature. Localized states of the interface layer protruding through the first graphene layer have caused giant enhancement of inelastic tunneling of electrons from graphene particularly on the places with localized electron states of the graphene/SiC interface layer. The inelastic phonon contribution for the out-of-plane graphene acoustic phonon at 70 mV has reached a gigantic 50% of the total tunneling current. Our work reveals an unusual process of inelastic tunneling, which is principally different from previously reported phonon-mediated tunneling in mechanically cleaved graphene placed on SiO_2 .⁷

Results and Discussion

Figure 1 shows spatially averaged STS curves on 0 interface, first, and second graphene layers on SiC, which are usually presented as local electronic structures of these layers.⁴ Even though the STS measurements have been obtained on areas with very small sizes (10–20 nm) that were surrounded by many large structural defects, they show comparable results to STS results reported by other groups on

better quality graphene samples.^{4,9} However, averaging of STS curves is not appropriate in disordered systems such as the graphene/SiC(0001) system because it mixes incorrectly the local density of states (LDOS) at different locations. We illustrate this in Figure 2 by a series of atomically resolved STM images of a first graphene layer taken at different bias voltages. At low bias voltages (± 50 mV), the characteristic graphene atomic structure together with the larger $6\sqrt{3} \times 6\sqrt{3} R30^\circ$ superstructure are visible, indicating a single graphene layer on SiC(0001).^{4-6,9} However, when the bias voltage is increased, bright dots start to appear until they fully dominate the STM pictures at higher voltages. Owing to these bias-dependent topographic features, an average of STS spectra becomes bias dependent, and therefore it does not reflect correctly an average of LDOS.

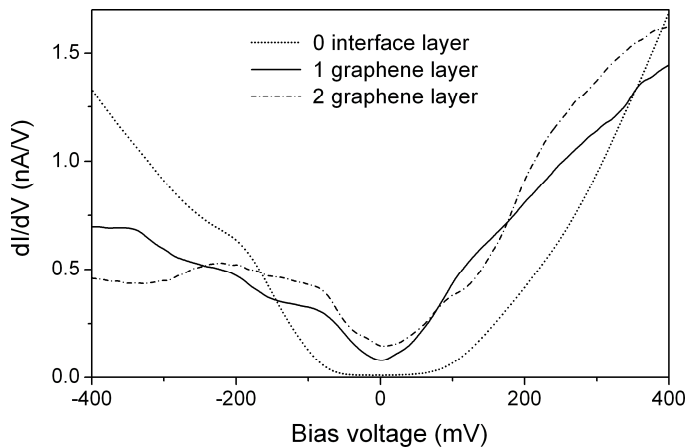


Figure 1. Spatially averaged STS curves on the 0 interface, first and second graphene layers on SiC(0001). Scanning parameters: $V = -200$ mV, $I = 50$ pA for graphene monolayer and bilayer, and $V = -200$ mV, $I = 5$ pA for the 0 layer.

The observed disordered bright features do not originate from the graphene layer but from the underlying interface layer as has been previously discussed by Rutter et al.⁴ Graphene thus shows transparency at higher bias voltages to bright features from the lower interface layer in STM. Although the bright features in the zero interface layer seem to be disordered on local scale, they manifest the $6\sqrt{3} \times 6\sqrt{3} R30^\circ$ reconstruction with respect to the SiC crystal on larger scales as confirmed by large scale STM images and low-energy electron diffraction (LEED).^{5,6} Interestingly, the positions of bright features are not the same in the filled and the empty states as symbolized by crosses and circles in Figures 2c and 2d. Circles and crosses point out the positions of the bright features in the filled

states (-200 mV) and in the empty states (200 mV), respectively. Local STS measurements on top of these features on a graphene monolayer have revealed clear localized electron states at -200 , -500 , and 500 mV (see Figure 2e). On the other hand, STS spectra measured on regions with a graphene character (no bright features are observed in STM) have not shown any peaks in the LDOS. Similar localized states as on the first graphene layer have also been measured on bright features in the zero interface layer by STS in Figure 2f. The carbon-rich interface layer has semiconducting properties with a 400 meV gap pinned in between the ± 200 mV localized states in accordance with previous STS measurements.⁴ The spatial extension of these localized states is in the order of 0.5 nm.

The origin of the localized states in the interface layer has been suggested to be either due to stem from Si-C bonds and Si dangling bonds in the interface layer consisting of covalently bonded graphene layer to the SiC(0001) surface^{10,11}. Alternatively a Si adatoms structure on top of the last SiC layer has been suggested.⁴ Both models propose correctly formation of localized states close to the Fermi energy. However, the first model is supported by angle-resolved photoelectron spectroscopy (ARPES) studies on interface and graphene layers on SiC(0001) (References. 10 and 12) and by transferring of monolayer graphene to bilayer graphene after decoupling of the interface layer by H_2 intercalation.¹³ In ARPES, the first graphene layer displayed well-developed graphene π bands extending up to the Fermi level; the interface layer exhibited semiconducting properties with absent π bands.¹⁰ Two localized states at the binding energies 0.5 and 1.6 eV have been identified in the carbon-rich interface layer with the $6\sqrt{3}\times 6\sqrt{3}R30^\circ$ reconstruction on the SiC(0001).¹⁰ Also the formation of empty electron states close to Fermi energy with a localized character has been observed in the graphitization study of SiC(0001) surface in inverse photoelectron spectroscopy.¹⁴ The localized states at ± 200 meV have not been identified in the photoemission experiments most probably because of their low intensities. Surprisingly, their energy coincides with a kink at 200 meV observed in the π band dispersion near the K point of monolayer graphene, whose origin has been suggested to be related to either electron-electron or electron-phonon interactions.^{15,16}

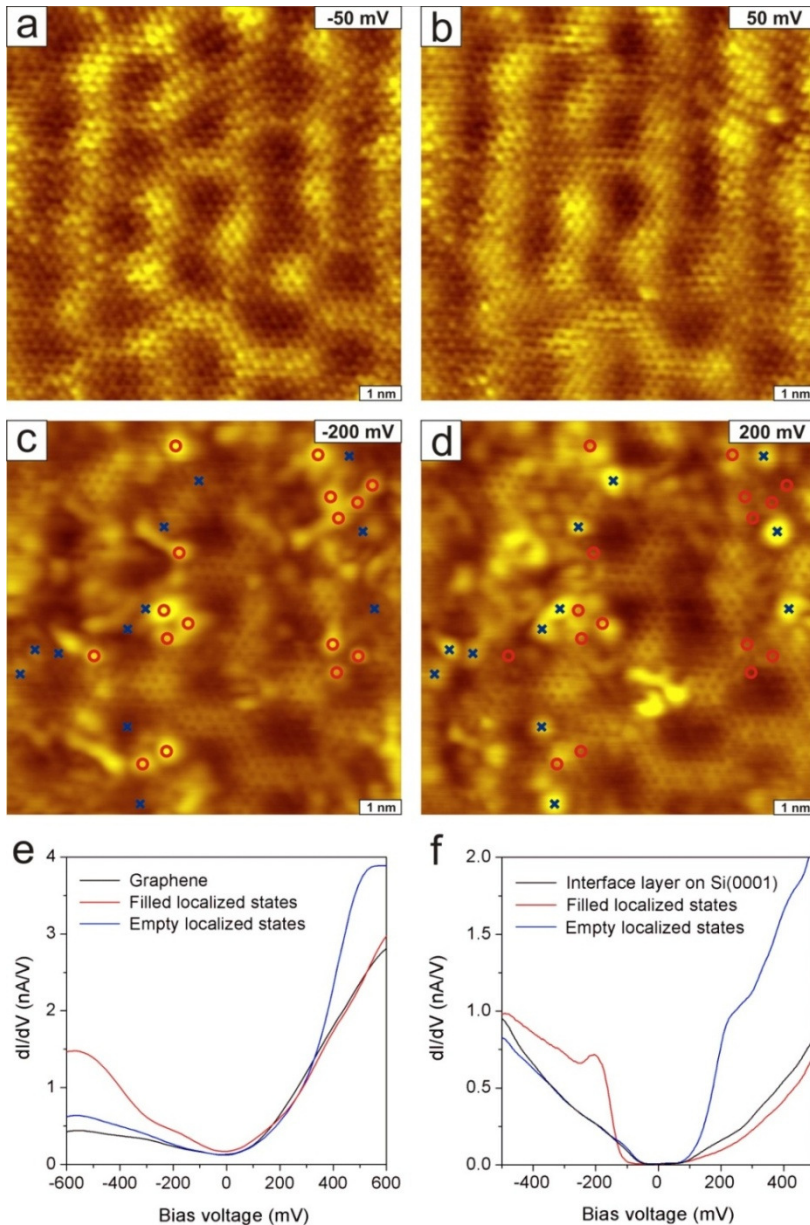


Figure 2. STM images of a 10×10 nm² area on single-layer graphene on SiC(0001) taken with $I = 5$ pA and (a) $V = -50$, (b) 50, (c) -200 , and (d) 200 mV. Circles point out the positions of the bright dots in the filled states and crosses in the empty states. (e) Three local characteristic dI/dV spectra on monolayer graphene on SiC(0001) ($V = 300$ mV and $I = 41$ pA). (f) Three local characteristic dI/dV spectra on the interface layer on SiC(0001) ($V = -200$ mV and $I = 5$ pA). All STS curves have been averaged over ten curves.

STS spectra of graphene monolayers and bilayers display an unexpected gap-like feature at the Fermi level (see Figure 1 or Reference 9). From a tight-binding fit to photoemission data,⁶ however, one would not expect such a gap-like feature in STS because of the electron doping, which causes a shift of the Dirac point (the minimum in the graphene DOS) to -0.45 and -0.32 eV for monolayer and bilayer graphene layers, respectively.¹⁶ Also transport experiments suggest a higher electron density on a monolayer graphene on SiC (References. 1 and 2) than on exfoliated graphene placed on SiO₂, where the Dirac point is in the vicinity of the Fermi energy.^{7,17} Recently the appearance of a gap-like feature at the Fermi level on exfoliated graphene supported on a silicon oxide surface has been explained by the inability to tunnel into the π states due to a small tunneling probability at the Fermi level.⁷ This has been overcome by the assistance of a phonon at 63 meV coupled with σ states, which made the tunneling possible at energies higher than the phonon energy.⁷ The experimental findings of Zhang et al. have been supported by theoretical modeling of Wehling et al.¹⁸

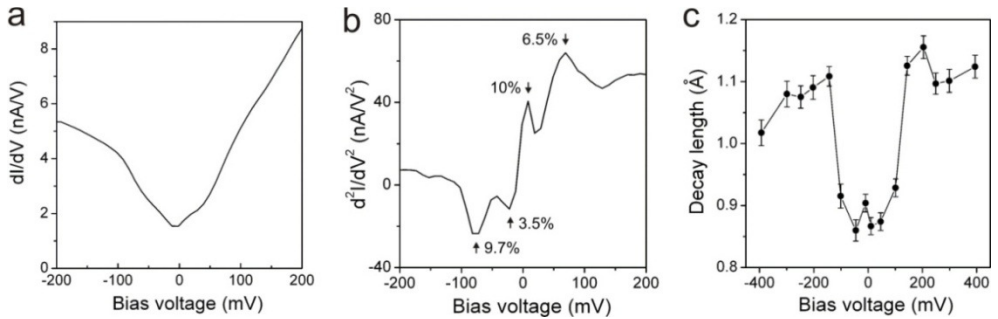


Figure 3. Spatially averaged (a) dI/dV and (b) d^2I/dV^2 (b) spectra taken on the graphene monolayer on SiC(0001) shown in Figure 4, and its tunnel current decay length λ as a function of bias voltage (c). An inelastic peak intensity $\Delta\sigma/\sigma$ is indicated at each attributed phonon peak in d^2I/dV^2 . Scanning parameters: 64×64 grid, $V = 50$ mV, and $I = 70$ pA. The decay lengths have been determined from $I(z)$ spectroscopy at fixed bias voltage by fitting it by an exponential function $I(z) = \exp(-z/\lambda)$. Error bars represent standard deviations of the measurements.

In Figure 3b, we show the observation of phonon contributions in IETS on a nanometer-sized monolayer graphene on SiC(0001). The inelastic tunneling features are observed as peaks (or dips) in the second derivative of current with respect to the voltage at the threshold where the electron energy associated with the bias voltage matches the oscillator energy. The dI/dV and d^2I/dV^2 spectra in Figure 3 have been spatially averaged over 4096 points. Four inelastic peaks corresponding to out-of-plane acoustic graphene phonons at 16 and 70 mV can

been identified in the d^2I/dV^2 spectrum on a graphene monolayer. Similar phonon modes at 16 and 58 mV have been found on graphite in IETS before.¹⁹ Phonon induced inelastic tunneling in single molecules deposited on metal surfaces typically leads to conductivity changes in the order of only $\Delta\sigma/\sigma \approx 1\%$,²⁰ where the normalized change in differential conductance $\Delta\sigma/\sigma$ is obtained by normalizing the peak area in d^2I/dV^2 to conductance. The inelastic peak intensities in monolayer graphene on SiC are $\Delta\sigma/\sigma \approx 10\%$ for both phonon contributions at 16 and 70 mV (Figure 4). Surprisingly, the tunneling conductivity changed by a much larger factor 13 outside the gap-like feature on the exfoliated graphene.⁷ This has been explained by a different mechanism based on the phonon-mediated tunneling process which involves momentum-conserving virtual transitions between 2D electron bands in graphene.

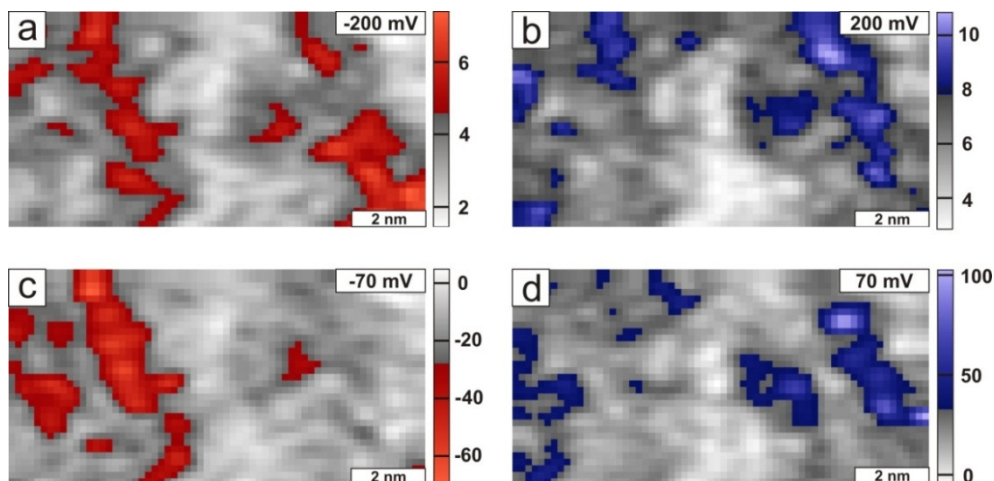


Figure 4. (a) and (b) dI/dV and (c) and (d) d^2I/dV^2 maps at constant bias voltage indicated in the right top corner of a $12 \times 8 \text{ nm}^2$ area on graphene monolayer on SiC(0001). Red regions indicate high intensity inelastic phonon contributions at -70 mV and high dI/dV at -200 mV and blue regions mark out high intensity d^2I/dV^2 at 70 mV and dI/dV at 200 mV . Scanning parameters: $V = 50 \text{ mV}$ and $I = 50 \text{ pA}$.

The mechanism of the phonon-assisted tunneling in exfoliated graphene was supported by observation of bias dependent wave-function spatial decay rates, where the tunnel decay length inside and outside the gap has been observed to be 0.25 and 0.45 \AA , respectively.⁷ Bias dependent wave-function spatial decay rates in monolayer graphene grown on SiC are depicted in Figure 4c. The decay length λ has been determined from $I(z)$ spectroscopy performed at fixed bias voltage V by fitting it to an exponential function $I(z) = \exp(-z/\lambda)$. Similarly like on exfoliated

graphene, two different decay rates have been observed inside and outside the gap-like feature bounded in the ± 100 mV region, $\lambda_{\text{IN}} = 0.89 \text{ \AA}$ and $\lambda_{\text{OUT}} = 1.1 \text{ \AA}$.

Although the results measured on epitaxial graphene in Figure 3 look similar to the data by Zhang et al. measured on exfoliated graphene,⁷ the mechanism is different. First, both out-of-plane acoustic phonon contributions at 16 and 70 mV have similar intensities but only the latter phonon can assist the virtual tunneling to σ electrons since it has the right momentum because it is centered at the K/K' points, whereas the other out-of-plane acoustic phonon at 16 mV cannot play the same role because it is located at the Γ point. Second, the tunneling decay rates are observed to change exactly at the edge of the gap of the interface layer (see Figure 3), whose states are known to have a large spatial extension since they are seen in STM even upon formation of two graphene layers above the SiC interface. Finally, the most important fact that disproves the phonon-assisted tunneling in epitaxial graphene on SiC is a spatially inhomogeneous character of the inelastic contribution.

To illustrate the spatial dependence of inelastic tunneling intensity, we show simultaneously measured dI/dV and d^2I/dV^2 maps on a graphene monolayer on SiC(0001) in Figure 4. The d^2I/dV^2 images depict intensities of the inelastic peak contribution of the phonon mode at ± 70 mV, and the dI/dV maps portray intensities of the localized states at ± 200 mV. The places of the high inelastic peak intensity coincide with the places where the ± 200 mV localized states are observed in the dI/dV maps. For this reason, high intensity regions in Figure 4 have been highlighted by red and blue color in negative and positive bias voltages, respectively, to highlight the correlation between $dI/dV(\pm 200 \text{ mV})$ and $d^2I/dV^2(\pm 70 \text{ mV})$ maps.

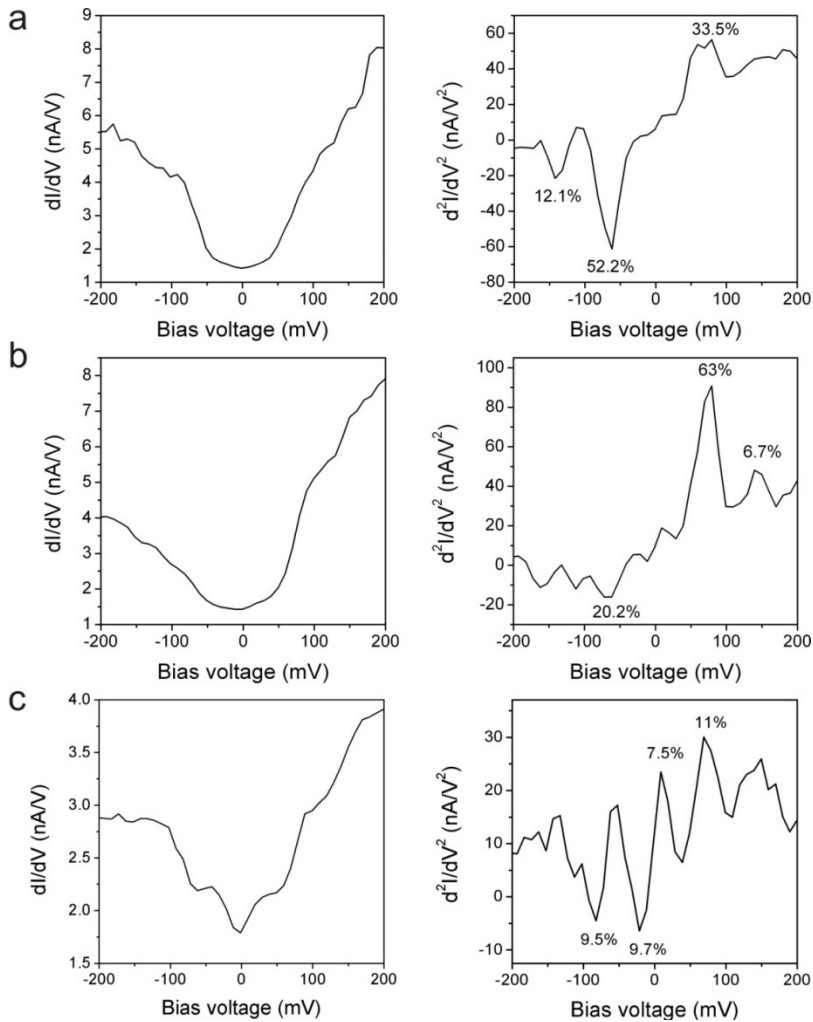


Figure 5. dI/dV and d^2I/dV^2 spectra on graphene monolayer on SiC taken at $V = 50$ mV and $I = 50$ pA. The spectra represent typical individual dI/dV and d^2I/dV^2 curves obtained in (a) red regions, (b) blue regions, and (c) gray regions in Figure 4. Inelastic peak intensities $\Delta\sigma/\sigma$ are indicated at the each attributed phonon peak in d^2I/dV^2 .

The IETS peak intensities vary spatially by a large factor in d^2I/dV^2 maps, up to 50 among some places, as seen by the difference between the values of red/blue and gray regions. The regions with high IETS intensities are found at different locations in positive and negative bias voltage, similar to the bright features in Figure 1. This inhomogeneous asymmetry can be also seen on three characteristic local dI/dV and d^2I/dV^2 spectra depicted in Figure 5. These spectra have been averaged only over ten local measurements; therefore, they exhibit a larger noise

level in comparison to the spatially averaged IETS spectra. An IETS curve measured on a position with a high IETS intensity at -70 mV (Figure 5a) shows a gigantic inelastic feature reaching $\Delta\sigma/\sigma \approx 50\%$ in negative bias voltage, while the IETS peak in positive voltage is half of this size. Such high IETS signals have been observed predominantly at positions with high dI/dV intensities at -200 mV. These places most probably correspond to the localized states at -200 mV on the first and zero graphene layers. Moreover, a second-harmonic phonon mode at -140 mV is observed in d^2I/dV^2 with an intensity approximately five times smaller than the intensity of the first harmonic mode. Similar results have been observed on places with a high inelastic peak at $+70$ mV that are located at position with a high dI/dV at 200 mV, implying a connection with localized states of the graphene monolayer in the empty states. In this case, an enormous first-order inelastic peak together with the second-harmonic contribution have been observed in the positive bias voltage. On the other hand, IETS spectra obtained on locations free of localized states (Figure 5c) have demonstrated relatively low intensity phonon contributions (10%) for both 16 and 70 mV out-of-plane phonons. No second-order phonon modes could be seen in these IETS spectra. It is important to note that one should be careful in relating the high intensity dI/dV regions at ± 200 mV with localized states since an increase in dI/dV can also be caused by high intensity IETS peaks at ± 70 mV. However, since the presence of localized states have also been independently proven by other STM groups on a monolayer graphene,⁹ it is highly probable that high intensity dI/dV correlates with localized states at ± 200 mV originating in the graphene/SiC(0001) interface layer.

Typical inelastic tunneling experiments give rise to phonon fingerprints that reach only a few percent of the total tunneling current; however, we observe unexpectedly giant signals as high as 50% in the presence of localized states. This could indicate a strong electron-phonon coupling strength (λ), but calculations by Park et al.²¹ have shown values for λ in the order of 0.05 at 200 meV binding energy. This relative small value cannot explain the large IETS intensity. The fact that the large IETS intensities coincide with the positions of sharp localized electron states at ± 200 mV is supported by the DFT calculation results of Atta-Fynn et al.²² In this study, localized electron states stemming from defects or topological disorder exhibited an anomalously large electron-phonon coupling.²² Hence, the observed localized states probably enhance the electron-phonon coupling, resulting in a larger IETS intensity. However, the presence of localized states might not be the only criterion of giant IETS contributions because the

IETSs have been measured on a very small graphene regions (10–20 nm) confined among many structural defects. Therefore, there seem to be two conditions for the giant enhancement of the IETS data: both the influence of the localized states at ± 200 mV and the presence of structural defects. The structural defects are known to play a very important role in the scattering of electrons, which is an additional contribution for localization, thus causing together with localized states an anomalously large electron-phonon coupling.

In addition, in the dI/dV spectra, higher harmonics are observed equidistantly spaced with the value of the vibration. Higher harmonics so-called phonon (vibrational) side bands have been observed occasionally in scanning tunneling experiments in the resonant tunneling regime.²³ The conditions for resonant tunneling are discussed in detail by Galperin et al.:²⁴ the higher order vibronic levels become visible if the tunneling electron stays relatively long on the molecule compared to the dephasing time and the localized electron state coincides with a vibration level. This happens if the chemical interaction between electron state and molecule is relatively small, resulting in a narrow broadening of the vibronic level.²⁴ As is shown, at ± 200 mV, localized electron states can couple with the out-of-plane phonons from graphene.

Because the dI/dV data do not show periodic phonon peaks equidistantly around ± 200 mV, the resonant tunneling channel is not related to the localized states at ± 200 mV. Resonant tunneling through localized states at the Fermi level is difficult to determine because of the pseudogap, but it would be highly probable if the origin of the pseudogap is of many-body character, characterized by electron-electron and electron-phonon interactions.²⁵

Conclusions

In conclusion, a giant inelastic tunneling process has been observed in epitaxial graphene on SiC(0001) in scanning tunneling experiments. The inelastic tunneling channel reached half of the total tunneling current. The mechanism of the giant tunneling is connected with the presence of sharp localized states originating in the interface with SiC and strong electron-phonon coupling in graphene near a structural defect.

Experimental

The growth of atomically thin graphene samples was carried out in situ in ultrahigh vacuum (UHV) on n-type 6H-SiC(0001) by thermal decomposition of Si at elevated temperatures. The growth process has been done on a homebuilt electron-beam heater according to the preparation method described elsewhere.⁸ The sample temperature has been monitored by a pyrometer using emissivity 0.9. Owing to inhomogeneous heating of the sample by the e-beam heater, a mixture containing very small atomically flat areas (10–20 nm) of graphene mono-, bi-, and interface layers has been produced as confirmed by LEED and STM. Scanning tunneling microscopy experiments were performed in an Omicron GmbH low temperature (LT)-STM setup, working under UHV conditions (10^{-11} mbar) at 5 K. Electrochemically etched W tips were used in the constant current STM mode. STS and IETS have been obtained by using two lock-in amplifiers and superimposing an alternating voltage reference signal with a frequency 990 Hz and amplitude 10 mV to the bias voltage applied to the sample.

References

- ¹ C. Berger, Z. Song, X. Li, X. Wu, N. Brown, C. Naud, D. Mayou, T. Li, J. Hass, A. N. Marchenkov, E. H. Conrad, P. N. First, W. A. de Heer, *Science* **2006**, *312*, 1191.
- ² K. V. Emtsev, A. Bostwick, K. Horn, J. Jobst, G. L. Kellogg, L. Ley, J. L. McChesney, T. Ohta, S. A. Reshanov, J. Röhrl, E. Rotenberg, A. K. Schmid, D. Waldmann, H. B. Weber, T. Seyller, *Nat. Mater.* **2009**, *8*, 203.
- ³ S. V. Morozov, K. S. Novoselov, M. I. Katsnelson, F. Schedin, D. C. Elias, J. A. Jaszczak, A. K. Geim, *Phys. Rev. Lett.* **2008**, *100*, 016602.
- ⁴ G. M. Rutter, N. P. Guisinger, J. N. Crain, E. A. A. Jarvis, M. D. Stiles, T. Li, P. N. First, J. A. Stroscio, *Phys. Rev. B* **2007**, *76*, 235416.
- ⁵ C. Riedl, U. Starke, J. Bernhardt, M. Franke, K. Heinz, *Phys. Rev. B* **2007**, *76*, 245406.
- ⁶ P. Lauffer, K. V. Emtsev, R. Graupner, T. Seyller, L. Ley, S. A. Reshanov, H. B. Weber, *Phys. Rev. B* **2008**, *77*, 155426.
- ⁷ Y. Zhang, V. W. Brar, F. Wang, C. Girit, Y. Yayon, M. Panlasigui, A. Zettl, M. F. Crommie, *Nat. Phys.* **2008**, *4*, 627.
- ⁸ C. Berger, Z. Song, T. Li, X. Li, A. Y. Ogbazghi, R. Feng, Z. Dai, A. N. Marchenkov, E. H. Conrad, P. N. First, W. A. de Heer, *J. Phys. Chem. B* **2004**, *108*, 19912.
- ⁹ V. W. Brar, Y. Zhang, Y. Yayon, T. Ohta, J. L. McChesney, A. Bostwick, E. Rotenberg, K. Horn, M. F. Crommie, *Appl. Phys. Lett.* **2007**, *91*, 122102.
- ¹⁰ K. V. Emtsev, F. Speck, T. Seyller, L. Ley, J. D. Riley, *Phys. Rev. B* **2008**, *77*, 155303.
- ¹¹ J. Červenka, K. van der Ruit, K. Flipse, *physica status solidi (a)* **2010**, *207*, 595.
- ¹² T. Ohta, A. Bostwick, T. Seyller, K. Horn, E. Rotenberg, *Science* **2006**, *313*, 951.
- ¹³ C. Riedl, C. Coletti, T. Iwasaki, A. A. Zakharov, U. Starke, *Phys. Rev. Lett.* **2009**, *103*, 246804.
- ¹⁴ I. Forbeaux, J.-M. Themlin, J.-M. Debever, *Phys. Rev. B* **1998**, *58*, 16396.
- ¹⁵ A. Bostwick, T. Ohta, T. Seyller, K. Horn, E. Rotenberg, *Nat. Phys.* **2007**, *3*, 36.
- ¹⁶ T. Ohta, A. Bostwick, J. L. McChesney, T. Seyller, K. Horn, E. Rotenberg, *Phys. Rev. Lett.* **2007**, *98*, 206802.
- ¹⁷ K. S. Novoselov, A. K. Geim, S. V. Morozov, D. Jiang, M. I. Katsnelson, I. V. Grigorieva, S. V. Dubonos, A. A. Firsov, *Nature* **2005**, *438*, 197.
- ¹⁸ T. O. Wehling, I. Grigorenko, A. I. Lichtenstein, A. V. Balatsky, *Phys. Rev. Lett.* **2008**, *101*, 216803.
- ¹⁹ L. Vitali, M. A. Schneider, K. Kern, L. Wirtz, A. Rubio, *Phys. Rev. B* **2004**, *69*, 121414.
- ²⁰ B. C. Stipe, M. A. Rezaei, W. Ho, *Science* **1998**, *280*, 1732.
- ²¹ C.-H. Park, F. Giustino, M. L. Cohen, S. G. Louie, *Nano Lett.* **2008**, *8*, 4229.
- ²² R. Atta-Fynn, P. Biswas, D. A. Drabold, *Phys. Rev. B* **2004**, *69*, 245204.
- ²³ X. H. Qiu, G. V. Nazin, W. Ho, *Phys. Rev. Lett.* **2004**, *92*, 206102.
- ²⁴ M. Galperin, A. Nitzan, M. A. Ratner, *Phys. Rev. B* **2006**, *73*, 045314.
- ²⁵ B. L. Altshuler, A. G. Aranov, *JETP* **1979**, *50*, 968.

Chapter 3:

An STM study: from C₆₀ to graphene formation

Abstract

We report on the full pathway from room temperature deposition of C₆₀ on Pt(111) to the formation of graphene at high temperatures. Using in-situ low temperature scanning tunneling microscopy (STM), a submonolayer of C₆₀ on Pt(111) is studied after heating steps at increasing temperatures. We are able to identify the molecular orientations of the C₆₀ molecules at each step. Changes in the apparent height of C₆₀ molecules in combination with a change in their orientation show that C₆₀ molecules adopt a subsurface missing-atom configuration. By studying the graphene layer formed upon an additional high temperature heating step, both by STM and density functional theory (DFT) calculations, we show that $\sqrt{3} \times \sqrt{3} R30^\circ$ domains of the formed graphene layer are also in a subsurface missing-atom configuration. By studying in detail the steps towards these subsurface missing-atom configurations, additional factors are revealed that can help explain how this system overcomes the large energy barriers associated with vacancy formation on the Pt(111) surface.

Introduction

The interaction between large molecules and metal surfaces plays an important role in molecular electronics. The C₆₀/metal interface serves as a prototype system for such interactions.¹ Experimental and *ab initio* theoretical studies have already uncovered several details of the C₆₀/Pt(111) system.^{1,2,3,4,5,6,7,8,9,10} After a heat treatment of approximately 400 °C, the C₆₀/Pt(111) system adopts either a $\sqrt{13}\times\sqrt{13}R13.9^\circ$ or a $2\sqrt{3}\times\sqrt{3}R30^\circ$ reconstruction, in which the C₆₀ molecules are located over a platinum vacancy^{1,5} (a schematic representation is shown in Figure 1). We will refer to this configuration as the C₆₀ missing subsurface platinum atom (C-MSPA) configuration. An additional heat treatment to 700 °C leads to decomposition and conversion of the C₆₀ molecules into graphene in domains with random orientations.^{2,3,11,12} This conversion has raised technological interest for graphene production.¹³ Among these domains is the $\sqrt{3}\times\sqrt{3}R30^\circ$ reconstruction which adopts a graphene missing subsurface platinum atom (G-MSPA) configuration⁹.

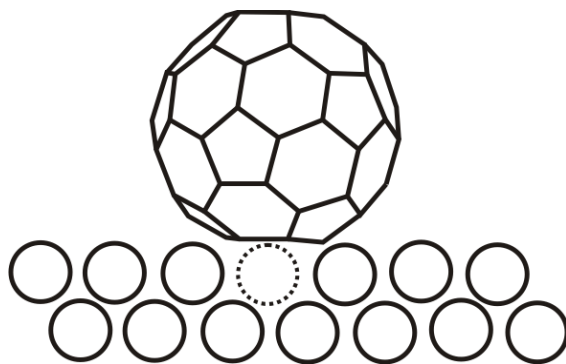


Figure 1. Schematical representation of a C₆₀ molecule(top) on top of a Pt(111) surface (bottom). The dotted circle denotes the position where a Pt atom is missing.

In spite of the rich physics of the C₆₀/Pt(111) system, only a few articles^{2,3,7} study how this system evolves under heat treatments at increasing temperatures. Here we study in detail the structural organization of the C₆₀ on Pt(111) system by low temperature scanning tunneling microscopy (STM) after applying heat treatments at increasing temperatures. As compared to previous work⁷ we report changes in apparent height of C₆₀ molecules that are related to the C-MSPA configuration and that appear to persist up to the high temperatures at which graphene is formed. We show that the transition towards the C-MSPA configuration nucleates at the edges of C₆₀ islands and that the Pt(111) surface away from the islands undergoes a

reconstruction, which remains after graphene formation. These observations may serve as important hints for how the system overcomes the energy barriers for vacancy formation in the Pt(111) surface, both in the C-MSPA and in the G-MSPA configuration.

Results

Figure 2 shows topographic STM images after deposition of C_{60} at room temperature. Figure 2a shows a stepped Pt(111) surface, where the lines extending from the image indicate the step edge directions. The arrow in the figure indicates the direction towards lower step edges. Deposition of C_{60} results in island growth at the lower side of the steps, in agreement with Reference 7 and 14. The C_{60} molecules in the islands are arranged hexagonally in two different orientations, as indicated by the dashed and dotted lattice vectors. From data discussed below the orientations will be determined to have formed a $\sqrt{13}\times\sqrt{13}R13.9^\circ$ structure in four possible, symmetric configurations. Using the same data, the orientation of the Pt(111) lattice has been determined, as shown in the bottom left corner of Figure 2b. The apparent height of all C_{60} molecules in the islands is the same and measured to be 0.60 nm. Figure 2b shows a small scale image of a C_{60} island. The C_{60} molecules appear in two different shapes: dumbbells and stripes, indicated by the dotted lines and dotted circles, respectively. Analogous to Reference 15 the bright features in the C_{60} shape are attributed to pentagons in the C_{60} cage. This relates the striped shape to a C_{60} molecule with a pentagon on top, and the dumbbell shape to a C_{60} molecule with a 6-6 bond on top, i.e. a bond which connects two hexagons in the C_{60} cage. Given the expected five-fold symmetry of the pentagon orientation, it is difficult to interpret their orientation relative to the Pt(111) lattice. The dumbbells have a two-fold symmetry, and two rotations can be observed at an approximate 60° angle. The long axis of the shapes is the direction of the 6-6 bond at the bottom of the C_{60} , which for all dumbbell shapes is aligned to the Pt(111) lattice (shown in the bottom left corner).

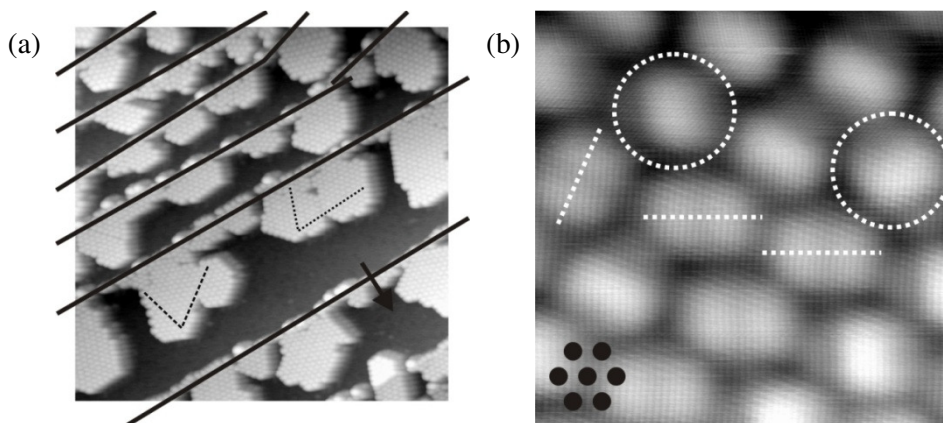


Figure 2. STM images obtained directly after deposition at room temperature. (a) A large scale topographic image (70 nm x 70 nm, 2.0 V, 20 pA) which shows several steps of the Pt(111) surface. Lines at the edge of the Figure highlight the step edges and the arrow in the Figure shows the direction in which the steps go down. The dashed and dotted lines indicate the hexagonal lattice vectors for two islands with different orientation. (b) A small scale topographic image (4 nm x 4 nm, 2.0 V, 20 pA) showing the orbital shape of the C₆₀ molecules in an island. Dotted circles have been drawn which highlight the stripe shaped orbitals. White dotted lines have been drawn along the long axis of the dumb-bell shaped orbitals and the stripe shaped orbitals respectively. The dots at the bottom left show the positions of atoms of the Pt(111) lattice.

Figure 3 shows C₆₀ on Pt(111) after a 280 °C heat treatment. The most obvious change after the heat treatment is the appearance of C₆₀ with a lower apparent height, determined to be 0.45 nm. These C₆₀ molecules appear dim in Figure 3a. Most of the dim molecules are highlighted by the white dotted square. Some dim molecules appear away from the edges, as highlighted by the black dotted circles. The top right of Figure 3a shows a zoom-in of the area highlighted by the white dotted square. The shapes of nearly all the dim C₆₀ appear to be triangles, as shown by the two black dotted example triangles. The points of the triangles point in the direction of the Pt(111) lattice vectors, shown as white arrows. Moreover, the triangles point slightly away from their nearest neighbors. This is in full agreement with the C-MSPA configuration determined by XRD in Reference 5. Combined with the observation of a low apparent height, we can conclude that these molecules are indeed in the C-MSPA configuration. Since at room temperature all molecules have an apparent height of 0.6 nm and are randomly oriented, we conclude that a transition took place from a molecular configuration with an unreconstructed Pt(111) surface to the C-MSPA configuration. The transition towards the C-MSPA configuration takes place most at the edge of the island in Figure 3. This indicates that the energetic barrier for the formation of the

configuration is lower at the edges of the C_{60} islands. Since the dim molecules appear not just at random locations at the edge of an island, but few molecule domains, suggests that the barrier is also lowered in the vicinity of a C_{60} molecule which is in the C-MSPA configuration.

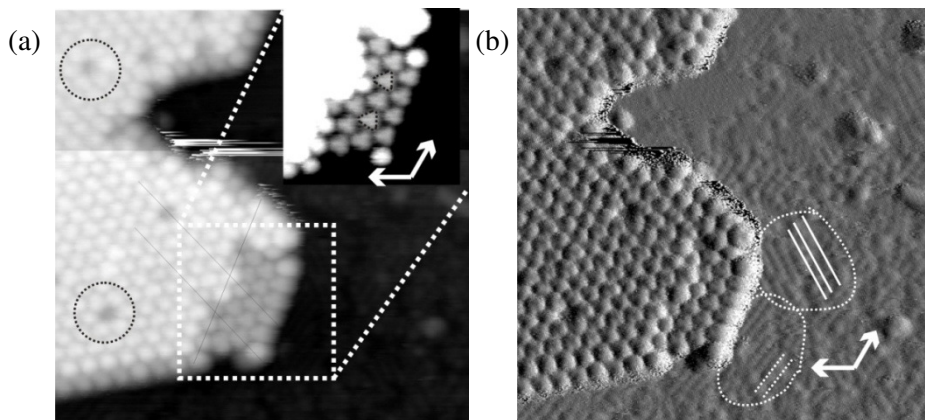


Figure 3. A C_{60} island after a 280 °C heat treatment imaged in a) STM topography and b) STM current (25.0 nm x 25.0 nm, 2.7 V, 95 pA). In both images the direction of the Pt(111) lattice vectors is shown using white arrows. In (a) black dotted circles show the location of dim molecules away from the edge of the islands. The white dotted square shows a location which contains many dim molecules at the edge of the island. The zoom in of this area, shown in the top right of the image, shows that these molecules have triangular shapes, some of which are highlighted by the black dotted triangles. In (b) dotted regions with continuous and striped lines indicate different domains of the Pt(111) surface reconstruction with a different orientation. The lines in the indicated regions highlight the striped pattern in these domains.

The molecules that did not undergo a change in apparent height show up as bright molecules. Nearly all have an apparent height of 0.6 nm. Unfortunately the present images do not allow relating them to particular molecular orientation. Below we will discuss the shapes of the bright molecules in more detail. However, we can exclude that the bright molecules form a second layer on top of the dim molecules: the locations of the bright and dim molecules appear at the same lattice locations, as indicated by the thin black lines. For spherical molecules, a second layer forms in the hollow sites of the first layer, as shown for the C_{60} on Pt(111) system in Reference 9. Since the bright molecules have the same location relative to the lattice as the dim molecules, we conclude that the dim and bright molecules are in the same (single) layer.

In the current image in Figure 3b a pattern is observed on the Pt(111) surface. The pattern appears in domains of different orientation. Two of these domains have been highlighted by dotted and continuous lines. In both domains, the pattern appears to be striped. Comparing the direction of the stripes to the Pt(111) lattice direction shown using the white arrows, indicates that the stripes follow lattice vectors of the Pt(111) surface. The pattern appears to be a reconstruction of the Pt(111) surface. Unfortunately it was not possible to determine the exact reconstruction of the patches; the patches are too small and exact lateral length scales and angles are difficult to measure using STM. The corrugation is close to 20 pm, which may explain why this reconstruction has not yet been reported in literature. However, a reconstruction of the Pt(111) surface into an amorphous phase, where the surface layer acquires a higher density, has been reported to occur¹⁶ above 1200 °C. Further modeling of the Pt(111) surface has led to the conclusion that the Pt(111) is only just stable and that the Pt(111) surface will reconstruct in the presence of a large number of adatoms. The reconstruction formed in the presence of the adatoms is expected to be strongly dependent on the various intrinsic and extrinsic parameters of the adlayer. This explains why the reconstruction observed in Figure 3b is different from those observed so far.¹⁷

Figure 4 shows topographic images obtained after subsequent heating to 330 °C. Figure 4a shows an island which has formed at the lower side of the step edge indicated by the lines outside the image. This island is in many aspects similar to that observed in Figure 3a. Dim molecules appear at the edge of the island, and isolated dim molecules appear away from the edges as indicated by the dotted circles. A difference is that this island shows a region of dim molecules away from the edge of the island, as indicated by the dash-dotted line. Furthermore next to dim molecules (apparent height 0.45 nm) and bright molecules (apparent height 0.60 nm), there appear to be molecules which have a higher apparent height of 0.65 nm. These are the extra bright molecules indicated by the solid ellipse.

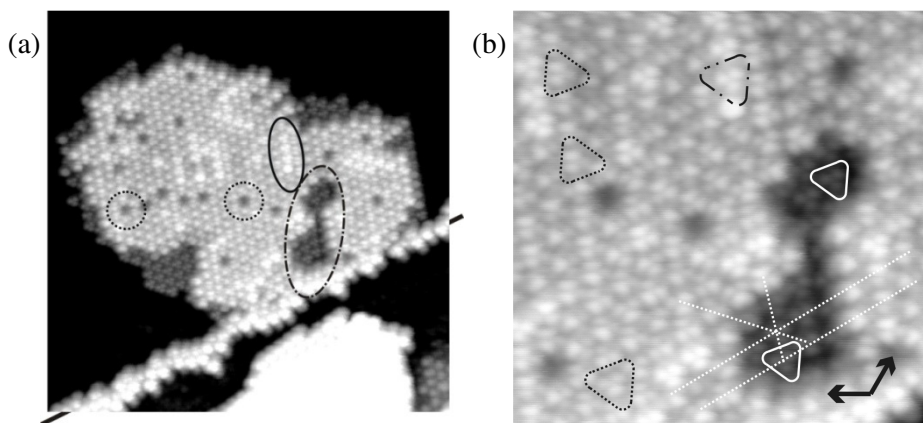


Figure 4. A C_{60} island after a 330 °C heat treatment imaged in STM topography: (a) (40 nm x 40 nm, 2.5 V, 132 pA) and a zoom in (b) (15 nm x 15 nm, 2.5 V, 132 pA). In (a) the lines extending out of the image indicate a step of the Pt(111) surface. The dotted circles indicated dim molecules away from the edges of the islands. The dot-dashed ellipse shows a region of dim molecules away from the island edges. The continuous ellipse indicates a row of extra bright molecules. In (b) the shape of one of these extra bright molecules is highlighted by the black dash-dotted triangle. Black dotted triangles highlight the a1/a2 shapes of the bright molecules. White continuous triangles highlight the triangular orientation of the dim molecules. The white dotted lines indicate the C_{60} lattice, to show that the bright molecules do not appear at shifted lattice positions with respect to the dim molecules, as expected for a bilayer. The black arrows at the bottom right indicate the Pt(111) lattice vectors.

We will now discuss the shapes of the dim, bright and extra bright molecules using a zoom in on the island, as shown in Figure 4b. The white solid triangles indicate that the dim molecules still have a triangular shape, pointing towards the lattice vectors indicated by the black arrows. Therefore we conclude that these dim molecules are in the C-MSPA configuration. The dotted white lines indicate that, as before, the bright and dim molecules are located on the same lattice positions; also the centrally located dim molecules are not part of an additional layer. Since both the apparent height and the orientation of the dim molecules in this central part are consistent with those at the edge of the island, we conclude that these dim molecules are also in the C-MSPA configuration.

The shapes of the bright molecules are also clearly resolved in Figure 4b. They appear as triangles, as highlighted by the black dotted lines. The apparent triangles are observed in two orientations, which differ by a 180° rotation. However the shape is not exactly triangular. In nearly all cases one lobe is slightly brighter (dimmer) than the other two. In Reference 7 these shapes are called the a1 (a2) orientation. Similar to the triangular case, these orientations have a hexagon at the top and at the bottom, however they are slightly tilted. The a1 orientation is tilted

so that the 5-6 bond, i.e. a bond between a hexagon and a pentagon of the C_{60} cage is on top (and at the bottom). The a2 orientation is slightly tilted so that a 6-6 bond is on top. Possibly, the presence of a platinum atom directly below the molecule prevents the bottom hexagon to lie flat on the Pt(111) surface. Therefore the bright molecules are forced to adapt a configuration which is slightly tilted, namely the a1 and a2 configuration. Images recorded after the heat treatment at 280 °C (not shown here) indicate that after this step the bright molecules are already in the a1 and a2 configurations.

Nearly all extra bright molecules are oriented in a triangular shape pointing in the direction of lattice vectors. Apparently these molecules are not hindered from having their bottom hexagon lie flat in the Pt(111) plane. We will discuss these extra bright molecules in more detail using the results of the next heat treatment.

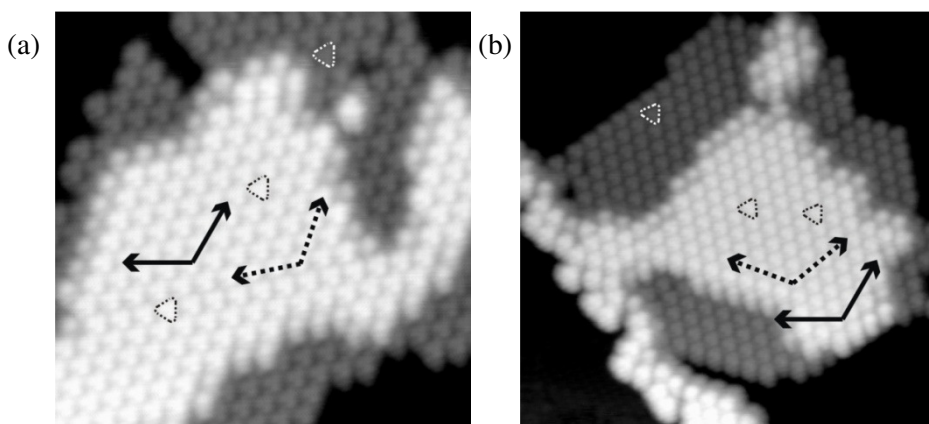


Figure 5. Two C_{60} islands after a 480 °C heat treatment imaged in STM topography (a) (25 nm x 25 nm, 1.7 V, 112 pA) and (b) (20 nm x 20 nm, 2.5 V, 116 pA). Black and white dotted triangles highlight the triangular shape of the extra bright and dim molecules respectively. The black dotted arrows indicate the C_{60} lattice vectors and the continuous black arrows show the Pt(111) lattice vectors based on the analysis of these images.

Figure 5 shows topographic images obtained after subsequent heating to 480° C. The molecules previously identified as bright molecules have completely disappeared. This leaves only the dim and extra bright molecules, which are in the same configuration and have the same apparent height as the dim and extra bright molecules in Figure 4. We will now extract the Pt(111) lattice vectors by using the C_{60} lattice vectors and molecular orientation. We will use the extra bright molecules, since they have the same orientation as the dim molecules, but have better visibility in the presented images. Based on the C-MSPA configuration as

presented in Reference 5, the triangles are aligned with the Pt(111) lattice vectors. Since the molecules form a $\sqrt{13}\times\sqrt{13}R13.9^\circ$ reconstruction, the C_{60} lattice vectors, shown as black dotted arrows, make an angle of 13.9° with respect to the Pt(111) lattice vectors. In Figure 5a the triangular shapes of the molecules point slightly to the left of their nearest neighbor. In other words, they are rotated slightly counter clockwise with respect to the C_{60} lattice vectors drawn as dotted arrows. This means that the Pt(111) lattice vectors are also rotated counter clockwise by 13.9° with respect to the black dotted C_{60} lattice vectors. This results in the Pt(111) lattice vectors shown as continuous black arrows. We apply the same procedure to the island shown in Figure 5b. The C_{60} lattice vectors do not point in the same direction as in Figure 5a. Furthermore, the triangular shapes are rotated slightly clockwise with respect to the white dotted C_{60} lattice vectors. However, to obtain the Pt(111) lattice vectors in this situation, the white dotted C_{60} lattice vectors must be rotated clockwise by 13.9° . This results in the Pt(111) lattice vectors shown as the continuous black arrows, which are consistent with those obtained in Figure 5a. This substantiates that the Pt(111) lattice vectors have been correctly determined, and that the molecules are indeed in the C-MSPA configuration.

We speculate that the extra bright molecules in Figure 4 and Figure 5 are also in the missing platinum atom configuration, but are situated on an additional layer of Pt(111). We base this speculation on four observations. (i) The extra bright molecules show the same orientation as the dim molecules, which we have shown to be explained by the missing platinum atom model. (ii) The height difference between the dim and extra bright molecules is 0.20 nm, similar to the Pt(111) step height¹⁸ of 0.23 nm. (iii) The STM data presented in Figure 5 show that approximately 50% of the molecules appear as extra bright molecules. In Reference 5, C_{60} molecules on Pt(111) were studied after a heat treatment at 380° , using X-ray diffraction (XRD). Given the temperature of the heat treatment in Reference 5, it is likely that in this case also $\sim 50\%$ of the molecules were extra bright molecules. The XRD measurement is however well explained using only the missing platinum atom model. This is best explained when both the dim and the extra bright molecules have adopted the missing platinum atom configuration. (iv) The appearance of an extra layer of Pt(111) requires the mobility of platinum atoms on the surface. Such a mobility is consistent with the observed reconstruction of the Pt(111) surface close to C_{60} islands. Furthermore in the appendix we present data of a moving Pt(111) step at room temperature. Both these

observations substantiate that platinum atoms are indeed mobile during the heat treatments.

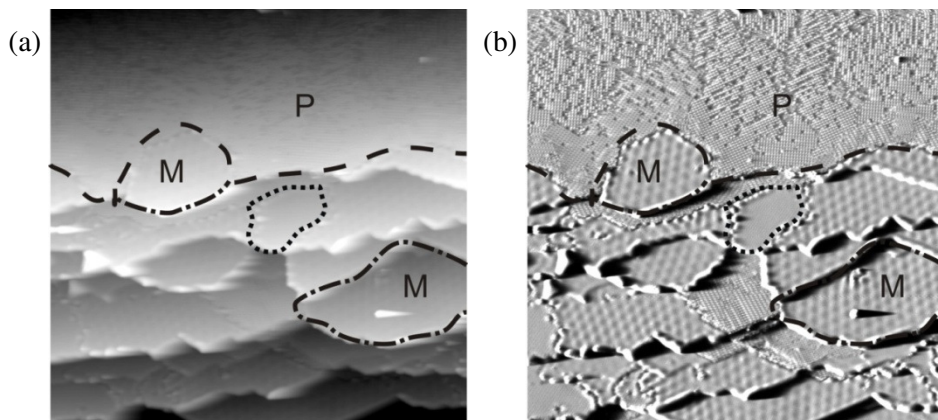


Figure 6. Topography (a) and current (b) STM images (80 nm x 80 nm, 48 mV, 40 pA) obtained after graphene formation at 940 °C. The black striped region indicated by the ‘P’ denotes a region of bare Pt(111) showing the surface reconstruction. The dash-dotted regions indicated by the ‘M’ denote graphene patches showing a Moiré pattern. The dotted line indicates the graphene patch with $\sqrt{3}\times\sqrt{3}R30^\circ$ reconstruction used for comparison with DFT results.

Figure 6 shows an STM image of graphene formed from the 0.5 ML C₆₀ on Pt(111) after a heat treatment at 940 °C. A large part of the image shows Pt(111) in the previously identified amorphous surface reconstruction, as highlighted by the black dashed line and the letter ‘P’ in the image. Graphene can be observed in domains with different rotation; among these are patches showing Moiré patterns, such as the domains highlighted by the black dash-dotted lines and the letter ‘M’. The area encircled by the dotted line shows a $\sqrt{3}\times\sqrt{3}R30^\circ$ reconstruction, as will be discussed below on basis of DFT calculations. The very large unit cells of the Moiré domains prohibit comparison with *ab initio* DFT calculations for these regions.

Studies based on DFT are typically carried out by choosing an initial configuration for the atoms in the unit cell. Using the forces on the atoms which have been calculated based on the electronic structure, new configurations can be found with increasingly lower total energies. In order to find the structure with the lowest total energy this procedure is then applied to different initial configurations, such as with or without a missing platinum atom. In Reference 9 such a DFT calculation is presented for the present system. Although it yields a lower total energy for the system with a platinum vacancy, this in itself does not prove that the structure

observed after the heat treatment at 940 °C is indeed caused by this configuration. The energy barrier for the formation of the missing platinum atom structure, estimated to be 3 eV,⁹ could prevent the system from reaching this configuration. We therefore compare the measured STM topography with a simulated topography. This simulated topography is based on Greens function calculations for the interaction between a tungsten tip and the calculated G-MSPA structure.⁹

The left part of Figure 7 shows a more detailed measurement of the STM topography determined on the $\sqrt{3}\times\sqrt{3}R30^\circ$ reconstructed graphene patch; the simulated STM topography is shown on the right. Overlaid on the simulated topography is a schematic representation of the missing platinum atom configuration. The bright features, highlighted by the white dotted line in both the measured and simulated topography, can now directly be related to platinum atoms located under a hexagon of the graphene lattice. The dark spots highlighted by the white dashed circles represent graphene carbon atoms located directly over a platinum vacancy. Based on this strong match, we conclude that the $\sqrt{3}\times\sqrt{3}R30^\circ$ graphene domains are in the G-MSPA configuration.

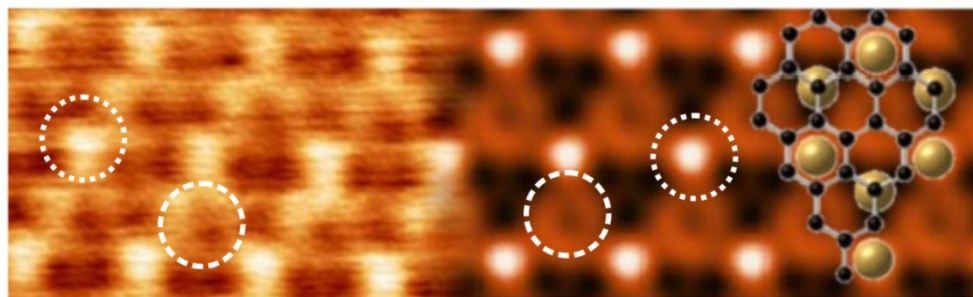


Figure 7. STM image (0.1 V, 50 pA) for the experimental (left) and DFT best-fit simulation (right).⁹ A schematic atomic model has been overlaid. Both images are merged in the central part. The gold colored atoms in the schematic model on the right indicate the Pt(111) atoms. The black atoms and the white lines between them indicate the carbon atoms and their bonds of the graphene lattice. The white dotted circle shown both on the simulated and the measured topography indicate the bright structure created by the platinum atoms which are not covered by a graphene atom. Similarly the white dashed circles indicate the carbon atom located on top of a platinum vacancy.

A summary of the presented results is given in Table 1. The observation of a MSPA configuration for both the C_{60} molecules and the $\sqrt{3}\times\sqrt{3}R30^\circ$ graphene domains, is well explained in the context of earlier studies of the Pt(111) surface. In Reference 16 an XRD study of the Pt(111) surface reveals that, at elevated temperature of 1200 °C, a reconstruction into a denser surface layer occurs. The

authors explain that at increased temperatures the interaction between the top layer and the underlying substrate is reduced, which allows the surface layer to collapse into a more dense form with lower free energy. More detailed modeling presented in Reference 17 shows that indeed the Pt(111) is only just stable and that the Pt(111) surface will reconstruct in the presence of a large number of adatoms. In this context the following picture emerges. In the MSPA configurations, carbon adatoms stabilize platinum surface vacancy underneath the adlayer, while it causes a reconstruction with a higher surface density surrounding the adlayers.

Table 1. The full pathway from deposition of C₆₀ at room temperature to the formation of graphene.

Step	Observation
After deposition / RT	$\sqrt{13}\times\sqrt{13}R13.9^\circ$ structure, molecular orientation dumbbell (6-6) aligned with the Pt(111) lattice and stripe (pentagon). Apparent height of all molecules 0.6 nm.
After 280° C treatment	Pt-reconstruction, dim C ₆₀ (apparent height 0.45 nm) as triangles with fixed orientation (C-MSPA configuration), bright C ₆₀ (apparent height 0.6 nm) in random molecular orientation $a1/a2$ (tilted hexagon). Dim C ₆₀ appear mostly at the edges of C ₆₀ islands in domains of a few molecules.
After 330° C treatment	Same as 280 °C, but extra bright C ₆₀ appear (apparent height 0.65 nm) in the C-MSPA configuration.
After 480° C treatment	The bright molecules have completely disappeared. Both extra bright and dim C ₆₀ are in the C-MSPA configuration, where the extra bright are on top of an additional Pt(111) layer.
After 940° C treatment	Rotationally disordered graphene, where domains with a $\sqrt{3}\times\sqrt{3}R30^\circ$ structure are in the G-MSPA configuration.

Conclusions

We have determined the intermediate steps in the pathway from deposition of C_{60} at room temperature to the formation of graphene. At room temperature the C_{60} molecules form islands with a $\sqrt{13}\times\sqrt{13}R13.9^\circ$ structure. The C_{60} molecules adopt orientations with either pentagons or 6-6 bonds on top. The 6-6 bond is aligned with the Pt(111) lattice. A heat treatment at 280 °C causes the molecules to change orientation to the slightly tilted hexagon orientation, i.e. the previously reported a1 and a2 configurations. Already after this heat treatment C_{60} molecules that are in the C-MSPA configuration are identified. The growth of domains of C_{60} molecules in the C-MSPA configuration at the edge of C_{60} islands, suggests that the energetic barrier for the formation of the C-MSPA configuration is lower at the edges of C_{60} islands and in the vicinity of other C_{60} molecules in the C-MSPA configuration. Additionally, the Pt(111) surface shows a reconstruction that we tentatively identify as an amorphous phase that was previously observed to form above 1200 °C.¹⁶ After annealing to 480 °C, all C_{60} molecules are in the C-MSPA configuration. Subsequent annealing to 940 °C causes the formation of graphene in rotationally disordered domains. For domains with a $\sqrt{3}\times\sqrt{3}R30^\circ$ structure, the atomic configuration could be calculated using DFT. A comparison between a simulated STM topography and a measured STM topography shows that these patches are in the G-MSPA configuration. The observation of a MSPA configuration for both the C_{60} molecules and the $\sqrt{3}\times\sqrt{3}R30^\circ$ graphene domains, is consistent with predictions that the Pt(111) surface is close to unstable.

Experimental

To obtain reproducible results, it is crucial to have a clean Pt(111) surface, for which the surface electronic structure is not affected by adsorbed molecules. For cleaning the Pt(111) sample after insertion into the system from air, the following procedure was applied: (i) The sample was annealed at 1000 °C in 1×10^{-6} mbar of O₂ for 5-10 min. (ii) The sample was sputtered using Ar ions at 1.5 keV and 2 μA for 5-10 min. (iii) The sample was annealed at 1000 °C for 5-10 min in UHV conditions ($\leq 1 \times 10^{-9}$ mbar). After applying two full cycles, i.e. steps (i) through (iii), three sputter-anneal cycles, i.e. step (ii) followed by step (iii), were performed.

After cleaning, C₆₀ is deposited on the substrate using a home built device, while the substrate is kept at room temperature. This home built device consisted of a folded tantalum foil, containing the C₆₀. The foil is heated using direct current, while its temperature is measured using a thermocouple. C₆₀ was evaporated by heating the home built device to 445 °C for 3 min which resulted in 0.5 monolayers of C₆₀. Directly after deposition the layer was studied using STM measurements that were performed in-situ using a low-temperature Omicron STM at 78K in UHV-conditions ($\leq 1 \times 10^{-11}$ mbar). Following the STM measurements, the sample was given an heat treatments at 280 °C, 330 °C, 480 °C, and 940 °C each for 7 min, each time followed by an STM study. During annealing and oxygen and heat treatments the temperature was controlled via a pyrometer (Impac IP-140, emissivity of 25%).

Appendix

Proof for the mobility of Pt(111) atoms on the Pt(111) surface

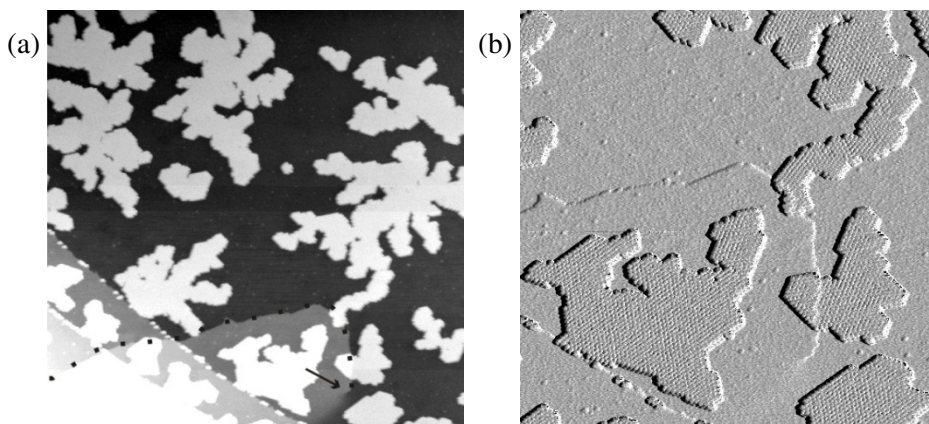


Figure A1. STM (a) topography and (b) current images taken directly after C_{60} deposition. Showing a deformed Pt(111) step indicated by the black dots, which is not covered by C_{60} molecules. The black arrow indicates a possible screw dislocation.

Figure A1 shows a Pt(111) step, highlighted by the black dots, which is not decorated with C_{60} molecules, as is typical⁹ for Pt(111) steps after deposition of C_{60} . Furthermore the step crosses several C_{60} islands, without having had any influence on their growth structure which is also atypical. We therefore conclude the step must have formed after deposition at room temperature, implying mobility of platinum atoms on the Pt(111) surface. A probable cause is the feature on the bottom right, as indicated by the arrow, which may be a screw dislocation of the crystal.

References

- ¹ M. Huang, *Phys. Chem. Chem. Phys.* **2012**, *14*, 4959.
- ² C. Cepek, A. Goldoni, S. Modesti, *Phys. Rev. B* **1996**, *53*, 7466.
- ³ N. Swami, H. He, B. E. Koel, *Phys. Rev. B* **1999**, *59*, 8283.
- ⁴ L. Giovanelli, C. Cepek, L. Floreano, E. Magnano, M. Sancrotti, R. Gotter, A. Morgante, A. Verdini, A. Pesci, L. Ferrari, M. Pedio, *Appl. Surf. Sci.* **2003**, *212–213*, 57.
- ⁵ R. Felici, M. Pedio, F. Borgatti, S. Iannotta, M. Capozzi, G. Ciullo, A. Stierle, *Nat. Mater.* **2005**, *4*, 688.
- ⁶ M. Sogo, Y. Sakamoto, M. Aoki, S. Masuda, S. Yanagisawa, Y. Morikawa, *J. Phys. Chem. C* **2010**, *114*, 3504.
- ⁷ C. Liu, Z. Qin, J. Chen, Q. Guo, Y. Yu, G. Cao, *J. Chem. Phys.* **2011**, *134*, 044707.
- ⁸ X. Q. Shi, A. B. Pang, K. L. Man, R. Q. Zhang, C. Minot, M. S. Altman, M. A. Van Hove, *Phys. Rev. B* **2011**, *84*, 235406.
- ⁹ G. Otero, C. González, A. L. Pinardi, P. Merino, S. Gardonio, S. Lizzit, M. Blanco-Rey, K. Van de Ruit, C. F. J. Flipse, J. Méndez, P. L. de Andrés, J. A. Martín-Gago, *Phys. Rev. Lett.* **2010**, *105*, 216102.
- ¹⁰ X.-Q. Shi, M. A. Van Hove, R.-Q. Zhang, *Phys. Rev. B* **2012**, *85*, 075421.
- ¹¹ P. Sutter, J. T. Sadowski, E. Sutter, *Phys. Rev. B* **2009**, *80*, 245411.
- ¹² M. Gao, Y. Pan, L. Huang, H. Hu, L. Z. Zhang, H. M. Guo, S. X. Du, H.-J. Gao, *Appl. Phys. Lett.* **2011**, *98*, 033101.
- ¹³ L. Gao, W. Ren, H. Xu, L. Jin, Z. Wang, T. Ma, L.-P. Ma, Z. Zhang, Q. Fu, L.-M. Peng, X. Bao, H.-M. Cheng, *Nat. Commun.* **2012**, *3*, 699.
- ¹⁴ G. Otero, J. Méndez, J. A. Martín-Gago, *Vacuum* **2011**, *85*, 1059.
- ¹⁵ G. Schull, R. Berndt, *Phys. Rev. Lett.* **2007**, *99*, 226105.
- ¹⁶ A. R. Sandy, S. G. J. Mochrie, D. M. Zehner, G. Grübel, K. G. Huang, D. Gibbs, *Phys. Rev. Lett.* **1992**, *68*, 2192.
- ¹⁷ R. Pushpa, S. Narasimhan, *Phys. Rev. B* **2003**, *67*, 205418.
- ¹⁸ The DFT calculations in Reference 9, show that the Pt-Pt distance is 0.277 nm. The height of a step on the Pt(111) surface is therefore equal to the height of a tetrahedron with ribs of length 0.277 nm. This results in a step height of $(1/3) \times \sqrt{6} \times 0.277 \text{ nm} = 0.226 \text{ nm}$.

Chapter 4:

Quasi-one dimensional in-plane conductivity in filamentary films of PEDOT:PSS

Abstract

The mechanism and magnitude of the in-plane conductivity of poly(3,4-ethylenedioxythiophene):poly(styrenesulfonate) (PEDOT:PSS) thin films is determined using temperature dependent conductivity measurements for various PEDOT:PSS weight ratios. For all studied weight ratios the conductivity of PEDOT:PSS is well described by the relation $\sigma = \sigma_0 \exp[-(T_0/T)^{0.5}]$ with T_0 a characteristic temperature. The exponent 0.5 indicates quasi-one dimensional (quasi-1D) variable range hopping (VRH). The experimentally determined conductivity prefactor σ_0 varies over three orders of magnitudes and follows a power law $\sigma_0 \propto c_{\text{PEDOT}}^{3.5}$ with c_{PEDOT} the weight fraction of PEDOT in PEDOT:PSS in the range of 0.04–0.3. Analysis of the field dependent conductivity shows a behavior that is consistent with quasi-1D VRH. Combined, these observations suggest that conductance takes place via a percolating network of quasi-1D filaments. Using transmission electron microscopy (TEM) filamentary structures are indeed observed both in vitrified dispersions and in dried films. For PEDOT:PSS films that were processed with a high boiling solvent, the Ohmic temperature dependence behaves as a quasi-1D VRH system, but the low characteristic temperature T_0 indicates that the system is close to the critical regime between a metal and an insulator. In this case, the conductivity prefactor scales linearly with c_{PEDOT} , indicating the conduction is no longer limited by a percolation of filaments. The lack of observable changes in TEM upon processing with the high boiling solvent suggests that the changes in conductivity are due to a smaller spread in the conductivities of individual filaments, or a higher probability for neighboring filaments to be connected rather than being caused by morphological modification of the filaments.

Introduction

Practical interest in poly(3,4-ethylenedioxythiophene):poly(styrenesulfonate) (PEDOT:PSS) is mainly driven by its widespread application as solution processable electrode layer in organic light emitting diodes and in organic and hybrid photovoltaic cells. In particular, these applications require a transparent conducting electrode which is generally provided by a layer of tin-doped indium oxide (ITO). Significant recent progress with respect to the combination of conductivity and transparency of PEDOT:PSS gives strong indications that it might be possible to replace the expensive and brittle ITO layer with a PEDOT:PSS layer.^{1,2}

Additionally, PEDOT:PSS and other PEDOT-based systems exhibit several technological relevant characteristics, such as charge transport properties in the critical regime close to the metal-insulator transition,^{3,4,5,6,7} order of magnitude in-/out-of-plane anisotropy in the electrical conductivity,^{8,9,10} power law behavior for the out-of-plane conductivity,^{11,12} high thermoelectric figure of merit,¹³ reversible volume changes,¹⁴ and the existence of polarons or bipolarons depending on interchain interaction.^{5,15}

To obtain PEDOT:PSS, the conductive element, PEDOT, which is undoped and insoluble in its pristine state is synthesized from 3,4-ethylenedioxythiophene (EDOT) in an aqueous solution containing the polyelectrolyte PSS. The PEDOT oligomers are attached to PSS chains by ionic interactions, which stabilize the doping of the PEDOT and solubilize the otherwise insoluble PEDOT in water, probably via the formation of core-shell micelles with a PEDOT-rich core and a PSS-rich shell.^{16,17} Atomic force microscopy (AFM), scanning tunneling microscopy (STM), and transmission electron microscopy (TEM) studies indicate that these micelles are present in spin coated layers.^{8,18,19} The morphology of the resulting layers is further complicated by the presence of composition gradients²⁰ or the presence of a lamellar structure.^{8,21} Post-processing treatments of PEDOT:PSS thin films, aimed at improving the electro-optical properties of the film, are often thought to affect this morphology.^{2,15,19,22,23,24,25,26}

Charge transport measurements are an important tool for gaining insight into the complex properties of PEDOT:PSS. Typically the temperature dependence of the conductivity is large and interpreted in the context of variable range hopping

(VRH).^{7,8,9,15,19,25,27} For the temperature dependent conductivity, $\sigma(T)$ at low bias, i.e. the Ohmic conductivity, VRH predicts that

$$\sigma(T) = \sigma_0 \exp \left[- \left(\frac{T_0}{T} \right)^\alpha \right], \quad (1)$$

where σ_0 is the conductivity prefactor, T_0 the characteristic temperature, and α a characteristic exponent related to the dimensionality of the system, d , by $\alpha = (1+d)^{-1}$. VRH behavior has been measured in PEDOT:PSS with $\alpha = 1/2$ in spin-cast^{2,15,19,22,25} and drop-cast^{6,26,28} films and in nano-wires^{4,27}, with $\alpha \approx 1/3$ in drop-cast films⁷ and with $\alpha = 1/4$ in spin-cast films.^{8,9} With few exceptions^{4,28} it was concluded that VRH correctly describes the mechanism of conduction. There is a remarkable high number of observations of quasi-one dimensional (quasi-1D) VRH in PEDOT:PSS. In some cases this could be directly related to morphology.^{19,27} Other articles^{2,6,15,22} cite the explanation of Epstein,²⁹ which describes a VRH system where states are weakly localized along the polymer backbone and strongly localized perpendicular to the backbone. Although such mechanism was shown to take place in cross-linked polyaniline,²⁹ it seems at odds with the granular morphology that is often observed in PEDOT:PSS films. Moreover, the prediction²⁹ that the electric field dependence of the conductivity relative to the Ohmic conductivity should not depend on temperature is inconsistent with the model suggested by Nardes *et al.*¹⁹

Here we explore the transport properties of PEDOT:PSS by characterizing the dependence of the conductivity on the composition (PEDOT to PSS ratio) and the temperature. The physical picture obtained from combining the two is more complex than expected. We find that the transport properties are best explained by VRH conduction through a percolating network of 1D filaments that is close to the percolation threshold. The combination of the two mechanisms offers a consistent explanation for the quasi-1D VRH behavior observed in many PEDOT:PSS systems. This mechanism is also consistent with the morphological features observed by TEM at cryogenic temperatures: we find that elongated filaments are already present in the dispersion, and maintain their presence in the dried layer, while their diameter shrinks. We extend our investigation to the more practically relevant PEDOT:PSS processed with a high boiling solvent (HBS) additive, which exhibits orders of magnitude higher conductivity. The linear relation between

conductivity and PEDOT:PSS ratio indicates a network with higher connectivity far away from the percolation threshold.

Results and discussion

In-plane conductivities were measured on thin spin cast films on glass substrates under high vacuum conditions. Figure 1 shows the measured conductivity as a function of temperature and bias for native processed, i.e. processed without additives, PEDOT:PSS in the weight ratios of 1:2.5, 1:6, 1:12, and 1:20. Notice that for lower PEDOT:PSS ratios the range in conductivity shifts down and extends. This way, two features are clearly observed. First, the room temperature conductivity decreases significantly as the weight fraction of PSS increases while the temperature dependence of the Ohmic conductivity (at $F = 0$, i.e. zero electric field) increases. In particular, while a 2 orders of magnitude increase in the conductivity is observed for samples comprising 1:2.5 PEDOT to PSS (Figure 1a) when the temperature is raised from 10 to 275 K, a 4 orders of magnitude increase in the conductivity is observed for the 1:20 samples (Figure 1d). Second, as the electric field is increased, especially the low temperature conductivity becomes higher and the temperature dependence of the in-plane conductivity becomes less.

For all samples, finite electric fields have a similar effect as increased temperatures; hence the temperature dependence at large electric fields becomes reduced. This behavior is typical for doped disordered semiconductors, such as PEDOT:PSS. In these materials, charge carriers move between localized states, or sites, by a thermally activated tunneling (i.e. hopping) process. As both thermal energy ($k_B T$) and an electric field in the hopping direction may provide the required energy for overcoming the energy barrier between sites a higher conductivity is reached when increasing the electric field or raising the temperature.

Composition dependence of the Ohmic conductivity in PEDOT:PSS

The insets of Figure 2 show the Ohmic conductivity (i.e. at $F = 0$) and the reduced activation energy $W = d(\log\sigma) / d(\log T)$ PEDOT:PSS presented in Figure 1. Fits to Mott's VRH theory (Equation (1)) are shown for $\alpha = 1/2$ (1D), $1/3$ (2D), and $1/4$ (3D) in red, green, and blue respectively. All PEDOT:PSS samples are best described by the fit with characteristic exponent $\alpha = 1/2$, indicating that transport in our samples is quasi-1D. The fitted parameters corresponding to $\alpha = 1/2$ are shown in Table 1. A truly one dimensional system cannot conduct current, because disordered 1D wires of infinite length will always contain a blocking site.³⁰

However, a large set of parallel one-dimensional conduction paths, or ‘filaments’ was shown to give rise to $\alpha = 1/2$.^{31,32,33} For a particular PEDOT:PSS system processed with a high-boiling solvent morphological evidence was previously found to support such an interpretation.¹⁹ A requirement³⁴ for the application of VRH theory is that $(T_0/T) \gg 1$. For the native processed PEDOT:PSS and temperature range studied in this paper $(T_0/T) = 4\text{--}16$, which is in agreement with observations of other quasi-1D VRH systems.^{4,27,35,36,37} A more detailed investigation of α yields that the data is best described by $\alpha = 0.45 \pm 0.05$, where α decreases slightly with temperature.

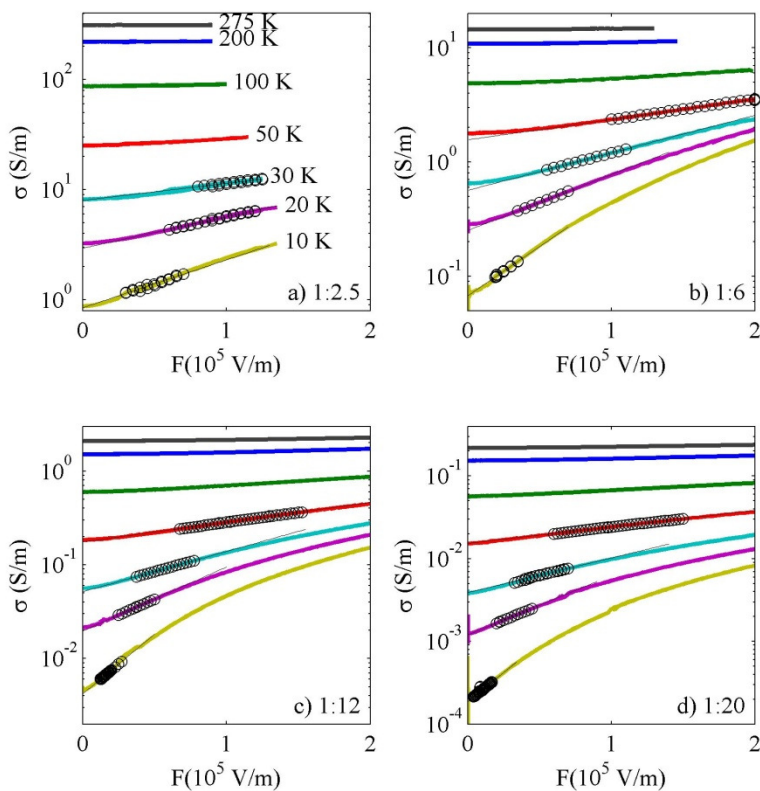


Figure 1. Solid lines are measurements of the conductivity as a function of electric field at the indicated temperature for native PEDOT:PSS in the ratios: (a) 1:2.5, (b) 1:6, (c) 1:12, and (d) 1:20. The thin black lines indicate fits to the measurement points highlighted by the circular markers. Intermediate temperatures are not shown for clarity.

Alternative models found in literature which yield Equation (1) with $\alpha = 1/2$ will be discussed after the full model is presented.

Table 1. Quasi-1D VRH fitting parameters for the different samples produced from the various PEDOT:PSS formulations, shown in Figures 2 and 7.

Samples	T_0 (K)	σ_0 (S/m)	$\sigma(300\text{ K})$ (S/m)
PEDOT:PSS, ratio 1:2.5	1.0×10^3	1.8×10^3	2.9×10^2
PEDOT:PSS, ratio 1:6	7.0×10^2	78	17
PEDOT:PSS, ratio 1:12	9.3×10^2	16	2.7
PEDOT:PSS, ratio 1:20	1.1×10^3	2.7	0.39
PEDOT:PSS, ratio 1:2.5 w/ HBS	39	6.3×10^4	4.4×10^4
PEDOT:PSS, ratio 1:6 w/ HBS	41	3.1×10^4	2.2×10^4
PEDOT:PSS, ratio 1:12 w/ HBS	57	1.5×10^4	9.4×10^3
PEDOT:PSS, ratio 1:20 w/ HBS	66	8.7×10^3	5.5×10^3

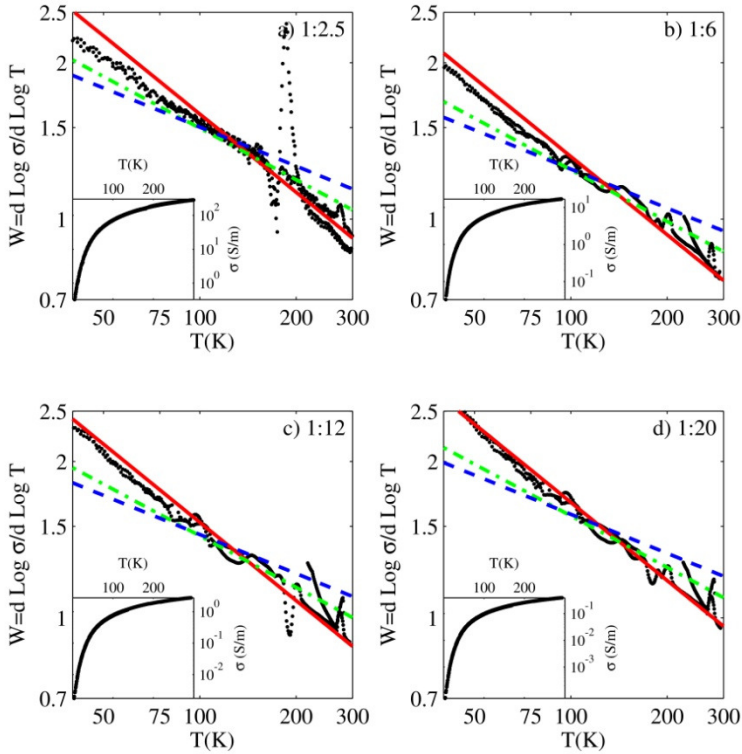


Figure 2. Measured Ohmic conductivities as a function of temperature (insets) and the reduced activation energy W as a function of temperature for native PEDOT:PSS in the ratios (a) 1:2.5 (b) 1:6 (c) 1:12 and (d) 1:20. The red, green and blue lines indicate slopes of $1/2$, $1/3$ and $1/4$, resp.

Figure 3 shows the characteristic temperatures T_0 and conductivity prefactors σ_0 obtained for five spin coated samples of each of the four PEDOT:PSS ratios, taken from two batches of newly prepared dispersions. To study the trend in σ_0 and T_0 with PEDOT concentration, connections between measurements points have been added to both Figure 3a and 3b. These connections indicate measurements that have been performed simultaneously. The data clearly show a decreasing characteristic temperature with increasing PEDOT concentration, which can be described using the empirical relation $T_0 \propto (c_{\text{PEDOT}})^{-0.35}$ indicated by the black line where c_{PEDOT} is the weight fraction of PEDOT in PEDOT:PSS..

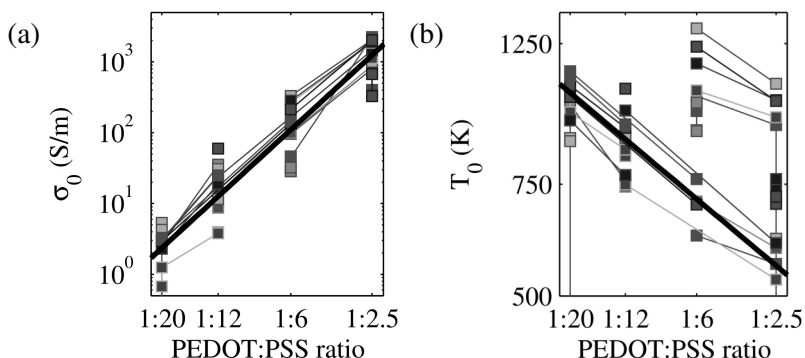


Figure 3. (a) Characteristic temperatures and (b) conductivity prefactors obtained from fits to the measured Ohmic conductivity as a function of temperature for five spin coated samples of each of the four PEDOT:PSS ratios, prepared from two batches of newly prepared dispersions. Simultaneously measured data are connected by thin lines. Both figures are double-logarithmic plots, with the x-axis scaled as PEDOT concentration, c_{PEDOT} . The solid black lines indicate a slope of (a) -0.35 and (b) 3.5.

The measurements of the conductivity prefactor shown in Figure 3b show that reducing the concentration of the conductive polymer PEDOT by adding additional PSS strongly reduces the conductivity. The relation between conductivity and PEDOT concentration can be described by a power law: $\sigma_0 \propto (c_{\text{PEDOT}})^{3.5}$ (indicated by the black line in Figure 3b). A similar power law dependence has been obtained when high aspect ratio conductive filaments were added to an insulating matrix.³⁸ This behavior can be explained on basis of percolation theory: as conductive elements (PEDOT) are added to the insulating filler (PSS), conduction can occur when a path is formed by connected conductive elements, running from one electrode to the other. The lowest concentration at which this occurs is defined as the percolation threshold. Above this concentration the number of conduction paths

strongly increases with increasing concentration of conductive material, typically causing the conduction to increase as a power law.³⁹ No threshold can be distinguished in Figure 3b. The conductive elements might at most contain PEDOT:PSS in a 1:2.5 ratio, otherwise the power law behavior would not persist up to 1:2.5. This means that the percolation threshold must be much lower than 12.5 vol-%, otherwise PEDOT:PSS in the ratio 1:20 would not show any conduction. If the conductive elements would be randomly dispersed spheres the percolation threshold would be⁴⁰ 29 vol-% (assuming a 3D system) while both disks,⁴¹ and filaments⁴² with a high aspect ratio (height to radius) are expected to exhibit (much) lower percolation thresholds. The percolation threshold significantly below 12.5 vol-% is consistent with non-spherical shape of the conductive elements in PEDOT:PSS mixtures.

TEM investigation

To investigate the morphology of PEDOT:PSS blends and possibly correlating this to the transport measurements a microscopic investigation of the PEDOT:PSS dispersion and thin films was performed. TEM images of vitrified dispersions (cryo-TEM) and dried layers (HRTEM) of PEDOT:PSS samples are dominated by the presence of randomly oriented worm-like filaments, see Figures 4a-d. The cryo-TEM images indicate that the filaments-like structures are already present in the dispersion and remain present in the dried layer, at a much higher concentration and reduced diameter. PEDOT-rich grains with a PSS-rich shell were observed before in dried layers,^{8,9,17,19,20,43,44} and via dynamic light scattering in dispersion.⁴⁴ We propose that the filaments observed in Figures 4a-d are similar structures, i.e. the filaments consist of a PEDOT-rich core and a PSS-rich shell. The filamentary structure of the films and the high aspect ratio of the observed filaments fully explains the percolation behavior reflected in the power law dependence of the conductivity prefactor on PEDOT concentration (Figure 3b).

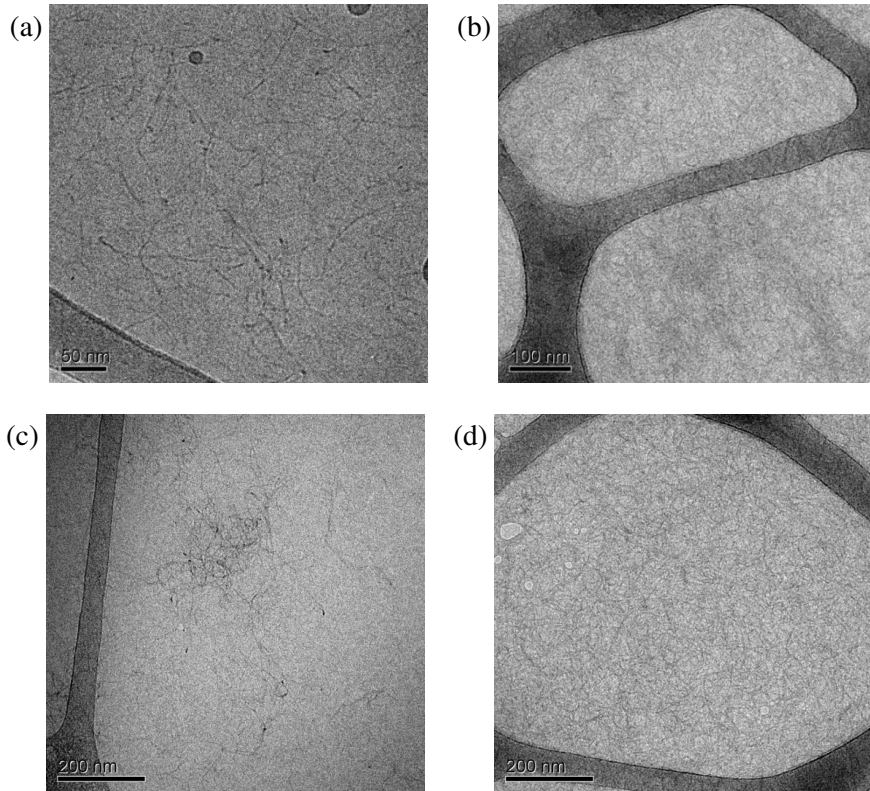


Figure 4. (a) Cryo TEM image of PEDOT:PSS emulsion in the ratio 1:2.5. The darker areas are the TEM grid-lines. (b) HRTEM image of dry specimen prepared from the same sample. The typical diameter of the filaments is 4-5 nanometers and their length may reach tens to hundreds of nanometers. (c) Cryo-TEM images of PEDOT:PSS emulsion with 1:20 ratio and (d) HRTEM of the same sample.

Consistent description for the composition dependence of the conductivity in the native processed material

Based on the results presented in Figures 1-4, we propose the following hierarchical model for the conduction behavior of the present PEDOT:PSS system. First, we suggest that current in PEDOT:PSS is transported in quasi-1D PEDOT-rich filaments which are embedded in a PSS-rich matrix, as indicated by the thick green and thin blue lines in Figure 5a. Along these filaments charges hop from site to site; such sites are shown in the zoom-in accented by the red square. Although PEDOT-rich grains are commonly observed in PEDOT:PSS, investigations of our

PEDOT:PSS layers using AFM and STM could not reveal evidence for such grains.^{8,18,19} Therefore we do not claim that hopping takes place between grains; e.g., the hopping sites might also be single or aggregated PEDOT oligomers along an extended PSS chain. The sites among which the hopping takes place are however restricted to filaments. Second, filaments that participate in conduction need to be part of a percolating network which connects to both electrodes. In Figure 5a these filaments are drawn as thick green lines. We suggest that the conductivity of this network is determined by the conductivity of the filaments as opposed to the nodes between the filaments. This way the temperature and field dependence of the conductivity is that of the intra-filament conductivity. The resulting network can be approximated as a large set of parallel filaments. Such sets are known to show VRH-type behavior with a characteristic exponent of $\alpha = 1/2$.^{31,32,33,45} Reduction of the PEDOT:PSS ratio by addition of the insulating PSS decreases the density of the PEDOT-rich filaments. This way, the conducting network is diluted and consequentially the probability for a filament to participate in the conducting network decreases. According to percolation theory, this gives rise to the observed power law dependence of the conductivity on the concentration of conductive material, provided the network is sufficiently close to the percolation threshold.³⁹

The trend in T_0 with PEDOT concentration and the observation that the measured values of α are somewhat below $\alpha = 1/2$, can be explained by corrections by Raikh and Ruzin⁴⁵ to Mott's quasi-1D VRH. Such corrections appear since in one dimension, regions without states, known as breaks, become important. This is because the current can no longer flow around these breaks as it could in two or more dimensions. Both analytical calculations and numerical simulations show that such breaks result in behavior which can still be described by Equation (1) with characteristic exponent $\alpha = 1/2$, however a correction for T_0 should be used, namely $T^* \approx 2T_0 \ln[2(L_{fil} / \xi)(T / T_0)]$, where L_{fil} is the length of the filaments and ξ the localization length. For finite temperature intervals this correction is very similar to the original Equation (1) with $\alpha \lesssim 1/2$. At higher PEDOT concentrations the filaments in the network are expected to be shorter, leading to smaller values of T^* , which explains the decreasing trend of T_0 with increasing PEDOT concentration observed in Figure 3a. Unfortunately extracting typical values of L_{fil} proves difficult for two reasons. Firstly, $\sigma(T)$ is only weakly dependent on L_{fil} which results in inaccurate measurements of L_{fil} . Secondly, at low temperatures and high

PEDOT concentration, the hopping length is expected to be of the order of the length of the filaments (for details see the discussion on the field dependence) and the 3D character of the network of filaments starts playing a role. The corrections by Raikh and Ruzin are calculated for large sets of parallel filaments which lack such a 3D character.

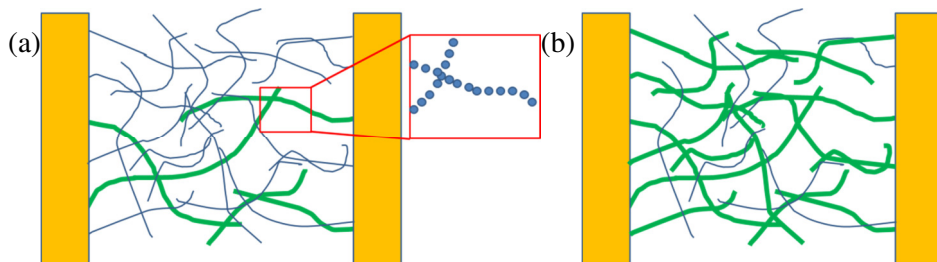


Figure 5: Schematic representation of filaments which determine the charge conduction in (a) native processed PEDOT:PSS and (b) PEDOT:PSS processed with HBS. The blue lines indicate the conducting filaments, of which the thick green lines show the filaments participating in conduction. The yellow bars represent the electrodes. The red square indicates a zoom-in showing possible sites for charge carrier hopping along the chain. Compared to native processed PEDOT:PSS (a), the nodes between filaments in PEDOT:PSS processed with HBS (b) have a much higher probability of being connected.

Alternative interpretations for the observed quasi-1D VRH behavior

We will now discuss alternative explanations for the presented data. A common alternative explanation for VRH with a characteristic exponent $\alpha = 1/2$ is the Efros-Shklovskii VRH model.³⁴ This model is derived identically to the Mott VRH model while taking into account a soft Coulomb gap in the density of states around the Fermi level, i.e. a depletion in the density of states near the Fermi level which exists because of the Coulomb interaction between the charge carriers. Inside this Coulomb gap the density of states does not depend on any material parameter except for the dielectric constant. The characteristic temperature in the Efros-Shklovskii VRH model can be shown to only depend on the dielectric constant, the dimensionality and the localization length. To explain a characteristic temperature of 1000 K in PEDOT:PSS with a dielectric constant of $\kappa \approx 4$ would require an unrealistically large localization length of $\zeta = 0.3 \mu\text{m}$.

Another alternative is a model by Sheng which describes hopping between metallic grains in an insulator matrix.⁴⁶ This model assumes that the thickness of the insulating shell around the metallic particles is proportional to the size of the metallic particles, which is justified for co-evaporated systems. Using this relation,

the model is able to take into account both the tunneling distance for the hops, and the energy barrier, which is determined by the charging energies of the grains. This results in the behavior described by Equation (1) with $\alpha = 1/2$. Furthermore, the example by Sheng shows that with increasing concentration of the metal, T_0 increases moderately while the conductivity increases an order of magnitude, similar to our measurements. Studies of the morphology of PEDOT:PSS have reported the presence of PEDOT-rich particles, although these were explicitly not observed for the present materials. However, as pointed out by Nardes, no evidence nor mechanism for the crucial constant size/thickness ratio has been found. Furthermore, $\sigma(F,T)$ does not resemble the high field prediction from Sheng's model, although this may be attributed to the comparatively low fields used in this experiment. Unfortunately Sheng does not make predictions for the non-Ohmic conductivity at lower fields.

A third alternative is offered by the model of Zuppiroli,⁴⁷ which describes polymers which are coupled to each other by dopants. This model is consistent with Equation (1) with $\alpha = 1/2$ and also predicts a decreasing trend of T_0 with increasing c_{PEDOT} . It does not make any predictions about non-Ohmic behavior or σ_0 . However, the polymer used to check their model shows no appreciable change in σ_0 while the doping is varied between 2.5 % and 55 %. Furthermore, similar to Sheng's model this model assumes the thickness of the insulating shell of the metallic particles to be proportional to the size of the metallic grain, while no mechanism is known for PEDOT:PSS which would cause such a proportionality.

Characterization of the field dependence of the conductivity of native processed PEDOT:PSS of varying ratio

To obtain further information about the characteristics of the conducting network, the field dependence in Figure 1 has been analyzed. Pollak and Riess⁴⁸ predict for non-Ohmic transport in variable range hopping systems:

$$\sigma(F,T) \propto \exp \left[c \frac{eFL(T)}{k_B T} \right], \quad (2)$$

where F denotes the electric field, e the electron charge, $L(T)$ the effective length of a hop, c is a constant related to the angle between the hopping direction and the

field estimated to be $c = 0.17$, and k_B denotes the Boltzmann constant. This expression is valid in the intermediate field range, i.e. where $(T_0/T)^a k_B T > eFL(T) > k_B T$. Therefore fits in Figure 1 are restricted to $1.3 < \sigma(F,T)/\sigma_{\text{OHM}}(T) < 2$, i.e. the points indicated by the circular markers. The low temperature non-Ohmic curves in Figure 1 show that the intermediate field regime relates to a bending point in $\log \sigma$ vs. F , so that even though Equation (2) does not describe the whole curve, $L(T)$ is uniquely defined. Equation (2) has been derived for 2D and 3D variable range hopping and takes into account the effect of a change in the percolating path due to the field. Since we expect the network of quasi-1D filaments to extend in three dimensions, possibly with one of the dimensions restricted due to the limited film thickness, we expect Equation (2) to hold, possibly with a different value of c . Also numerical simulations of quasi-1D VRH systems support the use of Equation (2) for these systems.³³

The effective hopping lengths determined for native processed PEDOT:PSS in ratios 1:2.5, 1:6, 1:12 and 1:20 using Equation (2) are shown in Figure 6. In Figure 6 the filled red symbols indicate results obtained using Equation (2) directly to available data in the intermediate field regime. Since at high temperatures experimental conditions did not allow to reach these fields, an empirical extrapolation has been used, as discussed in the Appendix. The open blue symbols show the effective hopping lengths obtained by this procedure.

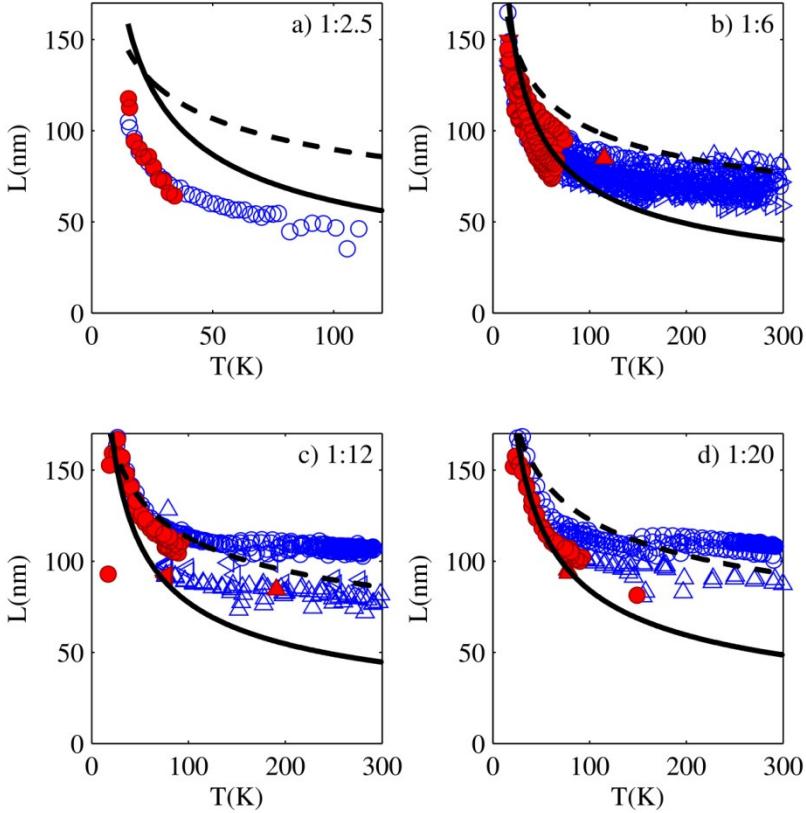


Figure 6. Extracted effective hopping lengths from I - V measurements on PEDOT:PSS with ratio (a) 1:2.5, (b) 1:6, (c) 1:12 and (d) 1:20. The solid red symbols represent fits of Equation (2) to data in the intermediate field range. The open blue symbols represent extrapolated values based on the Ohmic and low field ranges. To correct for temperature inaccuracies at low temperatures, the temperature was determined by the Ohmic conductivity using Equation (1) and $\alpha = 1/2$. The thick black continuous and dotted line represent expected results based on Equation (3) for localization lengths $\xi = 10$ nm in quasi-1D and $\xi = 60$ nm in 3D, respectively.

The magnitude of the typical length scale L is, for all temperatures, compatible with the length of the filamentary structures observed in TEM and decreases with increasing temperature. In variable range hopping this occurs because at lower temperatures, the lower thermal energy restricts the hopping to sites with energies closer to the Fermi level. This restriction forces the charge carriers to make longer hops, as described by:³⁴

$$L(T) = c_L \xi \left(\frac{T_0}{T} \right)^\alpha \quad (3)$$

where c_L is a constant depending on the dimensionality of the problem, for quasi-1D³³ $c_L = 2.6$ and for 3D $c_L = 0.35$,⁹ and ξ is the localization length. The hopping rate between two states decays exponentially with the distance, with a decay length $\xi/2$. The black continuous and dotted line in Figure 6 show the predicted effective hopping lengths are consistent with an effective localization length $\xi = 10$ nm in quasi-1D and $\xi = 60$ nm in 3D, respectively. With the exception of PEDOT:PSS in the ratio 1:2.5, the data points correspond reasonably well to both the 1D and 3D predictions. The deviation of PEDOT:PSS with ratio 1:2.5 is most probably caused by heating of the layer during high voltage pulses. A quantitative analysis of such heating is presented in the Appendix.

Interpretation of the effective localization length

In lowest order the localization length can be interpreted as the decay length of the wavefunction in quantum mechanical tunneling using the following equation:⁴⁹

$$\frac{\xi}{a_0} = \left(\frac{13.6eV}{\Delta E} \right)^{1/2} \left(\frac{m_0}{m_{EFF}} \right)^{1/2}, \quad (4)$$

where $a_0 = 0.5$ nm is the Bohr radius, ΔE is the energy difference between the chemical potential and the onset of the (nearly) free electron band, m_0 is the free electron mass, m_{EFF} is the effective mass of the (nearly) free electron band. If the tunneling inside PEDOT:PSS is similar to vacuum tunneling, then using $m_{EFF} = m_0$ and estimating¹⁷ $\Delta E \approx 5$ eV results in $\xi_{EST} \approx 0.9$ nm. From measurements for PEDOT:PSS films similar to those presented here Nardes *et al.* have determined $\xi = 8.2$ nm.⁹ A study into the electrical properties of single PEDOT:PSS nanowires found $\xi = 0.07$ nm.^{4,50} Measurements probing the magnetoresistance of PEDOT:PSS thin films led to $\xi = 10$ nm.²⁶ The discrepancy between the vacuum estimate and the values determined using Equation (3) can be explained in two ways.

Firstly, there could be a band which is closer to the chemical potential than the vacuum band. This could be a band formed by the π -conjugated states of the PEDOT molecules. Using ab-initio theory the effective mass of a prototypical

conjugated molecule was predicted to be $m_{\text{EFF}} = 0.15 m_0$.⁵¹ This requires for the 1D (3D) case $\Delta E \approx 0.25 \text{ eV} (7\text{meV})$. ΔE reflects the offset between the chemical potential, that lays in the localized states, and the delocalized or band-like states. Hence, the fact that in the 1D case $\Delta E \approx 10 k_B T$ is consistent with VRH-dominated transport. Simultaneously, the (energetic) proximity of band-like states can significantly increase the localization length. For the 3D case, the existence of band-like states within $k_B T$ of the chemical potential would result in a conduction behavior that is not dominated by hopping.

Secondly, a renormalization of the field may be necessary.⁹ If conduction takes place between metallic PEDOT-rich regions of size $d \approx 25 \text{ nm}$ located inside the PSS-shelled micelles, and the PEDOT-rich regions are separated by $s \approx 3 \text{ nm}$, then on average the potential between the metallic regions does not drop evenly across a length of $d+s$, but instead drops entirely in the insulating region of length s . Renormalizing all length scales by $s/(s+d) \approx 10$, resolves the discrepancy between the measured and estimated localization length. A similar renormalization is suggested in Reference 52, where it is suggested that variable range hopping systems have a length scale, L_0 , beyond which the material is homogenous. The change in chemical potential across a region of this length scale is concentrated on the most difficult hop in this part of the conduction network.

Both explanations work equally well for the data presented here. However, the first explanation also explains the magnetoresistance measurements in Reference. 26, which yielded similar results to those presented here. Unfortunately, the data presented here is not sufficient to distinguish between both scenarios. It is concluded that the temperature dependence of the non-Ohmic conductivity measurements is reasonably well described in the framework of quasi one dimensional VRH and the anomalously high localization length can be explained in several ways.

Composition dependence of the conductivity of PEDOT:PSS processed with high-boiling solvent

The conductivity of PEDOT:PSS when it is processed with a high-boiling solvent (HBS) added to the PEDOT:PSS dispersion in water is much higher and has a much weaker temperature dependence than its native counterpart processed without HBS.^{6,7,15,19,22,24,26} The insets in Figure 7 show the conductivity as a function temperature for PEDOT:PSS processed with HBS with PEDOT:PSS

ratios 1:2.5, 1:6, 1:12 and 1:20. To study the behavior of the Ohmic conductivity as a function of temperature, we calculated the reduced activation energy W for these measurements, as is shown in the main Figures 7a-d. For each curve, fits to Equation (1) are added for values of $\alpha = 1/2$, $1/3$ and $1/4$ which are, successively, the red, green and blue curves. The fit parameters for the fits for $\alpha = 1/2$ are shown in Table 1 as these give the best representation of the data, again in agreement with many previous reports.^{15,19,22,26}

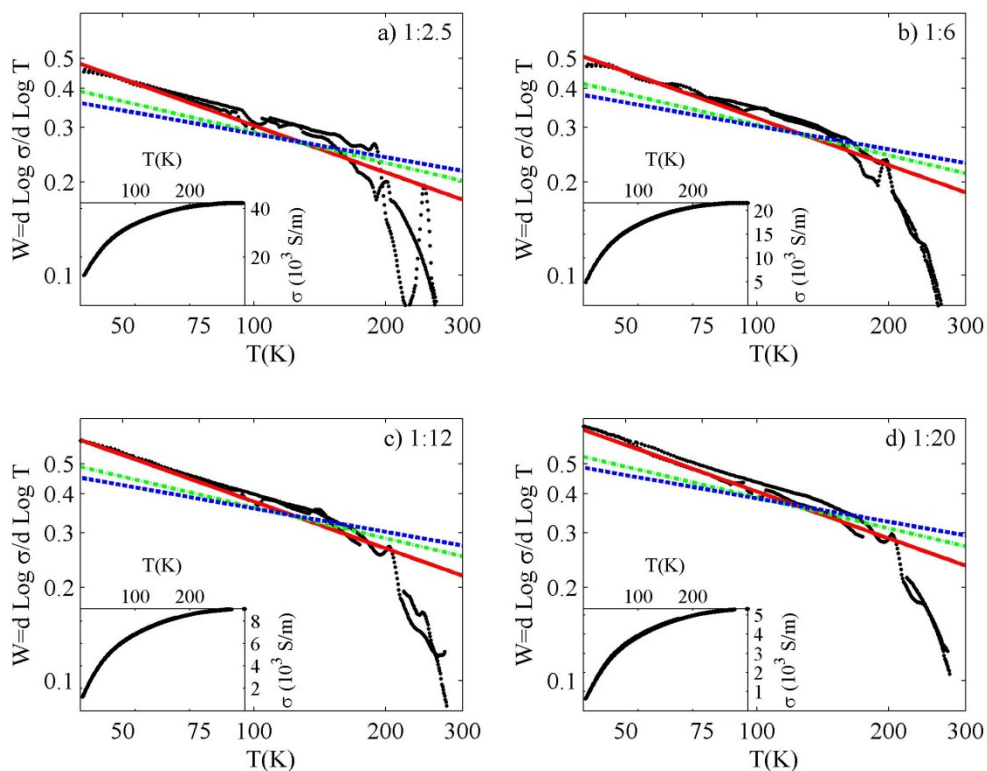


Figure 7. Measured Ohmic conductivities as a function of temperature (insets) and the reduced activation energy W as a function of temperature for PEDOT:PSS processed with HBS in the ratios (a) 1:2.5 (b) 1:6 (c) 1:12 and (d) 1:20. The red, green and blue lines indicate slopes of $1/2$, $1/3$ and $1/4$, resp.

Figure 8a shows the T_0 values obtained for the fits with $\alpha = 1/2$ for several measurements on two sets of spin coated samples. Extracted values of T_0 range from 30 to 100 K, which is lower than the lowest $T_0 \approx 275$ K found for PEDOT:PSS processed with a HBS in literature.²⁶ Other references^{15,19,22} show T_0

$> \approx 1000$ K. As in the PEDOT:PSS processed without HBS, a trend of decreasing T_0 with increasing c_{PEDOT} can be observed, which can be described as $T_0 \propto c_{\text{PEDOT}}^{-0.35}$, as indicated by the black line. Again, connections are shown between data points which have been obtained in simultaneous measurements, confirming this trend. Figure 8b shows the conductivity prefactor for the same samples. The conductivity prefactor shows an increasing trend with c_{PEDOT} which can be described as $\sigma_0 \propto c_{\text{PEDOT}}^1$, as indicated by the black line. The weak dependence of the conductivity prefactor on the PEDOT:PSS ratio suggests that the system is no longer close to the percolation threshold where power law behavior is observed, cf. Figure 3. Rather, the linear dependence on concentration suggests a well-connected system, far beyond the percolation threshold. In this regime, the material conductivity becomes linearly proportional to the fraction of conductive material.

Conductivity enhancement in PEDOT:PSS due to processing with HBS has been extensively studied, resulting in several explanatory schemes. Many authors^{22,23,25,26} find evidence that HBS induce a phase segregation between PEDOT:PSS and PSSH, i.e. PSS which is not bound to PEDOT. This way, PSS barriers in the PEDOT-rich phase are reduced. Other schemes to explain the conductivity changes upon processing with HBS, which are sometimes used in combination, include conformational changes of PEDOT:PSS toward linear structures,^{15,19,22,24,25} the influence of screening by the polar character of the HBS^{6,15,22,24}, a change from polaron to bipolaron conduction¹⁵ and increased inter-chain coupling⁷.

Interpretation of the conduction mechanism is difficult because of the weak temperature dependence of the conductivity in Figure 7, reflected in the low values for T_0 in Figure 8a. Interpretation in terms of quasi-1D VRH behavior, as for the formulations without HBS, is awkward since the observed $(T_0/T)^{0.5} = 0.4 - 1.2$ is inconsistent with the requirement $(T_0/T)^{1/2} \gg 1$. In studies of PEDOT:PSS processed with HBS where the conductivity can no longer be correctly described by quasi-1D VRH, the change in conduction behavior is often described in the context of a metal-insulator transition.^{6,7,26} In this scenario the quantum mechanical overlap between sites originally involved in Mott VRH increases beyond the point where charges can be treated as being localized on a specific site. This causes a change in conduction behavior from VRH to the critical regime where $\sigma(T) \propto T^\beta$ with $\beta = 0.3 - 1$,⁵³ for which the reduced activation energy is constant: $W = \beta$.

Although Figure 7 does not show temperature independent reduced activation energies, the extracted values do match the expected values for β in the critical regime. We therefore tentatively conclude that we are in the crossover between quasi-1D VRH and the critical regime, where characteristics of VRH are still dominant.

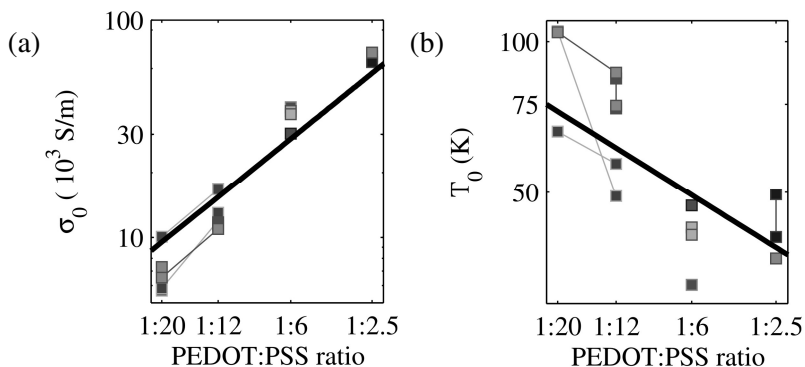


Figure 8. (a) Characteristic temperatures and (b) conductivity prefactors obtained from fits to the measured Ohmic conductivity as a function of temperature for two spin coated samples for all four PEDOT:PSS ratios processed with HBS each. Simultaneously measured data are connected by thin lines. Both figures are double-logarithmic plots, with the x-axis scaled as PEDOT concentration, c_{PEDOT} . The solid red line indicates a slope of (a) -0.35 and (b) 1.

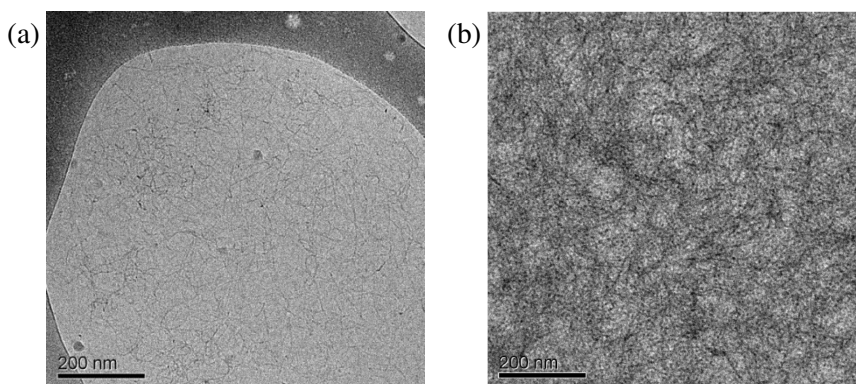


Figure 9. (a) Cryo-TEM image of PEDOT:PSS dispersion with HBS in the ratio 1:2.5. The darker area is the TEM grid. The typical diameter of the filaments is 4-5 nanometers and their length may reach tens to hundreds of nanometers. (b) HRTEM image of a dry specimen prepared from the same sample. The filaments look denser, and their diameter is smaller.

Figure 9a-b shows TEM images of vitrified dispersions (cryo-TEM) and dried layers (HRTEM) of PEDOT:PSS samples processed with HBS. In surprising similarity to native processed PEDOT:PSS, these are dominated by the presence of randomly oriented worm-like filaments. This similarity in morphology implies that processing with HBS changes the resulting PEDOT:PSS in a subtle way that cannot be resolved by TEM.

Recently, Yeo *et al.* showed that the suggested phase segregation between PEDOT-rich and PSSH-rich regions occurs in the vertical direction with the PSSH on top.¹⁰ Such a vertical phase segregation would both cause an increase in conductivity and be difficult to observe in TEM. However, simply extrapolating the results for native processed PEDOT:PSS according to the increased PEDOT:PSS ratio in the PEDOT-rich regions cannot explain the orders of magnitude increase in conductivity upon processing with HBS.⁵⁴ Instead, it is likely that processing with HBS causes a larger part of the filaments to contribute to the conduction. This will shift the network away from the percolation threshold, rationalizing the fact that the conductivity becomes linearly proportional to the PEDOT concentration. A schematic representation of this is given in Figure 5. This explanation requires that in the native processed PEDOT:PSS only a small fraction of the filaments takes part in conduction. This, in turn, resolves the seeming contradiction between the observation by TEM of a very dense filamentary network in dried layers of native processed PEDOT:PSS, and the dilute network with a typical length scale of ~100 nm evoked in the discussion of the conductivity: if all of the filaments observed in HRTEM would take part in conduction, the argument for the observed percolation behavior for native processed PEDOT:PSS would fail.

It is difficult to deduce from the data presented here the mechanism by which processing with HBS causes a larger part of the filaments to take part in conduction. One possibility is that the HBS would cause a strong reduction in the fraction of low-conductivity filaments, i.e. most filaments have become highly conductive and contribute to the conducting network. Alternatively the connectedness of the filaments could be increased by the processing with HBS, as suggested in Reference 7. Given the steep distance dependence of the tunneling rate between neighboring sites, small changes in the inter-filament distance could cause a much larger part of the filaments to participate in conductivity. Possibly, the presence of HBS which favorably interacts with PEDOT increases the relative surface area of PEDOT on the micelles, increasing this connectivity.

Conclusions

The conductivity of PEDOT:PSS as a function of temperature, electric field, and PSS:PEDOT ratio has been systematically characterized. The temperature dependence of the Ohmic conductivity for these materials is consistent with variable range hopping, in line with many other results.^{2,4,6,15,19,22,25,26,27,28} By adding more filler material (PSS) we are able to show that the conductivity prefactor depends strongly on the PEDOT concentration in the form of a power law, $\sigma_0 \propto c_{PEDOT}^{3.5}$, indicating percolation behavior. Since PEDOT:PSS in the ratio 1:20 is still conductive, the critical concentration at which percolation sets in is low and must be explained by conductive elements with a high aspect ratio, such as filaments. The percolating filament network can be regarded as a system of many quasi-1D wires in parallel, where the transport within the wires takes place by hopping. This configuration was previously shown to lead to the observed quasi-1D VRH behavior. TEM images of both the dispersion and dried layers of PEDOT:PSS confirm the presence of filaments. From previous observations PEDOT:PSS is expected to consist of PEDOT-rich structures with a PSS-rich shell,^{8,9,17,19,20,43,44} and hence we propose that these filaments consist of a PEDOT-rich core with a PSS-rich shell. This interpretation rationalizes both the observation of quasi-1D VRH and the critical percolation behavior found in the PEDOT concentration dependence of the conductivity prefactor. The non-Ohmic conductivity is well explained within the context of quasi-1D VRH, although the origin of the large localization length $\zeta = 10$ nm could not be uniquely determined.

PEDOT:PSS processed with HBS, having a much higher conductivity, shows the same quasi-1D VRH behavior, but the low characteristic temperature does not fully allow interpretation in terms of a VRH system. It is possible that PEDOT:PSS processed with HBS is close to the critical regime between a metal and an insulator. The conductivity prefactor shows a much weaker, linear dependence on the PEDOT concentration, $\sigma_0 \propto c_{PEDOT}$. Furthermore processing PEDOT:PSS with HBS does not cause significant changes in the morphology of the dried layers, as observed by TEM. This can be explained by a larger number of filaments participating in conduction after HBS treatment, either because of a smaller spread in conductivity or because of a larger probability for neighboring filaments to be connected.

Experimental

Sample Preparation

PEDOT:PSS dispersions were obtained from AGFA-Gevaert N.V. The dispersion used to prepare the samples is PEDOT:PSS ratio 1:2.5, which is commercially available without HBS as Orgacon ICP-1050 and with HBS as Orgacon HIL-1005. PEDOT:PSS ratios 1:2.5, 1:6, 1:12, 1:20, were prepared using the stock dispersion of PEDOT:PSS in ratio 1:2.5 with and without HBS. The PEDOT:PSS ratio was adapted using the PSS stock dispersion used during the polymerization of the PEDOT. Where necessary, water was added to obtain a PEDOT:PSS solid content of (0.90 ± 0.04) weight-%. This was followed by sonication to obtain homogeneous dispersions.

Samples for electrical measurements were prepared as follows, i.e. similar to Reference 9. The substrates consisted of $3 \times 3 \text{ cm}^2$ bare sodalime glass. They were first grooved into small pieces of $1 \times 1 \text{ cm}^2$ on the back side with a diamond pen, then sonicated in a bath of acetone for 10 minutes, cleaned with soap, rinsed with deionized water for 20 min and sonicated in a bath of isopropanol for 10 minutes. Residual organic contaminations were removed using a 30 min. UV-ozone treatment (UV-Ozone Photoreactor, PR-100, Ultraviolet Products).

The PEDOT:PSS dispersions were filtered using a $0.5 \text{ }\mu\text{m}$ filter and deposited in air by spin coating at 1000 RPM for 1 minute, followed by 3000 RPM for 1 minute to dry the layer. This typically resulted in layer thicknesses of 60 nm, 45 nm, 40 nm and 30 nm for native processed PEDOT:PSS in ratio of 1:2.5, 1:6, 1:12 and 1:20 respectively and in layer thicknesses of 70 nm, 55 nm, 55 nm and 50 nm for PEDOT:PSS processed with HBS in ratio of 1:2.5, 1:6, 1:12 and 1:20 respectively. After spin coating, samples were transferred into a glove box (O_2 and $\text{H}_2\text{O} < 1$ ppm) and subsequently annealed on a hot plate at $200 \text{ }^\circ\text{C}$ for a few minutes to remove residual water. Four electrodes ($1 \times 8 \text{ mm}$, 1 mm apart from each other) of 100 nm of gold were evaporated on top of each $1 \times 1 \text{ cm}^2$ piece.

After breaking the desired sample from the substrate, it was placed inside a cryostat (Oxford Instruments, modified for reaching low pressures) and evacuated to pressures below 10^{-6} mbar. The samples were exposed to air for a few minutes between the removal from the glove box and insertion into the cryostat. It was found that the room temperature conductivity only changes after exposure to air for

a few hours. Once placed, samples were degassed at 200 °C for a few hours to reach low pressures. This annealing step in vacuum did not alter the room temperature conductivity.

Electrical Characterization

Conductivity measurements were performed using a Keithley 2636a low current source-measure unit. The Ohmic conductivity was sampled continuously at 200 mV while the temperature was ramped at a rate of 1 K/min. The temperature ramping was interrupted for measurements of the non-Ohmic conductivity, which were performed at constant temperature after settling for 5 minutes. For samples with high conductivity and at high voltages, pulsed measurements and modeling of the temperature during the pulses were necessary to obtain reliable data as discussed in the Appendix. Long continuous measurements of ~24 hours were made possible using a LABVIEW control program. Temperature control was provided by an Oxford ITC 601 temperature controller that maintained temperature stability within ± 0.1 K. Measurements were performed in the range 4 -300 K, where the minimum temperature was limited by the finite thermal contact with the cold finger and the maximum temperature was chosen to prevent ionic currents which can deteriorate the samples. The thermometer of the Oxford ITC 601 is used for all measurements presented here. To estimate the uncertainty in the obtained temperature measurements, calibration measurements using an additional thermometer were performed. The additional thermometer was located on the cold finger on which also the sample was mounted. This measurement showed that the temperature difference between the additional thermometer and the temperature determined using the temperature controller was at most 2.5 K and occurred below 70 K. Above 70 K the temperature difference was at most 1 K.

Transmission Electron Microscopy at cryogenic temperatures (Cryo-TEM) and high resolution TEM (HRTEM)

Samples for cryo-TEM imaging were prepared by depositing a droplet of typically 5 μ L on perforated polymer film supported on a 300 mesh carbon coated electron microscope grid (copper, Ted Pella - lacey substrate). Ultra-thin films (10-250 nm) were formed as most of the dispersion was removed by blotting. The process was carried out in a controlled environment vitrification system where the temperature and the relative humidity are controlled, using an automatic Plunger- Freezer system by Leica (EM GP). The samples were examined at -178°C using a FEI Tecnai 12 G² TWIN TEM equipped with a Gatan 626 cold stage. Samples for

HRTEM imaging were prepared by placing a droplet of the dispersion on a TEM grid (300 mesh Cu, Ted Pella Ltd.) and allowing the solvent to evaporate.

Appendix

Extrapolation of I-V curves

At elevated temperatures, i.e. much above 100 K, it is difficult to reach the values of the electric field divided by temperature F/T required to reach the intermediate regime. For PEDOT:PSS in the ratio 1:2.5 the main limitation is that given its high conductivity, high fields cause severe heating of the layer. In the other cases the voltage was limited by the maximum voltage range of 200 V of the Keithley 2636a, and by the wiring inside the cryostat, of which we are not certain it could withstand much higher voltages. To overcome this problem, the data has been studied in detail to provide an empirical fit. This empirical fit extrapolates the low field data to the intermediate field regime in order to extract the hopping length $L(T)$ also at these temperatures.

Figure A1 shows a detailed study of the non-Ohmic conductivity for PEDOT:PSS in the ratio 1:6. To focus on the non-Ohmic behavior, the normalized strictly non-Ohmic part of the conductivity was studied, i.e. $(\sigma/\sigma_\Omega - 1)$. In the intermediate regime, according to Equation (2), $(\sigma/\sigma_\Omega - 1)$ is strictly a function of $F \times L/T$. Using Equation (3) in the quasi 1-D regime this reduces to $(\sigma/\sigma_\Omega - 1) = f(V/T^{1.5})$ in the intermediate regime. Figure A1 shows that curves for $(\sigma/\sigma_\Omega - 1)$ plotted against $V/T^{1.5}$ indeed show similar behavior in the region $10^{-2} < (\sigma/\sigma_\Omega - 1) < 4$, which contains not only the intermediate field regime, but also the low field regime. The behavior resembles a simple power law, with power 1.5, as indicated by the thick black line. This leads to the empirical fit:

$$\sigma = \sigma_\Omega (1 + x_1(T)V^{1.5}), \quad (\text{A5})$$

where $x_1(T)$ is a temperature dependent parameter.

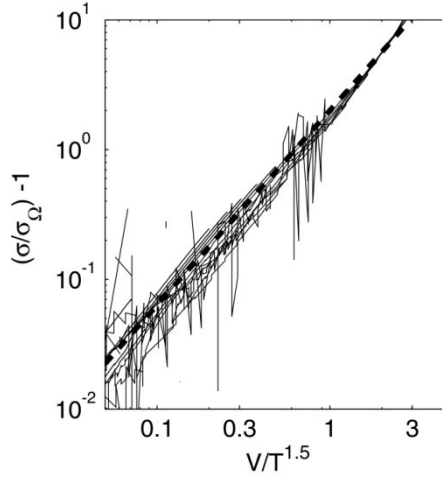


Figure A1. Normalized non-Ohmic conductivity data for PEDOT:PSS without HBS with ratio 1:6. The thin lines indicate represent measurements at different temperatures. The thick black line indicates the relation used for extrapolation to intermediate fields.

Modeling of heating during high voltage pulses

Modeling of heating was required to extract the non-Ohmic conductivity $G(V_0, T_0)$ of the highly conductive PEDOT:PSS in the ratio 1:2.5.

During a short pulse of length $\tau_p < d^2 / D$ where d indicates the thickness of the glass substrate and D the thermal diffusion constant of glass, the temperature can be estimated using the heating parameter $\eta = \left(A \sqrt{\pi \kappa \rho C_p} \right)^{-1}$, where A is the area the device, κ is the heat conductivity of glass, C_p is the heat capacitance of glass and ρ the density of glass. The temperature in the glass can be approximated from the one dimensional diffusion equation, where at the device side of the glass ($z = 0$), $\partial T / \partial z = 0$, so that heat can only be transported through the glass and not through the vacuum above. Furthermore, for a short pulse, the thickness of the glass can be treated as infinite. The solution for the temperature-profile is a Gaussian, such that at $z = 0$:

$$T(t) = T_0 + \eta \int_0^t \frac{P(t')}{\sqrt{t'}} dt', \quad (\text{A1})$$

where T_0 is the temperature before the pulse and $P(t)$ is the power as a function of time measured from the start of the pulse.

For glass at room temperature the following constants: $\kappa = 1\text{Wm}^{-1}\text{K}^{-1}$; $C_p = 880\text{ J kg}^{-1}\text{K}^{-1}$; $\rho = 2.4 \times 10^3\text{ kg m}^{-3}$; result in $\eta = 55.5\text{ K W}^{-1}\text{ s}^{-0.5}$ for a 7 mm^2 sample at RT.

Figure A2 a shows the conductance measured during a short 95 V pulse at 150 K. For this behavior a fit has been made, under the following approximations. Since the relative increase in conductivity is small, the power, $P(t)$, can be calculated using a constant conductance:

$$P = G(V_0, T_0)V^2(t). \quad (\text{A2})$$

Since both the current and voltage are recorded during the pulse, the voltage during the pulse is measured and approximated by the empirical equation:

$$V(t) = V_0(1 - \exp(\tau_{rise}^{-3}t^3)), \quad (\text{A3})$$

where the fit parameter τ_{rise} is in close agreement to the Keithley 2636a specifications. The measured conductivity can be approximated to be linear in temperature and this dependence can be estimated using the Ohmic conductivity $G_\Omega(T)$, resulting in:

$$G = G(V_0, T_0) \left[1 + T \left(\frac{d}{dT} \log G_\Omega \Big|_{T=T_0} \right) \right]. \quad (\text{A4})$$

Combining Equations (A1-A4) and using η and $G(V_0, T_0)$ as fit parameters, results in the dashed line in Figure A2a. Figure A2b shows the values of $\eta(T)$ which have been determined in this way. The measured values at room temperature are in good agreement to the predicted value of $\eta = 55.5\text{ K W}^{-1}\text{ s}^{-0.5}$.

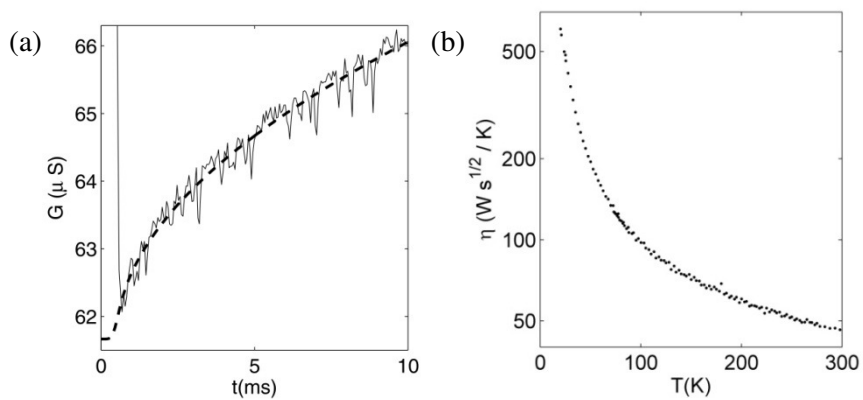


Figure A2. (a) Fit of the conductivity during a 95 V voltage pulse causing heating of the PEDOT:PSS layer. $T_0 = 150$ K, PEDOT:PSS ratio 1:2.5, native processed. (b) Measurement of the heating parameter, using the conductivity increase of PEDOT:PSS as a temperature measurement.

References

- ¹ Y. H. Kim, C. Sachse, M. L. Machala, C. May, L. Müller-Meskamp, K. Leo, *Adv. Funct. Mater.* **2011**, *21*, 1076.
- ² Y. Xia, K. Sun, J. Ouyang, *Adv. Mater.* **2012**, *24*, 2436.
- ³ A. Aleshin, R. Kiebooms, R. Menon, A. J. Heeger, *Synth. Met.* **1997**, *90*, 61.
- ⁴ Y. Cao, A. E. Kovalev, R. Xiao, J. Kim, T. S. Mayer, T. E. Mallouk, *Nano Lett.* **2008**, *8*, 4653.
- ⁵ J. L. Duvail, P. Rétho, V. Fernandez, G. Louarn, P. Molinié, O. Chauvet, *J. Phys. Chem. B* **2004**, *108*, 18552.
- ⁶ J. Y. Kim, J. H. Jung, D. E. Lee, J. Joo, *Synth. Met.* **2002**, *126*, 311.
- ⁷ N. Kim, B. H. Lee, D. Choi, G. Kim, H. Kim, J.-R. Kim, J. Lee, Y. H. Kahng, K. Lee, *Phys. Rev. Lett.* **2012**, *109*, 106405.
- ⁸ A. M. Nardes, M. Kemerink, R. A. J. Janssen, J. A. M. Bastiaansen, N. M. M. Kiggen, B. M. W. Langeveld, A. J. J. M. van Breemen, M. M. de Kok, *Adv. Mater.* **2007**, *19*, 1196.
- ⁹ A. M. Nardes, M. Kemerink, R. A. J. Janssen, *Phys. Rev. B* **2007**, *76*, 085208.
- ¹⁰ J.-S. Yeo, J.-M. Yun, D.-Y. Kim, S. Park, S.-S. Kim, M.-H. Yoon, T.-W. Kim, S.-I. Na, *ACS Appl. Mater. Interfaces* **2012**, *4*, 2551.
- ¹¹ A. J. Kronemeijer, E. H. Huisman, I. Katsouras, P. A. van Hal, T. C. T. Geuns, P. W. M. Blom, S. J. van der Molen, D. M. de Leeuw, *Phys. Rev. Lett.* **2010**, *105*, 156604.
- ¹² I. Katsouras, A. J. Kronemeijer, E. C. P. Smits, P. A. van Hal, T. C. T. Geuns, P. W. M. Blom, D. M. de Leeuw, *Appl. Phys. Lett.* **2011**, *99*, 013303.
- ¹³ O. Bubnova, Z. U. Khan, A. Malti, S. Braun, M. Fahlman, M. Berggren, X. Crispin, *Nat. Mater.* **2011**, *10*, 429.
- ¹⁴ D. S. H. Charrier, R. A. J. Janssen, M. Kemerink, *Chem. Mater.* **2010**, *22*, 3670.
- ¹⁵ J. Ouyang, Q. Xu, C.-W. Chu, Y. Yang, G. Li, J. Shinar, *Polymer* **2004**, *45*, 8443.
- ¹⁶ T. Takano, H. Masunaga, A. Fujiwara, H. Okuzaki, T. Sasaki, *Macromolecules* **2012**, *45*, 3859.
- ¹⁷ G. Greczynski, T. Kugler, M. Keil, W. Osikowicz, M. Fahlman, W. Salaneck, *J. Electron. Spectrosc. Relat. Phenom* **2001**, *121*, 1.
- ¹⁸ U. Lang, E. Müller, N. Naujoks, J. Dual, *Adv. Funct. Mater.* **2009**, *19*, 1215.
- ¹⁹ A. M. Nardes, R. A. J. Janssen, M. Kemerink, *Adv. Funct. Mater.* **2008**, *18*, 865.
- ²⁰ J. Hwang, F. Amy, A. Kahn, *Org. Electron.* **2006**, *7*, 387.
- ²¹ C. Ionescu-Zanetti, A. Mechler, S. A. Carter, R. Lal, *Adv. Mater.* **2004**, *16*, 385.
- ²² Y. Xia, J. Ouyang, *J. Mater. Chem.* **2011**, *21*, 4927.
- ²³ X. Crispin, F. L. E. Jakobsson, A. Crispin, P. C. M. Grim, P. Andersson, A. Volodin, C. van Haesendonck, M. Van der Auweraer, W. R. Salaneck, M. Berggren, *Chem. Mater.* **2006**, *18*, 4354.
- ²⁴ H. Okuzaki, Y. Harashina, H. Yan, *Eur. Polym. J.* **2009**, *45*, 256.
- ²⁵ T. Wang, Y. Qi, J. Xu, X. Hu, P. Chen, *Appl. Surf. Sci.* **2005**, *250*, 188.

- ²⁶ C. S. Suchand Sangeeth, M. Jaiswal, R. Menon, *J. Phys. Condens. Matter* **2009**, *21*, 072101.
- ²⁷ S. Samitsu, T. Shimomura, K. Ito, M. Fujimori, S. Heike, T. Hashizume, *Appl. Phys. Lett.* **2005**, *86*, 233103.
- ²⁸ A. N. Aleshin, S. R. Williams, A. J. Heeger, *Synth. Met.* **1998**, *94*, 173.
- ²⁹ J. Joo, S. M. Long, J. P. Pouget, E. J. Oh, A. G. MacDiarmid, A. J. Epstein, *Phys. Rev. B* **1998**, *57*, 9567.
- ³⁰ E. Abrahams, P. W. Anderson, D. C. Licciardello, T. V. Ramakrishnan, *Phys. Rev. Lett.* **1979**, *42*, 673.
- ³¹ A. S. Rodin, M. M. Fogler, *Phys. Rev. Lett.* **2010**, *105*, 106801.
- ³² K. Maschke, H. Overhof, P. Thomas, *Phys. Stat. Solidi (b)* **1974**, *61*, 621.
- ³³ A. S. Rodin, M. M. Fogler, *Phys. Rev. B* **2009**, *80*, 155435.
- ³⁴ B. I. Shklovskii and A. L. Efros, *Electronic Properties of Doped Semiconductors*, Springer-Verlag: Berlin 1984, ISBN 3-540-12995-2
- ³⁵ Not all references shown explicitly mention values of T_0 , in those cases we have extracted T_0 from Figures of the data.
- ³⁶ C. L. Pint, Y.-Q. Xu, E. Morosan, R. H. Hauge, *Appl. Phys. Lett.* **2009**, *94*, 182107.
- ³⁷ F. J. Rueß, A. P. Micolich, W. Pok, K. E. J. Goh, A. R. Hamilton, M. Y. Simmons, *Appl. Phys. Lett.* **2008**, *92*, 052101.
- ³⁸ Z.-M. Dang, K. Shehzad, J.-W. Zha, A. Mujahid, T. Hussain, J. Nie, C.-Y. Shi, *Compos. Sci. Technol.* **2011**, *72*, 28.
- ³⁹ Y. P. Mamunya, *J. Macromol. Sci. B* **1999**, *38*, 615.
- ⁴⁰ C. D. Lorenz, R. M. Ziff, *J. Chem. Phys.* **2001**, *114*, 3659.
- ⁴¹ Y. B. Yi, E. Tawerghi, *Phys. Rev. E* **2009**, *79*, 041134.
- ⁴² M. Foygel, R. D. Morris, D. Anez, S. French, V. L. Sobolev, *Phys. Rev. B* **2005**, *71*, 104201.
- ⁴³ G. Zotti, S. Zecchin, G. Schiavon, F. Louwet, L. Groenendaal, X. Crispin, W. Osikowicz, W. Salaneck, M. Fahlman, *Macromolecules* **2003**, *36*, 3337.
- ⁴⁴ B. Friedel, T. J. K. Brenner, C. R. McNeill, U. Steiner, N. C. Greenham, *Org. Electron.* **2011**, *12*, 1736.
- ⁴⁵ M. E. Raikh, I. M. Ruzin, *Sov. Phys. JETP* **1989**, *68*, 642.
- ⁴⁶ P. Sheng, B. Abeles, Y. Arie, *Phys. Rev. Lett.* **1973**, *31*, 44.
- ⁴⁷ L. Zuppiroli, M. N. Bussac, S. Paschen, O. Chauvet, L. Forro, *Phys. Rev. B* **1994**, *50*, 5196.
- ⁴⁸ M. Pollak, I. Riess, *J. Phys. C* **1976**, *9*, 2339.
- ⁴⁹ D. J. Griffiths, *Introduction to quantum mechanics*; Pearson Prentice Hall, 2005.
- ⁵⁰ In ref. 4 using the slope in Figure 4 and Equation (2), it can be determined that $L = 1.2$ nm at 10 K. Using Equation (3) this results in $\xi = 0.07$ nm.
- ⁵¹ J. W. van der Horst, *The electronic and optical properties of conjugated polymers*, PhD Thesis Eindhoven University of Technology, 2001.

⁵² B. I. Shklovskii, *Sov. Phys. Semicon.* **1977**, *10*, 855.

⁵³ A. I. Larkin, *Sov. Phys. JETP* **1982**, *56*, 647.

⁵⁴ Increasing the conductivity from $\sigma_0 = 1.8 \cdot 10^3$ S/m for native PEDOT:PSS in the ratio 2:5 to $\sigma_0 = 6.3 \cdot 10^4$ S/m for PEDOT:PSS in the ratio 1:2.5 processed with HBS requires according to $\sigma_0 \propto C_{\text{PEDOT}}^{3.5}$ an effective PEDOT:PSS ratio of 4:1 at the bottom of the PEDOT:PSS layer, which is unlikely high.

Chapter 5:

The curious out-of-plane conductivity of PEDOT:PSS

Abstract

For its application as transparent conductor in light-emitting diodes and photovoltaic cells, both the in-plane and out-of-plane conductivity of PEDOT:PSS are important. However, studies into the conductivity of PEDOT:PSS rarely address the out-of-plane conductivity and those that do, report widely varying results. Here we present a systematic study of the out-of-plane charge transport in thin films of PEDOT:PSS with varying PSS content. To this end, we enclose the PEDOT:PSS in small vias between metallic contacts. An unexpected, but strong dependence of the conductivity on via diameter is observed. The change in conductivity correlates with a diameter dependent change in PEDOT:PSS layer thickness. We suggest that the more than three orders of magnitude variation in out-of-plane conductivity with only a 3-4-fold layer thickness variation can quantitatively be explained on basis of a percolating cluster model. This model describes the probability for conductive paths between the top and bottom electrode to be formed from randomly placed conductive elements in an insulating matrix, and shows that for thin layers this probability strongly decreases with increasing layer thickness. The results also rationalize previously unexplained findings in molecular junctions where PEDOT:PSS is used as contact electrode.

Introduction

The conductive polyelectrolyte poly(3,4-ethylenedioxythiophene):poly(styrene-sulfonate) (PEDOT:PSS) is commonly used as transparent electrode in organic light emitting diodes and in organic or hybrid photovoltaic cells. In early applications, PEDOT:PSS was merely used for planarization and to stabilize the workfunction of tin-doped indium oxide (ITO). To prevent cross talk typically low conductivity PEDOT:PSS formulations were used, made by deliberately increasing the amount of PSS, so that only the out-of-plane conductivity was of importance. Recent efforts are aimed at fully replacing the expensive and brittle ITO layer with PEDOT:PSS.^{1,2} This leads to the additional requirement of a high in-plane conductivity to distribute the current across the device. This can be achieved by processing the emulsion with the addition of a high boiling solvent (HBS) such as ethylene glycol (EG), which is able to increase the in-plane conductivity of PEDOT:PSS to 1.4×10^5 S/m.¹

Many studies have been performed in which the in-plane conductivity is addressed. Only a few studies have been performed that measure the out-of-plane conductivity and they report widely varying results. Nardes *et al.*^{3,4} found for the PEDOT:PSS with PEDOT:PSS ratio 1:6, a large anisotropy in the in- and out-of-plane conductivity, roughly a factor 400, which was explained by the anisotropy in the granular structure as revealed by cross-sectional atomic force microscopy (AFM). The out-of-plane conductivity was found to show an Arrhenius-type temperature dependence, while the in-plane conductivity showed a non-Arrhenius temperature dependence best explained using variable range hopping (VRH).^{3,4} In studies towards self-assembled monolayer (SAM) electronics, van Hal *et al.*⁵ found an anisotropy of 1000. Na *et al.*^{6,7} have studied the influence of high boiling solvents on the conductivity using different techniques and found that adding different amounts of solvent can change the anisotropy from 7 to 50 and from 2000 to 30000 for two different PEDOT:PSS formulations.

To gain understanding of the out-of-plane conductivity, we present a systematic investigation of the out-of-plane conductivity of PEDOT:PSS of varying composition. A major problem in measuring the out-of-plane conductivity of highly conductive PEDOT:PSS formulations is that the thin film resistance easily drops below the contact resistance, hindering the acquisition of useful data. For the present PEDOT:PSS formulations this requires devices to have areas less than roughly $100 \mu\text{m}^2$.⁸ Therefore, we use devices which consist of circular

interconnects (vias) in an insulating photoresist layer sandwiched between two metallic electrodes. The analyzed via diameters vary between 2 μm and 100 μm . A strong diameter dependence of the out-of plane conductivity is observed. Hence, the anisotropy of the conductivity is diameter dependent. This dependence is very strong, several orders of magnitude, and is consistent between all PEDOT:PSS ratios measured. These facts hint at the existence of a fundamental underlying mechanism. Unraveling this mechanism is the main topic of this article.

Results

Figure 1 shows the measured out-of-plane conductivity as a function of via diameter for PEDOT:PSS in the ratios of 1:2.5, 1:6, 1:12 and 1:20. Much of the 14 orders of magnitude spread between the largest and smallest measured values is caused by shorts and disconnected devices. Such devices often have atypical I - V curves,⁹ indicated in the graphs by plusses instead of squares as markers. Since the highly conductive shorts fully determine the averages, percentiles have been studied instead. The five lines in each graph show for each diameter, from bottom to top, the 20%, 40%, 50%, 60%, and 80% percentiles of the complete set of all measured values. Remarkably, for all PEDOT:PSS ratios there remains a very strong trend in conductivity as a function of diameter that is larger than the typical spread between the 20% and 80% percentiles. Furthermore, there appears an increase in the scatter for devices with lower PEDOT:PSS ratio.

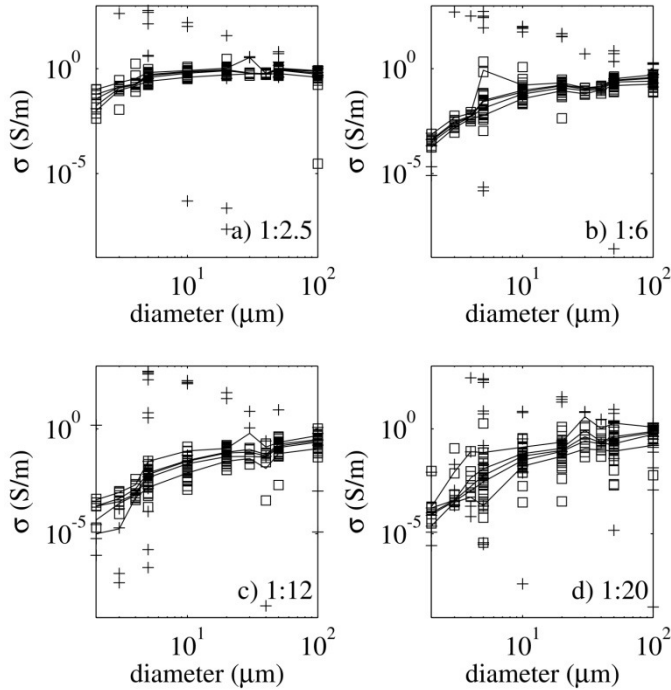


Figure 1. Measured conductivities for devices with PEDOT:PSS ratio 1:2.5, 1:6, 1:12 and 1:20. The solid lines indicate the 20%, 40%, 50%, 60% and 80% percentiles (bottom to top) of the full dataset.. Crosses instead of squares indicate measurements with an atypical I-V curve.⁹

Figure 2a shows the median of the out-of-plane conductivity for two different types of substrates as a function of via diameter for PEDOT:PSS in the ratios of 1:2.5, 1:6, 1:12 and 1:20. All devices consistently show an orders of magnitude decrease in conductivity with decreasing diameter. The devices can be divided into groups with similar conductivities. Since a physical interpretation is yet missing, these groups will be phenomenologically described by the function $\sigma \propto \left[\exp((d_0 / d)^{1/2}) + Rc \right]^{-1}$, where d_0 is a typical length scale and $Rc = 6 \Omega$ is the typical resistance of the gold strips between the probe needles and the via. The first group, i.e. the devices with PEDOT:PSS ratio 1:2.5, is well described by the typical length scale $d_0 = 25 \mu\text{m}$ indicated by the upper dashed line. The second group, consisting of all other PEDOT:PSS ratios, i.e. 1:6, 1:12 and 1:20, seems well approximated by the lower dashed line, following the same relation with $d_0 = 100 \mu\text{m}$. This is in stark contrast to the in-plane conductivity studied in Chapter 4,

which shows that the in-plane conductivities of PEDOT:PSS with ratios 1:6 and 1:20 differ by almost two orders of magnitude.

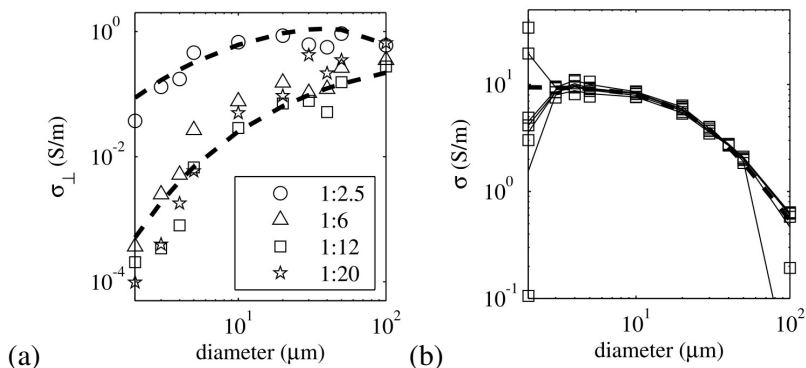


Figure 2. (a) Median conductivities for devices with PEDOT:PSS ratio 1:2.5, 1:6, 1:12 and 1:20. The black thick dashed lines are the result of an empirical relations (discussed in the main text) which takes into account a contact resistivity of $R_c = 6 \Omega$. (b) Measured conductivities (squares) for PEDOT:PSS of type 'ICP 1020' to which a HBS has been added. The solid lines indicate the 20%, 40%, 50%, 60% and 80% percentiles. The thick dashed line shows a constant conductivity of 10 S/m taking into account a contact resistance $R_c = 10 \Omega$.

For comparison, the conductivity for the PEDOT:PSS type ICP 1020 with HBS has been measured. The result is shown in Figure 2b. Similar to Figure 1, all measured values are shown together with their percentiles. The spread in measurement values is very small. In contrast to the materials without HBS, the data is well described by the black dashed line, which shows the theoretical result for a diameter independent conductivity of 10 S/m, taking into account a contact resistance $R_c = 10 \Omega$. Devices with a diameter of 2 μm , however, do not yield consistent results. The diameter independent conductivity combined with a measured in-plane conductivity of $32 \cdot 10^3 \text{ S/m}$, shows that this PEDOT:PSS type has a very high in-plane/out-of-plane anisotropy of 3200.

In Chapter 4 it was shown that the in-plane conductivity shows a power law relation as a function of PEDOT concentration, c_{PEDOT} , namely $\sigma_{\parallel} \propto C_{\text{PEDOT}}^{3.5}$. Using these results for the in-plane conductivity σ_{\parallel} and combining them with the median out-of-plane conductivities σ_{\perp} from Figure 2a results in the median anisotropy, $\sigma_{\parallel} / \sigma_{\perp}$, as a function of diameter for the different PEDOT:PSS ratios as shown in Figure 3a. The effect of the contact resistance is reflected in the small upturn at 100 μm of the continuous line which shows the empirical relation describing the PEDOT:PSS with ratio 1:2.5. The observed range of anisotropies stretches over

four orders of magnitude and covers all previously published anisotropy values.^{3,4,5,6,7} To study the dependence of the anisotropy on the PEDOT:PSS ratio, the anisotropy for devices with a diameter of 50 μm is shown in Figure 3b. For this diameter the trend in conductivity with diameter has largely settled, and contact resistance effects are small. The experimental data is well described by the relation $\sigma_{\parallel}/\sigma_{\perp} = 1.1 \times 10^4 c_{\text{PEDOT}}^{2.5}$, shown as the dashed line in Figure 3b.

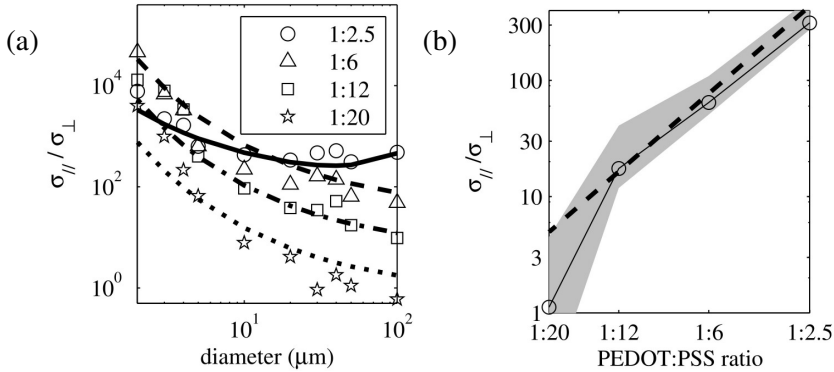


Figure 3. (a) The room temperature in-plane conductivity for the different PEDOT:PSS ratios. The black line indicates a power law relation with power 3.5. (b) The in-plane / out-of-plane anisotropies in the conductivity based on Figure 2a. The continuous, dashed, dash-dotted and dotted lines indicate the anisotropies based on the empirical relations shown in Figure 2a for devices with PEDOT:PSS ratio 1:2.5, 1:6, 1:12 and 1:20 respectively. (c) Double logarithmic plot of the measured median anisotropies (connected circles). for a via diameter of 50 μm , where the x-axis is scaled as the PEDOT concentration. The gray patch indicates the region between the 20% and 80% percentile of the data. The dashed line indicates a power law dependence with exponent 2.5.

The diameter dependence of the conductivity and the anisotropy is very strong, both vary by nearly four orders of magnitude, and the variation is consistent between all PEDOT:PSS ratios 1:6, 1:12 and 1:20. These facts hint at the existence of a fundamental underlying mechanism. This mechanism will also have to explain the reduced diameter dependence for the ratio 1:2.5 and the lack of diameter dependence in the samples of PEDOT:PSS type ICP1020.

In addition to the conductivity and anisotropy dependence on diameter, our devices also show a layer thickness dependence on diameter. To study and quantify this dependence, AFM measurements have been performed on finished devices, as shown in Figure 4. The inset in Figure 4a shows a topographic image of the top gold electrode of the device. In the middle of the image the via is visible as a

depression, the depth of which is measured along the cross-section indicated by the white dotted line, and plotted in the main panel of Figure 4a. Considering the device layout shown in Figure 5a, the depth of the observed dip should be equal to the nominal thickness of the photoresist layer of 520 nm. If, however, the PEDOT:PSS layer thickness inside the via is larger than outside the via, this results in a reduction in the measured depth of the device.

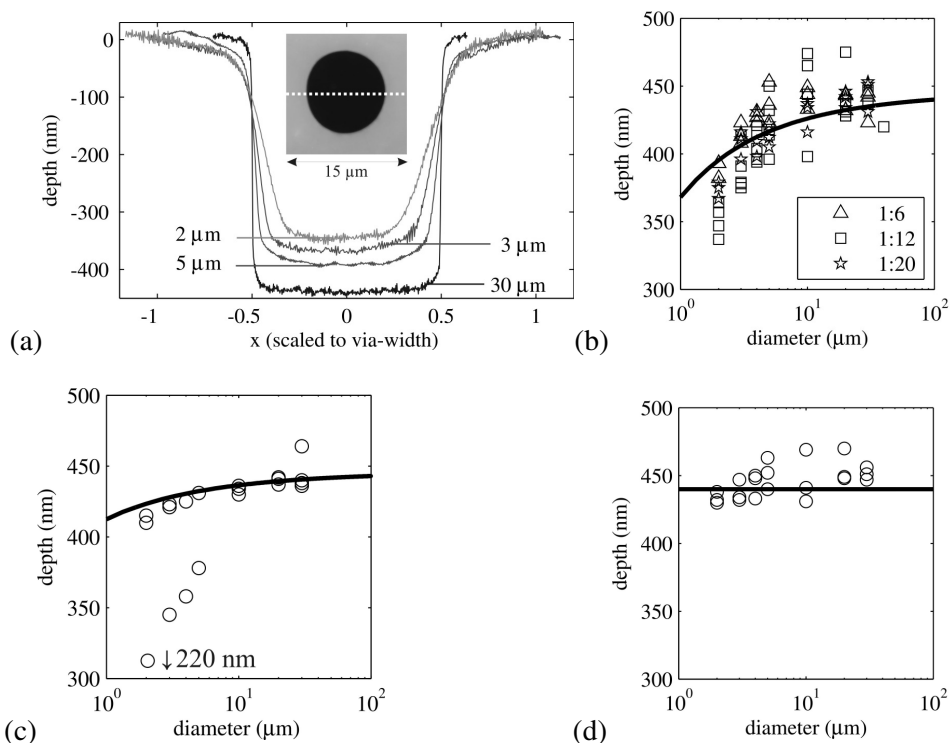


Figure 4. (a) Inset: a topographic AFM image of a 10 μm device. The dashed white line indicates the typical location for the cross-sections shown in the main panel. The cross-sections are shown to the scale of the device-width and are measured on a substrate with PEDOT:PSS ratio 1:12. (b)-(d) Depths determined by cross-sections as shown in (a) for (b) PEDOT:PSS with ratios 1:6, 1:12 and 1:20, (c) PEDOT:PSS of ratio 1:2.5 and (d) PEDOT:PSS type 'ICP1020'. Lines are calculated from Equation (1).

To investigate the PEDOT:PSS layer thickness dependence on diameter, the depth of devices for PEDOT:PSS in the ratios 1:6, 1:12 and 1:20 is shown in Figure 4b. Figures 4c and d show the same for PEDOT:PSS in the ratio 1:2.5 and for PEDOT:PSS type ICP1020, respectively. For Figures 4b and c there is a decrease in depth with decreasing diameter, which can be related to an increase in

PEDOT:PSS layer thickness. An alternative explanation could be that there is a systematic change of photoresist layer thickness with device diameter. To avoid such systematic errors, we measured devices both at the center and at the edge of the substrate; thereby the influence of systematic thickness variations of the photo resist layer is ruled out. Alternative scenarios that might give rise to an apparent diameter dependent layer thickness like shadow effects during the gold evaporation or photo resist thickness variations related to the etching of the vias can be ruled out since they would equally affect all devices in Figures 4b-d, which is clearly not the case. We therefore attribute the observed depth variations to variations in PEDOT:PSS layer thickness in the vias, most likely caused by a diameter- and material-dependent interplay between viscosity, surface tension and contact-line pinning during the spin coating.

Summarizing the data in Figures 2, 3 and 4, for the PEDOT:PSS formulations without HBS there is a significant diameter dependence both in the conductivity and in the PEDOT:PSS layer thickness. As such, also the conductivity anisotropy is diameter dependent. In principle, these dependencies may result from different mechanisms. However, there is a clear correlation between the degree of thickness variation and the degree of conductivity variation: the PEDOT:PSS formulations that give rise to the strongest thickness variation, i.e. 1:6, 1:12 and 1:20, also show the most pronounced conductivity variation. The ICP 1020 material shows neither a thickness nor a conductivity variation. The 1:2.5 material lays in between, both in thickness and in conductivity variation. This strongly suggests that there is a causal relation between thickness and out-of-plane conductivity. However, for a homogeneous Ohmic conductor a 3-4-fold layer thickness variation should not lead to a conductivity variation by several orders of magnitude. In the next section we provide an interpretation of this surprisingly strong dependence of conductivity on diameter.

Discussion

Our experimental data shows that for certain PEDOT:PSS formulations both the thickness of the layer and its out-of-plane conductivity are dependent on the device diameter. To explain these experimental observations, several scenarios, such as the contribution of the in-plane-conductivity, a PSS top layer model, phase separation between PEDOT-rich and PSS-rich material, highly conductive filaments, charge transport in a layered morphology and a percolation cluster

model are considered in this section, some of these are schematically shown in Figure 5.

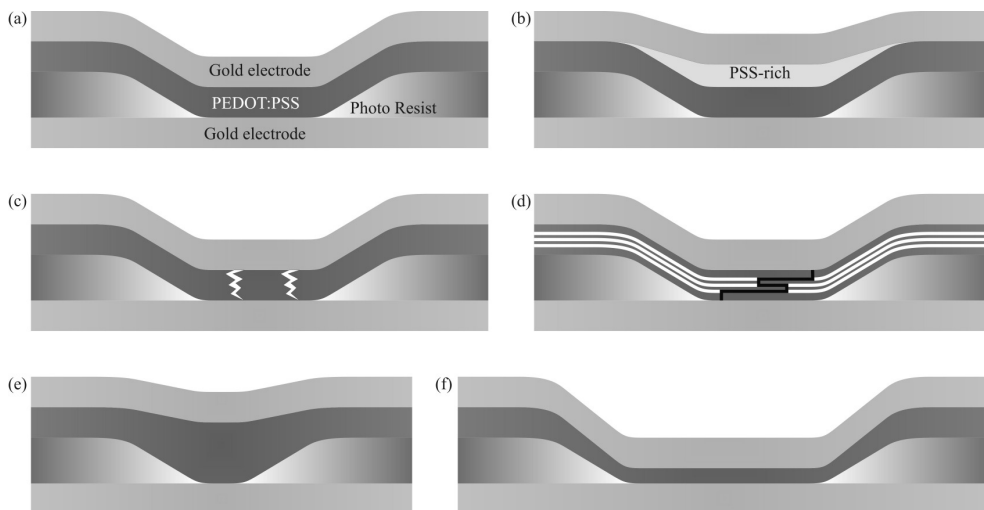


Figure 5: Schematic representation of (a) the device used for measuring the out-of-plane conductivity and (b-f) models to explain the diameter dependence of the determined out-of-plane conductivity. (b) A PSS layer of which the thickness is diameter dependent. (c) A few highly conductive filaments which cause a diameter dependent median conductivity. (d) A ‘lasagna’, i.e. layered model, in which layers are connected by a few highly conductive shorts, resulting in a diameter dependent average conductivity. (e-f) A diameter dependence of the layer thickness, which in a percolating system causes a diameter dependent conductivity.

The contribution of in-plane conductivity

First we discuss the influence of the in-plane conduction in the region surrounding the intended via, i.e. area where the bottom gold electrode contacts the PEDOT:PSS. Since the in-plane conductivity is higher than the out-of-plane conductivity and the top electrode contacts the entire layer, it is possible that the PEDOT:PSS on top of the photoresist contributes substantially to the measured out-of-plane conductivity. This effectively increases the area over which the out-of-plane conductivity is measured. This effect would be strongest for devices with small diameters, since there a small increase in effective area causes a relatively bigger effect. The result would be an increase in the conductivity with smaller diameters, which is opposite to what is observed in Figure 2a, and therefore this mechanism can be ruled out.

PSS top layer model

Figure 5b is a schematic representation of a possible diameter dependent thickness of a PSS-rich top-layer.^{6,10} It cannot be excluded that during the evaporation step of the spin-coating process, the PSS preferentially moves into the vias. This could be caused by a difference in hydrophobicity between the gold electrode and the photo resist layer, or possibly by a temperature gradient which occurs due to the difference in thermal conductivity between the gold electrodes and the photo resist layer. Furthermore, this could also explain the dependence of layer thickness on device diameter shown in Figure 4. The influence of the PSS-rich top layer has been studied in Reference 6, where the out-of-plane conductivity and PSS concentration of the top-layer were measured for polar solvent-treated PEDOT:PSS layers. Although a significant change in top-layer PSS concentration was reached, this resulted in an out-of-plane conductivity change of less than a factor two. Furthermore a study of the bias dependence of the conductivity, shown in the Appendix, finds that the bias dependence increases for smaller diameters. Adding an insulating top PSS layer for smaller diameters would result in smaller fields, and therefore cause a smaller bias dependence. Based on these arguments, we exclude a diameter dependent thickness of the top PSS layer as an explanation for the orders of magnitude change in conductivity with diameter. Furthermore, it is expected that during the evaporation of the top contact, some gold penetrates this layer, which therefore shunts this PSS-barrier.

Phase separation between PEDOT-rich and PSS-rich regions

It has often been shown that PEDOT:PSS can phase separate into PEDOT-rich and PSS-rich regions, with important consequences for the conductivity.^{6,11,12,13,14} Such phase separation could occur differently for devices with different diameters, because of their different layer thickness. That is, a thicker layer takes longer to dry and allows a longer time for phase separation to occur. Although enhanced phase separation is commonly reported for PEDOT:PSS processed with HBS,^{6,11,12,14,15} it is, to our knowledge, not reported for PEDOT:PSS processed without HBS. Furthermore, phase separation in PEDOT:PSS is typically understood to cause an increase in conductivity, while in the data presented here devices with thicker layers, which would be expected to have more pronounced phase separation, have a much lower conductivity. As a further test, we exposed an PEDOT:PSS sample to water vapor, while keeping it elevated temperatures and measured the (in-plane) conductivity. Continuing this treatment for a few hours did not lead to any

appreciable changes apart from a minor decrease in conductivity, i.e. incomparable to the observed change of three orders of magnitude. Combined these arguments make (diameter dependent) phase separation as an explanation for the strong diameter dependence of the out-of-plane conductivity highly unlikely.

Filament-conduction model

Figure 5c indicates the possibility that rare, but highly conductive filaments determine the conductivity of the whole device. The importance of such filaments for the out-of-plane conductivity of thin films has been suggested in literature.^{16,17,18} Indeed, this explanation does not require diameter dependent material constants and is able to create a diameter dependent median conductivity. However a more detailed calculation shows that it cannot explain our data. The argument goes as follows. Our data indicates that the probability for a 2 μm device to have a conductivity less than 5×10^{-4} S/m is $29 / 35 = 0.83$, while the same probability for a 4 μm device is $3 / 32 = 0.094$. However, if we consider the 4 μm device to be made up out of 4×2 μm devices, than the probability to have a conductivity smaller than $5 \cdot 10^{-4}$ S/m should have been at least $(0.83)^4 = 0.47$. This discrepancy cannot be explained by a statistical difference in shorted devices between devices of diameters 2 μm and 4 μm , since this would require more than 20 of the devices with 4 μm diameter to be shorted. It is therefore concluded that rare but highly conductive filaments do not explain the diameter dependence of the median conductivity. A generalization of the above calculation is given in the Appendix.

Connected layers model

Figure 5d indicates a layered structure of the PEDOT:PSS, where only a few highly conductive filaments or shorts connect neighboring highly conducting layers. Such a structure seems likely in view of cross-sectional AFM performed in Reference 4, which reveals a strongly anisotropic structure attributed to drying effects during spin coating. Although this model is very similar to the one shown in Figure 5c, the total conductivity here is limited to the worst connection between two consecutive layers. This way, not only the median conductivity is diameter dependent, but also the average conductivity is diameter dependent. If in an N -layer system with total thickness L , highly conductive filaments are Poisson distributed as one filament of conductivity G_F per area A_F , then a step in conductivity as a function of diameter appears where the device area equals A_F . Below this diameter the probability for a highly conducting connection between all layers is highly unlikely, while above

this diameter not having such a connection for all layers becomes unlikely. If the resistivity of the in-plane layers is neglected, the conductivity steps to $N G_F L / A_F$. As shown in the more detailed discussion of this model in the Appendix, by choosing the right distribution of filaments with different conductivities, the diameter dependence of the conductivity for PEDOT:PSS in the ratios 1:6, 1:12 and 1:20 can be well reproduced. Unfortunately this requires filaments with $G_F \gg 10 G_0$, where G_0 is the quantum of conductance, the maximum conductivity for a system where a single quantum state mediates the conductivity. It is unlikely that a single filament, as investigated for this material in Chapter 4, can have a conductivity much higher than $10 G_0$. With this restriction, the layered structure can only explain a small part of the curves in Figure 2, up to diameters of 5-10 μm . Again, a more detailed discussion of this model is given in the Appendix.

Percolating cluster model

From our detailed analysis of the field, temperature and composition dependence of the in-plane conductivity, presented in Chapter 4, we know that the thin layers of the PEDOT:PSS formulations without HBS are percolating systems of quasi-1D filaments near the percolation threshold. In a broader perspective, percolation is typically a necessary ingredient for the interpretation of transport results in PEDOT:PSS.^{3,4,14,19,20} This powerful theory describes the formation of connected, i.e. conductive, networks when conductive elements are successively added to an insulating matrix.²¹ Most notably, the theory predicts that there exists a percolation threshold, i.e. a specific density of conductive elements beyond which macroscopic conduction occurs. Only above the percolation threshold does the system contain a connected network of infinite size. In concentrations close to the percolation threshold the system is in a critical regime, which means that a power law dependence on (changes in) the concentration of conductive elements occurs for many observables of the system, such as the conductivity or the probability of finding clusters of a particular size. Applying percolation theory to thin layers is difficult, since these layers are neither two dimensional nor three dimensional. Instead, a cross-over is expected to occur with increasing layer thickness.^{22, 23} For the out-of-plane conductivity this means that the connected network responsible for conduction no longer needs to be infinitely large, but needs merely to have a size equal to the thickness of the layer. Early work uncovered interesting phenomena for such thin percolating systems, such as the following dependence of the out-of-plane conductivity on layer thickness:^{23,16,17}

$$\sigma \propto \exp[-(44.6L / \zeta)^{1/2}], \quad (1)$$

where L denotes the layer thickness, and ζ denotes the localization length, i.e. the length scale of the exponential decay of the localized electronic states. This equation reflects the fact that the probability of finding clusters with a size of at least the film thickness, i.e. that connect the electrodes, strongly decays with increasing thickness. Equation (1) holds for thin layers, i.e. small values of L / ζ . However, in Reference 23, good agreement between experiment and theory is reached even for $L / \zeta \approx 300$. In Chapter 4 the localization length for the present PEDOT:PSS emulsions has been determined to be $\zeta = 10$ nm, whereas the layer thickness here varies between ~ 40 nm and ~ 140 nm. Although Equation (1) has been derived for variable range hopping (VRH) in an isotropic system, similar relations are expected for the conductivity of the PEDOT:PSS films studied here, where the conductivity is determined by percolation through a 3D network of quasi-1D filaments, as shown in Chapter 4. Therefore, a strong dependence of the conductivity on layer thickness, such as described by Equation (1), does not require, nor imply, that hopping-type processes dominate the out-of-plane conductivity of PEDOT:PSS.

Diameter dependent thickness and conductivity

In order to test whether thickness dependent percolation can explain our data, we have used Equation (1) to calculate the layer thickness from the conductivity. To this end, we take the empirically fitted conductivities in Figure 2 (dashed lines) and the previously determined $\zeta = 10$ nm as input to calculate²⁴ an estimate for L , and concomitantly for the apparent via depth. The results are shown as the black lines in Figure 4b-d. Given the fact that Equation (1) is used without any adjustments, the agreement with the measured depths is surprisingly good. Although the prediction shown by the black line somewhat underestimates the measured depths, the trend of increasing depth, and therefore decreasing PEDOT:PSS layer thickness, with increasing diameter is well reproduced in Figures 4b-d. Note that also the correlation between the degree of thickness variation and the degree of conductivity variation follows naturally from the model, as shown by the black lines in panels c and d. The percolation cluster model accounts for the reduced diameter dependence for the ratio 1:2.5 and the lack of diameter dependence in the samples of PEDOT:PSS type ICP1020.

Anisotropy

For the present PEDOT:PSS system a power law relation is found between the in-plane conductivity vs. PEDOT concentration, i.e. $\sigma_0 \propto c_{\text{PEDOT}}^{3.5}$, which has been explained in the context of the regime near the percolation threshold in Chapter 4. The interpretation of the conductivity dependence on layer thickness as a result of the percolative nature of conduction in PEDOT:PSS is also in accordance with the decreasing anisotropy with decreasing PEDOT content shown in Figure 3b. That is, at lower PEDOT contents, small connected clusters have a lower probability of contributing to the in-plane conductivity, but have a similar probability of contributing to the out-of-plane conductivity due to the thinness of the film. This causes the out-of-plane conductivity to be approximately linear with PEDOT content. Since the in-plane conductivity depends on the PEDOT content as $\sigma_0 \propto c_{\text{PEDOT}}^{3.5}$ (see Chapter 4), this combines into an anticipated power-law dependence of the anisotropy $\sigma_{\parallel} / \sigma_{\perp} \propto c_{\text{PEDOT}}^{2.5}$. This result explains well the trend in the measured anisotropies as shown in Figure 3b by the solid black line.

One aspect of the anisotropies remains to be clarified, namely the fact that $\sigma_{\parallel} / \sigma_{\perp} > 1$. This seems in contradiction to the statement above that clusters that do not contribute to the in-plane conductivity can still contribute to the out-of-plane conductivity, which would result in $\sigma_{\parallel} / \sigma_{\perp} < 1$. This requires that the clusters themselves are inherently anisotropic. Such an inherent anisotropy naturally arises when the filaments in the PEDOT:PSS layer, observed in Chapter 4, are predominantly oriented in-plane, causing out-of-plane conduction paths to have a zigzag pattern. Considering that the length of the filaments of approximately 100 nm is larger than the layer thickness, it is highly likely that the filaments indeed have a preferential in-plane orientation.

Relation with molecular tunneling diodes

An interesting connection can be made with a surprising finding in the research into the tunneling conductivity of self-assembled monolayers with a top PEDOT:PSS electrode.⁵ There it was found that the resistivity of two stacked layers is the product and not the sum of the individual resistivities. Below it will be shown that this multiplicative resistivity can be explained if the out-of-plane conductivity of PEDOT:PSS does not take place homogeneously, but only through a partial area of the layer which has much higher conductivity. Such an inhomogeneity is implied by the percolation behavior observed for the

PEDOT:PSS types discussed in this article, but could also be present in layers which do not show a strong dependence of the conductivity on layer thickness.

Let the partial area for with high out-of-plane conductivity, be Ahc and the total via area be A . The out-of-plane normalized resistivity (unit Ωm^2) for the PEDOT:PSS layer per unit area, RS_{PEDOT} is now determined by the normalized resistivity per unit area of the high conductive parts, $RShc$, as $RS_{\text{PEDOT}} = RShc \times A / Ahc$. Let the SAM have a normalized resistivity per unit area RS_{SAM} . We further assume that the in-plane conductivity of the SAM is negligible and that $RShc \ll RS_{\text{SAM}}$, which both seem realistic. The normalized resistance (unit Ω) of the entire layer stack is then given by $R_{\text{TOT}} = RS_{\text{SAM}} / Ahc = (A \times RShc)^{-1} \times RS_{\text{SAM}} \times RS_{\text{PEDOT}}$, i.e. proportional to the product of the PEDOT:PSS and SAM resistivities. In other words, the resistivity of the PEDOT:PSS-SAM stack is set by the fraction of molecules in the SAM that contact a part of the PEDOT:PSS layer with high conductivity. This is the same fraction that also determines the (in the presented case, layer thickness dependent) out-of-plane resistivity of the PEDOT:PSS layer itself. Therefore, both the stack and the PEDOT:PSS resistivity are proportional to this fraction, so necessarily the stack resistivity is also proportional to the resistivity of the PEDOT:PSS layer

Conclusions

The out-of-plane conductivity of thin films of PEDOT:PSS (without high boiling solvent) for varying PEDOT contents has been systematically investigated using devices consisting of circular vias with varying diameter. This reveals a strong and significant diameter dependence of the median out-of-plane conductivity over more than three orders of magnitude. At large diameters, where this diameter dependence levels off, comparison to the in-plane conductivity shows an orders of magnitude change in anisotropy with PEDOT:PSS ratio. To investigate the trend in the anisotropy with via diameter, several models have been tested and rejected. However, this change can be well explained in the context of percolating clusters, i.e. small connected networks formed from randomly placed conductive elements in an insulating matrix. The abundance of these clusters strongly decreases with size. Hence, clusters that have only a small probability of connecting in-plane electrodes placed macroscopically far apart can still have a large probability of connecting out-of-plane electrodes that are separated by a microscopically thin film. Increasing the PEDOT:PSS ratio strongly increases the abundance of clusters

adding to the in-plane conductivity, while only marginally increasing the number of clusters adding to the out-of-plane conductivity.

The diameter dependence of the conductivity can quantitatively be explained by the concomitant change in layer thickness because of the strong size dependence of the abundance of clusters, which in order to contribute to the out-of-plane conductivity need to be as large as the layer thickness. This theoretical framework is also fully consistent with the trend found in the anisotropy by varying the PEDOT:PSS ratio. The presented strong dependence of out-of-plane conductivity on layer thickness is of evident relevance to applications which typically require a minimum value for the out-of-plane conductivity of PEDOT:PSS. Examples are the application of PEDOT:PSS in hole-extracting contacts or recombination layers in (tandem) solar cells or in the anode of OLEDs. This interpretation also rationalizes previously unexplained findings in molecular junctions where PEDOT:PSS is used as contact electrode.

Experimental

PEDOT:PSS emulsions were obtained from AGFA-Gevaert N.V. The emulsion used to prepare the samples is PEDOT:PSS ratio 1:2.5 and is commercially available as ICP-1050. PEDOT:PSS ratios 1:6, 1:12, and 1:20 were prepared using the stock dispersion of PEDOT:PSS in ratio 1:2.5. The PEDOT:PSS ratio was adapted by adding PSS. Where necessary, water was added to obtain a solid content of (0.90 ± 0.04) w%. To obtain homogeneous emulsions we sonicated the solutions. This procedure for preparing the emulsions is the same as used in Chapter 4. Additionally, as a reference sample, the commercially available PEDOT:PSS material ICP-1020, from the same manufacturer has been used. To this sample 5 vol-% dimethyl sulfoxide (DMSO) was added as a high boiling point solvent.

The out-of-plane conductivity measurements of PEDOT:PSS were performed using the previously developed technology of large-area molecular junctions. The devices were prepared according to the procedures described in Reference 25. Two types of junctions were prepared that differed only in the used photoresist; the measurement results were completely consistent. As substrates a 4" or 6" silicon wafer with a 500 nm thermally grown silicon oxide was used. On this wafer, a 1 nm layer of chromium was thermally evaporated through a shadow mask, followed by 60 nm of gold. The RMS roughness of the bottom contact is about 0.7 nm over an area of $0.25 \mu\text{m}^2$. The via in each two terminal junction was photolithographically defined in an insulating matrix of photoresist, either ma-N 1410 or L6000.5 (Micro Resist Technology GmbH) that was deposited by spin coating. After a pre-bake step to remove any remaining solvents, the layer was exposed to UV light with a Karl Süss MA1006 mask aligner, to define the vertical interconnects, 'vias', with diameters ranging from 1 to 100 μm . Unfortunately the devices with a diameter of 1 μm , were of a low quality, resulting in a too big scatter to be used in the analysis. After development, the film was hard baked at 200 °C for at least 1h. The wafer was subsequently cut in several pieces. This allowed the simultaneous processing of different PEDOT:PSS compositions on a single wafer, thereby eliminating processing variations that can affect device performance. A last step before PEDOT:PSS deposition was cleaning of the bottom gold contacts with a PDC plasma cleaner (Harrick plasma) to remove any photoresist residuals. To obtain an equal layer thickness for all PEDOT:PSS of varying ratio, the following spin coat parameters were used. The ramp-rate was 1000 RPM/s and the first spin coating step is 500 RPM for 5 s followed by 120 s of 2000 RPM (for 1:2.5), 1700

RPM (1:6), 1500 RPM (1:12), 1500 RPM (1:20) or 1500 RPM (ICP1020). On planar test substrates these parameters led to layer thicknesses around 40 nm for PEDOT:PSS ratios 1:2.5, 1:6, 1:12 and 1:20 and to a thickness of around 100 nm for the ICP 1020. After spin coating, the wafer was then immediately transferred to a vacuum oven for at least 1 h to dry the film. As top electrode, 100 nm of gold was evaporated through a shadow mask. This gold layer, apart from providing electrical contact with the measurement probes, also serves as a self-aligned mask for the removal of redundant PEDOT:PSS by reactive ion etching (O_2 plasma). This step eliminates any parasitic currents from top to bottom electrode.

For the in-plane conductivity measurements substrates were used that consisted of $3 \times 3 \text{ cm}^2$ bare sodalime glass. They were first grooved into small pieces of $1 \times 1 \text{ cm}^2$ on the back side with a diamond pen, then sonicated in a bath of acetone for 10 minutes, cleaned with soap, rinsed with deionized water for 20 min and sonicated in a bath of isopropanol for 10 minutes. Residual organic contaminations were removed using a 30 min. UV-ozone treatment (UV-Ozone Photoreactor, PR-100, Ultraviolet Products).

The PEDOT:PSS solutions were filtered using a $0.5 \mu\text{m}$ filter and deposited in air by spin coating at 1000 RPM for 1 minute, followed by 3000 RPM for 1 minute to dry the layer. This typically resulted in layer thicknesses of 60 nm, 45 nm, 40 nm and 30 nm PEDOT:PSS in ratio of 1:2.5, 1:6, 1:12 and 1:20 respectively. After spin coating, samples were transferred into a glove box (O_2 and $H_2O < 1 \text{ ppm}$) and subsequently annealed on a hot plate at $200 \text{ }^\circ\text{C}$ for a few minutes to remove residual water. Four electrodes ($1 \times 8 \text{ mm}$, 1 mm apart from each other) of 100 nm of gold were evaporated on top of each $1 \times 1 \text{ cm}^2$ piece.

After breaking the desired sample from the substrate, it was placed inside a cryostat (Oxford Instruments, modified for reaching low pressures) and evacuated to pressures below 10^{-6} mbar. The samples were exposed to air for a few minutes between the removal from the glove box and insertion into the cryostat. It was found that the room temperature conductivity only changes after exposure to air for a few hours. Once placed, samples were degassed at $200 \text{ }^\circ\text{C}$ for a few hours to reach low pressures. This annealing step in vacuum did not alter the room temperature conductivity.

The two point probe in-plane conductivity and out-of-plane conductivity measurements were performed as bias sweeps between -0.5 V and 0.5 V using a Keithley 2636a source-measure unit. To avoid the influence of water on the conductivity of PEDOT:PSS, exposure of the samples to air was minimized and electrical measurements were performed in a glove box. The conductivities reported in this article are the conductivities measured at a bias at 0.5 V. The bias dependence of the conductivity is shown in the Supplementary Information.

Appendix

Bias dependence of the conductivity

Figure A1a shows a typical G - V curve for the measured devices. To obtain a measure for the bias dependence the empirical fit: $G(V) = a \times V^2 + b$ is used, indicated in by the black line. In Figure A1b, the relation between a and b values is shown for devices of the same diameter and PEDOT:PSS composition. Clearly a is nearly proportional to b for devices of the same type, as indicated by the black line. Therefore their bias-dependence is well characterized by the measure a/b .

Figure A1c shows the average values of a/b for the varying compositions as function of diameter and Figure A1d shows the same for the reference PEDOT:PSS type ICP1020 with HBS. For all measurements the bias dependence decreases, i.e. a/b goes down, with increasing diameter and with increasing out-of-plane conductivity. This excludes that the observed decrease in out of plane conductivity with decreasing diameter (Figure 2) is caused by a top PSS-layer through which tunneling is needed for charge carriers to cross, for the following reason. Increasing, at constant bias, the thickness of such a PSS top layer decreases the electric field within this layer. This would result in a smaller bias-dependence for the devices with a thick PSS-top layer, i.e. the devices with small diameters, in contrast to what is observed in Figure A1c.

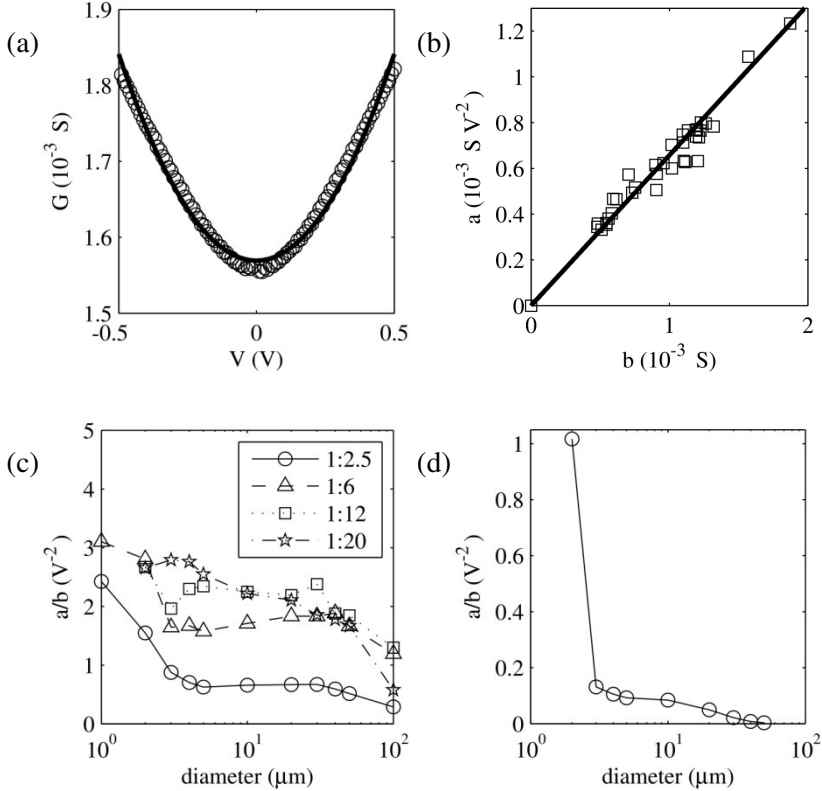


Figure A1. (a) Typical conductivity measurement as a function of applied bias for a single device. The black line shows a fit with dependence $G = aV^2 + b$. The device is produced using PEDOT:PSS in the ratio 1:2.5 and has a diameter of 10 μm . (b) Fitted a parameters vs. b parameters of all I - V curves for devices of composition PEDOT:PSS 1:2.5, with diameter 10 μm . The black line indicates a linear fit through the origin. The fit in (a) is a single data point in this figure. (c) The average bias dependence, i.e. the average ratio a/b , for different compositions and diameters. (d) The same as (c) but for the reference sample made using PEDOT:PSS type ICP1020.

The observed diameter dependence of a/b is however consistent with the percolation argument used to explain the relation between conductivity and layer thickness. Using this interpretation the number of connecting clusters per device rapidly decreases with decreasing diameter. A distribution in cluster conductivity is expected, where the conductivity is limited by the most difficult and probably furthest hop in the cluster. This distribution, together with the decreasing amount of contributing clusters for decreasing diameters, causes that devices with small diameter are dominated by hops over longer distances. Within a VRH

interpretation, along such a longer distance the same field transfers more energy to the charge carrier, resulting in a stronger bias dependence.

A generalization of the filament-conduction model

In the main text we excluded the possibility that the observed diameter dependence is caused by rare but highly conductive filaments using a simple mathematical example. The data however allows many such examples, therefore this argument is generalized in this section.

Consider the distribution of the highly conductive filaments to be a Poisson process, i.e. for each filament conductance G_{FIL} the probability of finding k such filaments is Poisson distributed, with Poisson parameter λ equal to the average number of such filaments per unit area. The mathematics of the Poisson process is such that if the stochastic number of filaments for a certain area A is k , then if A is broken into a set of disjoint subsets say A_1 and A_2 , the number of filaments in A_1 and A_2 , namely k_1 and k_2 , are independent and $k = k_1 + k_2$.²⁶

Since the conductivity of a device is proportional to the sum of the stochastic number of filaments multiplied by their conductance, it follows that the stochastic conductivity σ for a device with area A is made up as $\sigma = \sigma_1 + \sigma_2$, where the σ_1 and σ_2 are independent stochastic conductivities for the partial areas A_1 and A_2 . Therefore: $P(\sigma < S) \geq P(\sigma_1 < S)P(\sigma_2 < S)$ or if we choose N equal partial areas A_1 : $P(\sigma < S) \geq P(\sigma_1 < S)^N = P(\sigma_1 < S)^{A/A_1}$ or $P(\sigma < S)^{A/A} \geq P(\sigma_1 < S)$.

It can also be proven that for two areas A and B and any A_1 : if $A > B$ then $P(\sigma < S)^{A/A} \geq P(\sigma_1 < S)^{A_1/B}$. Therefore the probability $P(\sigma(A) < S)^{A/A}$ must be a monotonically increasing function in A . The probability $P(\sigma(A) < S)$ can be easily estimated by the relative number of devices with area A that have a conductivity less than S . The resulting estimates of $P(\sigma(A) < S)^{A/A}$ for the combined set of devices with PEDOT:PSS ratio 1:6, 1:12 and 1:20 are shown in Figure A2.

In Figure A2 the example given in the main text can be found at $S = 5 \cdot 10^{-4}$ S/m. Devices with a diameter of $4 \mu\text{m}$ have a value for $P(\sigma(A) < S)^{A/A}$ that is smaller than the value of $P(\sigma(A) < S)^{A/A}$ for devices with a diameter of $2 \mu\text{m}$ in contradiction to the previous statement that $P(\sigma(A) < S)^{A/A}$ has to be monotonically increasing with A . Many more such examples can be found, such as

for $5 \cdot 10^{-4} \text{ S/m} < S < 5 \cdot 10^{-2} \text{ S/m}$ devices with a diameter of $5 \mu\text{m}$ have a value of $P(\sigma(A) < S)^{A_1/A}$ that is smaller than the value of $P(\sigma(A) < S)^{A_1/A}$ for devices with a diameter of $2 \mu\text{m}$. There is an abundance of cases in which $P(\sigma(A) < S)^{A_1/A}$ is decreasing instead of monotonically increasing. In other words, the lines in Figure A2 should be ordered in the same way as the legend on the right and they should not cross, but this is not true for many of the lines in Figure A2. Therefore, it is highly unlikely that the diameter dependence of the median conductivity can be explained by rare but highly conductive filaments.

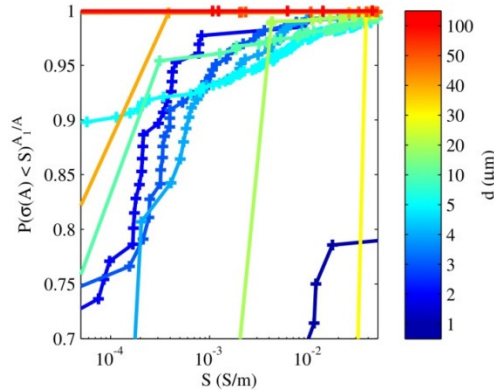


Figure A2. Estimated values of $P(\sigma(A) < S)^{A_1/A}$, which should monotonically increase with area A , for the combined set of devices with PEDOT:PSS ratios of 1:6, 1:12 and 1:20 and $A_1 = 1/4 \pi \mu\text{m}^2$.

Realizations of the connected layers model

Here the results are shown for a ‘leaky lasagna’, i.e. layered model in which layers are connected by a few highly conductive shorts, resulting in a diameter dependent average conductivity. As discussed in the main text, this model adequately describes the conductivity as a function of diameter, but demands filament conductivities much higher than expected for PEDOT:PSS filaments.

For the model, a vertical filament density of 1 (Figure A3c) or 10 (Figure A3a and A3b) per $1/4 \pi \mu\text{m}^2$ is used. The conductivity for each filament is stochastic, with the distribution described by the probabilities and matching conductivities in Table

A1. Figures A3a and b show the results for a 10 layer system, where the in-plane conductivity is approximated to be much higher than the filament conductivity.

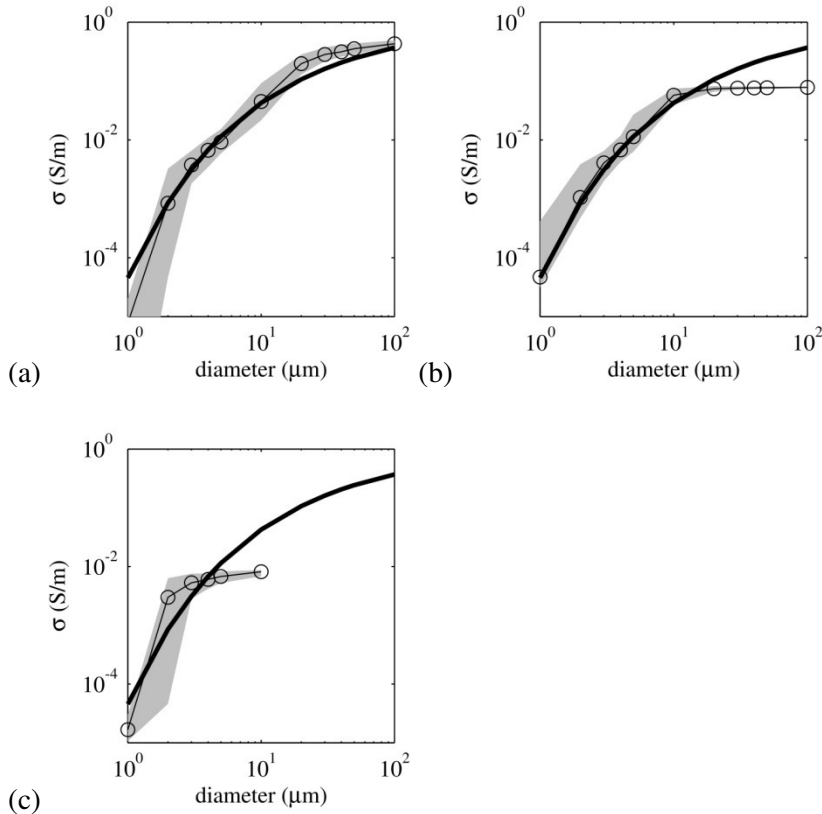


Figure A3. (a,b) 10-layer models with highly conductive planes, which allow for (a) unlimited filament conductance, (b) filament conductance limited to $10 G_0$. (c) A 5-layer model with in-plane bond percolation, bond conductivity $10 G_0$, bond probability $p = 0.5$, in which out of plane filaments are allowed with conductance up to $100 G_0$. Parameters used are given in Table 1.

Figure A3a, for which filaments exceeding $1000 G_0$ have been allowed, matches well with the empirical fit for PEDOT:PSS ratios 1:6, 1:12 and 1:20 shown in Figure 2a of the main text. The values in Table A1 were chosen *ad hoc* and therefore there is still room for improvement within the model.

Figure A3b shows the same model as shown in Figure A3a, but restricted to a maximum filament conductance of $10 G_0$. Although there is a good match between the model and the empirical fit for devices with diameters below $10 \mu\text{m}$, the lack of an overall match clearly shows the inadequacy of this model.

Alternatively, if instead of vertical filaments, shorts of much higher conductance ($100 G_0$) are considered between adjacent layers, then the in-plane conductivity must play a role. For this purpose the in-plane conductivity in each of the layers was described by an $N \times N$ bond percolation model with bond conductance $10 G_0$ and bond probability $p = 0.5$ to account for the critical percolation behavior found in-plane in Chapter 4. The number of sites was chosen as $N = d / (1 \mu\text{m})$ and the distribution for the conductance of the vertical connections is shown in Table A1. The result for a 5 layer system with these parameters is shown in Figure A3c. Although parameters were varied to near optimal values, no good match between the model and the empirical fit could be obtained for diameters larger than $5 \mu\text{m}$, due the limits on the out of plane conductivity that are imposed by the in-plane conductivity.

Table A1: Distribution used for the conductance of filaments used for the models shown in for Figure A3.

Figure A3a			Figure A3b			Figure A3c	
G(S)	P		G(S)	P		G(S)	P
0.00E+00	7.04E-01		1.96E-10	8.41E-01		9.82E-11	8.98E-01
3.81E-10	2.00E-01		3.46E-08	1.11E-01		2.26E-08	8.51E-02
6.72E-08	5.00E-02		1.39E-06	4.20E-02		7.75E-02	1.65E-02
6.81E-07	2.22E-02		1.64E-04	4.79E-03			
2.57E-06	1.25E-02		7.75E-04	8.82E-04			
6.25E-06	8.00E-03						
2.26E-04	2.00E-03						
2.58E-03	5.00E-04						
5.85E-03	2.22E-04						
9.41E-03	1.25E-04						
1.31E-02	8.00E-05						
1.91E-01	2.00E-05						

References

- ¹ Y. H. Kim, C. Sachse, M. L. Machala, C. May, L. Müller-Meskamp, K. Leo, *Adv. Funct. Mater.* **2011**, *21*, 1076.
- ² Y. Xia, K. Sun, J. Ouyang, *Adv. Mater.* **2012**, *24*, 2436.
- ³ A. M. Nardes, M. Kemerink, R. A. J. Janssen, *Phys. Rev. B* **2007**, *76*, 085208.
- ⁴ A. M. Nardes, M. Kemerink, R. A. J. Janssen, J. A. M. Bastiaansen, N. M. M. Kiggen, B. M. W. Langeveld, A. J. J. M. van Breemen, M. M. de Kok, *Adv. Mater.* **2007**, *19*, 1196.
- ⁵ P. A. van Hal, E. C. P. Smits, T. C. T. Geuns, H. B. Akkerman, B. C. D. Brito, S. Perissinotto, G. Lanzani, A. J. Kronemeijer, V. Geskin, J. Cornil, P. W. M. Blom, B. D. Boer, D. M. de Leeuw, *Nat. Nanotech.* **2008**, *3*, 749.
- ⁶ J.-S. Yeo, J.-M. Yun, D.-Y. Kim, S. Park, S.-S. Kim, M.-H. Yoon, T.-W. Kim, S.-I. Na, *ACS Appl. Mater. Interfaces* **2012**, *4*, 2551.
- ⁷ S.-I. Na, G. Wang, S.-S. Kim, T.-W. Kim, S.-H. Oh, B.-K. Yu, T. Lee, D.-Y. Kim, *J. Mater. Chem.* **2009**, *19*, 9045.
- ⁸ Given the small layer thickness for spin-coated layers, i.e. ~ 100 nm, even a modest out-of-plane conductivity, e.g. 1 S/m, can result in devices with very low resistance, i.e. 0.1 Ω for a 1 mm x 1 mm device. Since contact resistances are typically of the order 1-10 Ω , micrometer sized devices are required.
- ⁹ *I-V* curves are decided to be atypical on basis of the criterion that 90% of all conductivities measured at biases larger than 0.1V fall between 30% and 100% of the conductivity measured at the maximum bias, i.e. 0.5 V. This criterion discards less than 20% of all devices. For an example of an *I-V* curve, see the Appendix. It for instance allows for Ohmic *I-V* curves, but the criterion is effective at removing *I-V* curves which have transient changes, i.e. big changes in conductivity during the measurement.
- ¹⁰ J. Hwang, F. Amy, A. Kahn, *Org. Electron.* **2006**, *7*, 387.
- ¹¹ Y. Xia, J. Ouyang, *J. Mater. Chem.* **2011**, *21*, 4927.
- ¹² X. Crispin, F. L. E. Jakobsson, A. Crispin, P. C. M. Grim, P. Andersson, A. Volodin, C. van Haesendonck, M. Van der Auweraer, W. R. Salaneck, M. Berggren, *Chem. Mater.* **2006**, *18*, 4354.
- ¹³ T. Wang, Y. Qi, J. Xu, X. Hu, P. Chen, *Appl. Surf. Sci.* **2005**, *250*, 188.
- ¹⁴ C. S. Suchand Sangeeth, M. Jaiswal, R. Menon, *J. Phys. Condens. Matter* **2009**, *21*, 072101.
- ¹⁵ T. Wang, Y. Qi, J. Xu, X. Hu, P. Chen, *Appl. Surf. Sci.* **2005**, *250*, 188.
- ¹⁶ A. V. Tartakovskii, M. V. Fistul', M. E. Raikh, and I. M. Ruzin, *Sov. Phys. Semicond.* **1987**, *21*, 603.
- ¹⁷ A near-literal copy of Reference 16 is available online as Y. Park, *Solid State Commun.* **2000**, *115*, 281.
- ¹⁸ A. S. Rodin, M. M. Fogler, *Phys. Rev. Lett.* **2010**, *105*, 106801.
- ¹⁹ J. Ouyang, Q. Xu, C.-W. Chu, Y. Yang, G. Li, J. Shinar, *Polymer* **2004**, *45*, 8443.
- ²⁰ S. Samitsu, T. Shimomura, K. Ito, M. Fujimori, S. Heike, T. Hashizume, *Appl. Phys. Lett.* **2005**, *86*, 233103.
- ²¹ Y. P. Mamunya, *J. Macromol. Sci., B* **1999**, *38*, 615.
- ²² B. I. Shklovskii and A.L. Efros, *Electronic Properties of Doped Semiconductors*, Springer Verlag, Heidelberg: 1984, ISBN 3-540-12995-2

²³ M. Pollak, J. J. Hauser, *Phys. Rev. Lett.* **1973**, *31*, 1304.

²⁴ Additionally the following estimates have been made: the layer thickness for a diameter of 100 μm is 40 nm, i.e. the layer thickness on glass substrates using the same spin coating conditions, and the layer thickness of the photo resist layer is 520 nm.

²⁵ I. Katsouras, V. Geskin, A. J. Kronemeijer, P. W. M. Blom, D. M. de Leeuw, *Org. Electron.* **2011**, *12*, 857.

²⁶ J. A. Rice, *Mathematical Statistics And Data Analysis*; Cengage Learning, 2007. Poisson processes are discussed on page 46.

Chapter 6:

A systematic study to universal scaling of the out-of-plane conductivity of thin films of PEDOT:PSS

Abstract

For the development of organic electronic materials it is important to relate the charge transport behavior to their microscopic structure. Recent measurements of the out-of-plane conductivity of poly(3,4-ethylenedioxythiophene):poly(styrene sulfonate) (PEDOT:PSS), and of the conductivity of a semiconducting polymer in a field effect device revealed a curious power law dependence of the conductivity on field and temperature in both the Ohmic and non-Ohmic regimes. This was referred to as universal scaling. Connecting this behavior to a particular microscopic model has proven to be difficult. Here we present a systematic study of the temperature and bias voltage dependence of the out-of-plane conductivity of PEDOT:PSS through the use of interconnect structures (vias) for varying via diameters and various PEDOT:PSS formulations. The measurements indeed show universal scaling. By use of explicit knowledge of the microscopic structure of the used PEDOT:PSS materials the number of possible underlying models can be narrowed down to only three models: a model for finite size effects in quasi one-dimensional variable range hopping, a model for a chain of quantum dots in the Coulomb blockade regime and a model for connected Luttinger liquids. The presented measurements seem at odds with all but the latter model.

Introduction

In organic electronics, the charge transport behavior is typically strongly affected by the positional and energetic disorder in the material. This disorder can cause local bottlenecks for the current which determine the macroscopic conductivity of the material. Therefore, a good description of the bottleneck is needed for a good description of the charge transport of a disordered system. Some of the properties of the disorder of a molecular electronic material can be determined from microscopic techniques, such as scanning probe microscopy. However, it is nearly impossible to determine the position of the current paths in a molecular system and the conductivity along these paths. In other words, experimental techniques are in general not able to determine the specific bottlenecks for charge conduction in molecular systems. To overcome this problem, charge transport properties have been measured and compared to theoretical models and simulations, typically inspired by some knowledge of the microscopic structure of the particular molecular system. The simplest model which is able to accurately describe the experimental charge transport properties for a molecular system is most likely correct; this principle is commonly referred to as Ockham's razor. In investigations of conducting polymers, charge transport studies often reveal a stretched exponential temperature dependence of the Ohmic conductivity ($\sigma \propto \exp[-(T_0/T)^\alpha]$), which is accurately described by variable range hopping (VRH).^{1,2} Some conducting polymer systems with higher conductivity tend to show a power law temperature dependence of the Ohmic conductivity ($\sigma \propto T^\alpha$), which is typically considered to be a consequence of the increasingly metallic properties of the system, which cause an insulator to metal transition.^{3,4,5}

Recent studies on organic electronic systems, which do not only measure the Ohmic conductivity, but also the non-Ohmic conductivity obtained at increased electric fields, reveal a curious pattern.^{6,7,8,9,10,11} They show that the Ohmic conductivity has a power law temperature dependence, but most importantly, that rescaling the current and voltage using the power law dependence on temperature produces a universal curve. Both the Ohmic and non-Ohmic parts of the temperature-scaled I - V curves match this universal curve, which consists of a crossover between an Ohmic voltage dependence, i.e. $I(V) \propto V$, and a steeper power law dependence, i.e. $I(V) \propto V^\beta$. In most experimental investigations^{8,9,11} these observations are explained as stemming from Luttinger liquid (LL) behavior.¹² However, due to very similar resulting charge transport behavior, a

strong case can also be made for a description based on a chain of quantum dots with Coulomb blockade behavior,^{13,14} which is used as explanation in Reference 7. Recently Rodin and Fogler¹⁵ have suggested that previous experimental results might also be well explained in terms of quasi one-dimensional (1D) VRH, which is in line with the widespread use of VRH for the description of charge transport in molecular systems. The near exact match of charge transport behavior for these fundamentally different interpretations poses a challenge to experimentally differentiate between them.

Here we study poly(3,4-ethylenedioxythiophene):poly(styrene sulfonate) (PEDOT:PSS), an organic conducting polymer system with widespread applications in organic electronics. In Reference 6 it was shown that the out-of-plane conductivity of spin coated layers of PEDOT:PSS shows universal scaling. Unfortunately the data presented in Reference 6 did not allow for the origin of the universal scaling being unambiguously determined. To further address this problem we study the out-of-plane conductivity of spin coated layers of a PEDOT:PSS type which has been extensively studied in Chapters 4 and 5. The previous investigations reveal that the in-plane conductance of this type of PEDOT:PSS takes place via a percolating network of quasi-1D filaments, as was deduced from the temperature, field and composition dependence of the conductivity in combination with transmission electron microscopy (TEM), discussed in Chapter 4. Furthermore, studies into the out-of-plane conductivity of the same materials show a strong thickness dependence, which can be explained on basis of percolation theory. The out-of-plane conduction mechanism of these materials is still unknown. Since the conduction pathways that dominate the out-of-plane conductivity are different from those that dominate the in-plane conductivity, the dominant transport mechanism may well be different for the in- and out-of-plane directions.

We present a study of the out-of-plane conductivity of spin coated PEDOT:PSS layers using devices which consist of circular interconnects (vias) in an insulating photoresist layer sandwiched between two metallic electrodes. The same structures were used in Chapter 5 to study the room temperature Ohmic conductivity. A careful study of the determined scaling parameters of the universal behavior observed in these devices, combined with previous knowledge of the PEDOT:PSS materials is used to evaluate the applicability of various interpretations and to provide criteria for the development of possible alternatives which explain the observed universal behavior.

Results

Figure 1a shows the measured conductivity as a function of voltage at different temperatures for a 5 μm device with PEDOT:PSS ratio 1:6. At low voltages, the conductivity is Ohmic, i.e. independent of the voltage, while at higher voltages the conductivity shows a power law dependence on voltage, which shows up as a linear dependence in the log-log plot. The Ohmic conductivity, determined at low voltages, is shown as a function of temperature in Figure 1b for the non-HBS-treated PEDOT:PSS in the ratios of 1:2.5, 1:6, 1:12, and 1:20 studied before in Chapters 4 and 5 as well as for the additional, HBS-treated PEDOT type ‘ICP1020’ for devices with varying via-diameter. In each case the Ohmic conductivity is well described by a power law relation, i.e. $\sigma_{OHM} \propto T^\alpha$. Such temperature dependence has been observed before for the Ohmic conductivity of PEDOT:PSS^{4,16} and PEDOT doped with other molecules.¹⁷ There the power law dependence is typically explained as related to the critical regime between metal and insulator.¹⁸

In Reference 10, the same power law is found for the Ohmic conductivity measured in the out-of-plane direction of spin coated layers of PEDOT:PSS, where additionally the electric field is increased to study the non-Ohmic regime. With the proper normalization of the J - V curves, it was shown that all data points collapse onto a universal curve. In Figure 1c the same procedure is applied to the device with PEDOT:PSS ratio 1:6 for which the full dataset is shown in Figure 1a. Indeed, the measured J - V curves at different temperatures produce a similar universal curve as measured in Reference 10, signified by the two following parts. In the Ohmic part, shown in the left part of Figure 1c, the data is best described by the leftmost black dashed line representing the relation $J/T^{\alpha+1} \propto eV/kT$, where J is the current density, T denotes the temperature, α is the parameter derived from the fits shown in Figure 1b, e denotes the electron charge, and k the Boltzmann constant. In the non-Ohmic part, shown in the right part of Figure 1c the data can be described by the steep black dashed line representing the relation $J/T^{\alpha+1} \propto (eV/kT)^\beta$. In many publications^{13,10, 19} the universal curve is restricted to $\beta \equiv \alpha + 1$. This rule is also applied here, since it results in an accurate description of the data, while reducing the number of fit parameters. The observed behavior is captured in the following equation:

$$J = cT^{1+\alpha} \sinh\left(\gamma \frac{eV}{kT}\right) \left| \Gamma\left(\frac{1+\beta}{2} + \frac{i}{\pi} \gamma \frac{eV}{kT}\right) \right|^2, \quad (1)$$

where c is a scaling parameter and γ a parameter such that the crossover between the Ohmic and non-Ohmic regime takes place at $eV/kT \approx 2\gamma^{-1}$,²⁰ and Γ the gamma function.

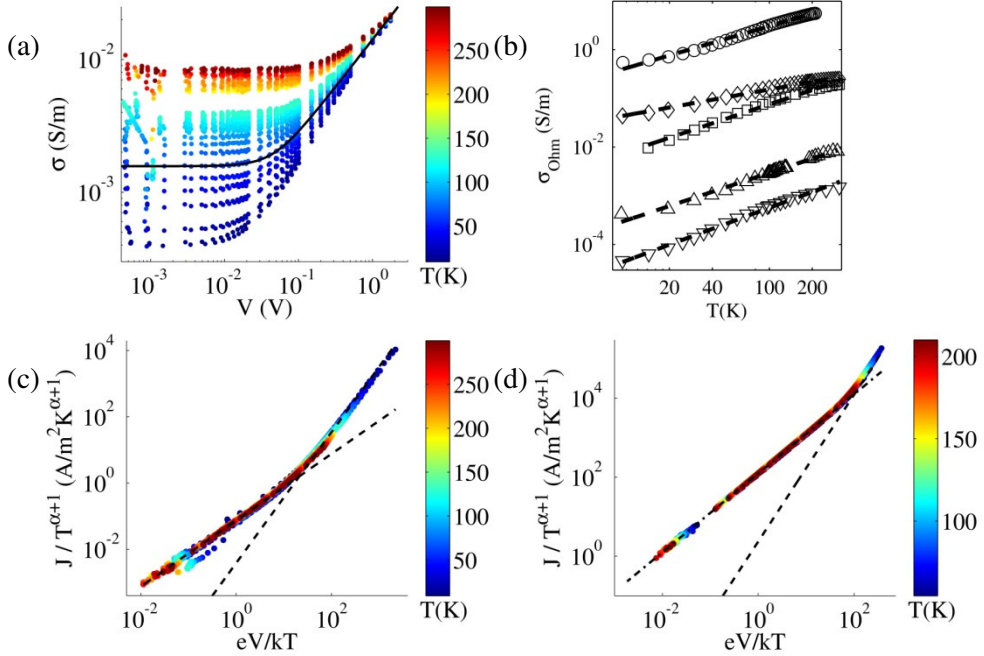


Figure 1. (a) Full dataset for a 5 μm device with PEDOT:PSS ratio 1:6. The black line indicates a fit of Equation (1) to the data measured at 60 K. (b) The Ohmic conductivity as a function of temperature for devices with PEDOT:PSS ratios 1:2.5(\square), 1:6(\diamond), 1:12 (\triangle),1:20 (∇) and type ‘ICP1020’ (\circ) and diameter 20 μm (\square), 100 μm (\diamond), 5 μm (\triangle), 5 μm (∇) and 10 μm (\circ). The device labeled by \diamond is the same device as in (a). The dashed lines indicate power law fits. (c) J - V curves normalized using the temperature dependence found in a) for the same 5 μm device with PEDOT:PSS ratio 1:6 as shown in (a). The leftmost black dashed line indicates an Ohmic dependence, the steeper black dashed line indicates a power law $I(V)$ behavior.

To compare the behavior of all the studied devices, the scaling parameters of the universal curve were determined as follows. From a power-law fit to the Ohmic conductivity as a function of temperature, as shown in Figure 1b, the parameter α is determined. The remaining parameters, γ and c , are determined by fitting Equation (1) to the normalized dataset, as shown in Figure 1c. The resulting power law exponents α are plotted in Figure 2a and show a remarkable dependence on via-diameter for all measured devices except those of PEDOT:PSS with ratio 1:2.5. This dependence can be described by the empirical relation $\alpha(d) \propto \log[(d_0 / d)^{1/5}]$ with $d_0 = 700 \mu\text{m}$, as indicated by the thick black dashed line. Figure 2b shows the

γ^{-1} parameters for the different measured devices, as determined by the fitting procedure. The different PEDOT:PSS ratios, produced from the same starting emulsion are grouped together at $\gamma^{-1} = 10-20$, while the HBS-treated PEDOT:PSS type ‘ICP1020’ appears at $\gamma^{-1} = 60$. For the ‘ICP1020’ there is also a difference between the measurements with continuous voltages (up to 0.5 V) and with pulsed voltages (up to 2.5 V). This could be an effect of the fitting procedure; because the extended pulsed voltage range yields a larger number of non-Ohmic data points for the high temperature measurements, these obtain an increased weight, leading to somewhat different values for γ^{-1} . The other two parameters, i.e. α and c appear unaffected by this.

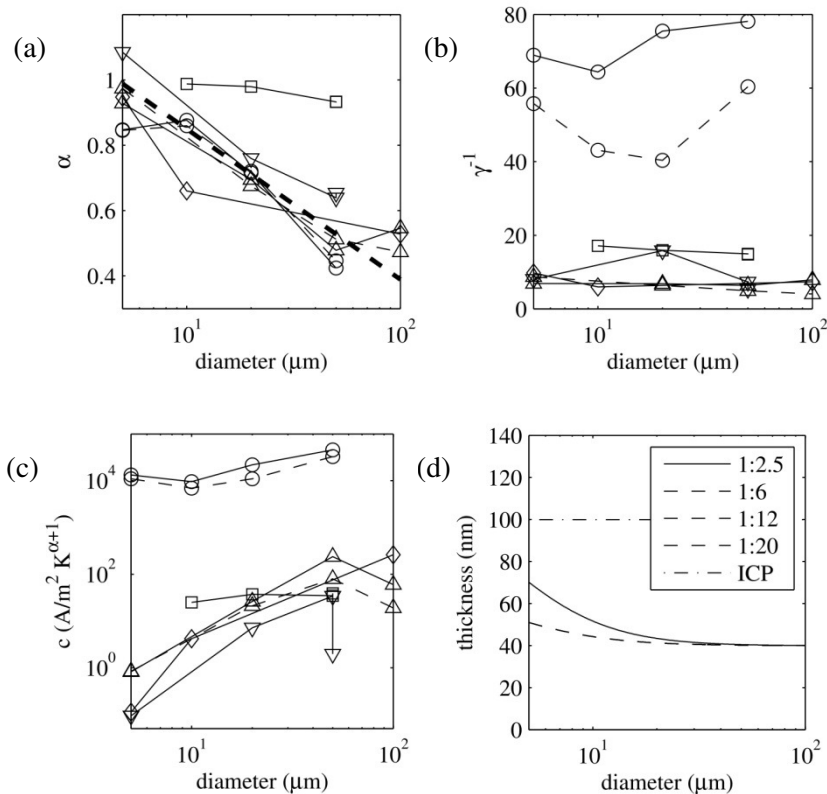


Figure 2. Scaling parameters of the universal curve, (a) α , (b) γ^{-1} and (c) c , for devices with varying diameter and for device and PEDOT:PSS ratios 1:2.5(\square), 1:6(\diamond), 1:12 (\triangle), 1:20 (∇), and PEDOT:PSS type ‘ICP1020’ (\circ). For PEDOT:PSS ratio 1:12 and PEDOT:PSS type ‘ICP1020’, additional measurements with an extended voltage range, i.e. up to 2.5 V instead of 0.5 V, have been performed and are indicated by the dashed connectors. The thick black dashed line in a) indicates the empirical relation described in the text. (d) Empirical relations for the layer thickness of the different devices obtained from AFM images in Chapter 5.

Figure 2c shows the c parameters for the different measured devices. The unit for this parameter is a bit awkward. However, since α , γ , and c are the full set of parameters, having fixed α and γ , c is uniquely defined by the room temperature conductivity. Unfortunately there is no naturally associated temperature with the devices to turn the c parameters into current densities. Still the diameter and composition dependence shown in Figure 2c are very similar to those of the room temperature conductivity for such devices. The room temperature conductivity of the same devices as studied here is discussed in Chapter 5, where the change in conductivity with diameter is found to be related to systematic variations in the layer thickness between devices, as shown in Figure 2d. Therefore the x -axis of panel c, but possibly also that of panels a and b, should actually be read as ‘layer thickness’.

The collapse to a universal curve, as shown in Figure 1b, describes the data quite well, and reduces the entire measurement set for all temperatures to just three parameters, i.e. α , γ , and c . To study the data in more detail, Equation (1) has been applied to single J - V curves, i.e. at a single temperature. An example of this is shown in Figure 1a, where a fit with Equation (1) to all data measured at 60 K is shown by the black line. In this way the following parameters can be defined as a function of temperature: β (notice that α cannot be defined for data at a single temperature), γ , and c . These temperature dependent parameters are shown in Figure 3. Although according to Equation (1) these should be constant, they do show some temperature dependence. Most remarkably, for $\beta(T)$ a decrease with temperature is observed. Such a decrease has been noted before in Reference 11, where it was shown that polymer nanowires display a similar decrease of $\beta(T)$ with temperature. For the measurements presented in Reference 11, this could be accurately described by $\beta(T) = 1 + \beta_0 T^\nu$, where β_0 and $\nu = 0.2-0.5$ are fit parameters. This relation also gives a good description for the measurements shown in Figure 3a. The same relation works well for all devices with non-HBS-treated PEDOT:PSS in the ratios 1:2.5, 1:6, 1:12, and 1:20. The temperature dependence of the fit parameters to the universal curve for devices with PEDOT:PSS type ‘ICP1020’ are discussed below. The remaining γ^{-1} and c parameters shown in Figures 3b and 3c are highly constant, except for an upturn toward low temperatures. This upturn can be explained by measurement errors due to the low values of the voltages, currents and temperatures for the crossover point which determines these parameters. In summary, in spite of the good description of the dataset for devices given by the fixed parameters α ($\beta \equiv \alpha + 1$), γ , and c , a

temperature dependent $\beta(T)$ provides extra information which can be used to test different models.

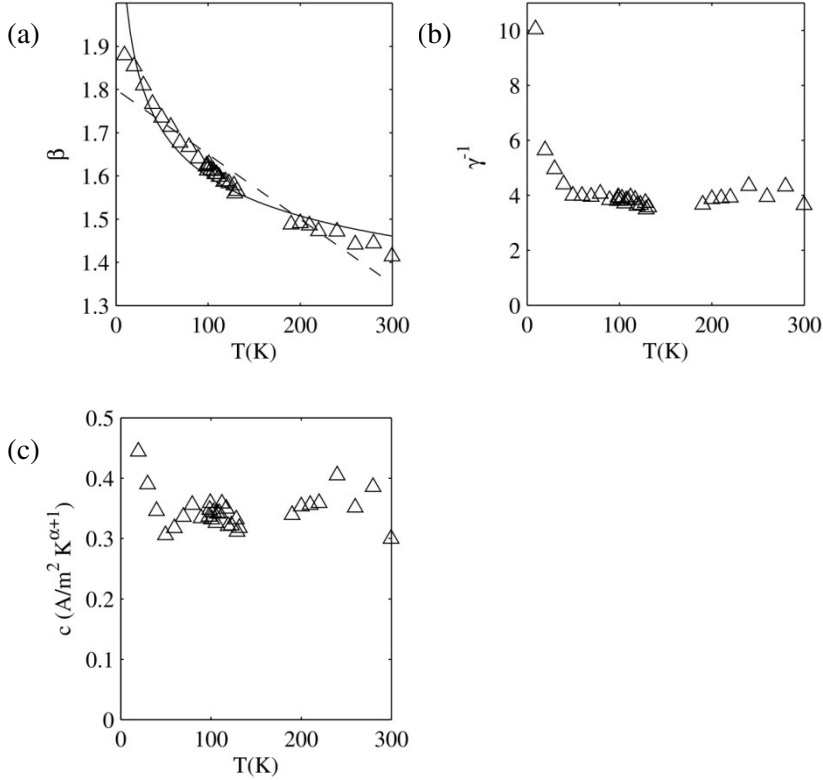


Figure 3. Scaling parameters of the universal curve determined for each temperature, (a) $\beta(T)$, (b) $\gamma^{-1}(T)$ and (c) $c(T)$, for a device with diameter 5 μm and PEDOT:PSS 1:12. The solid line in (a) is a fit of the form $\beta(T) = 1 + \beta_0 T^{-\nu}$, with $\beta_0 = 1.8 \text{ K}^\nu$ and $\nu = 0.24$. The dashed line in (a) is a linear fit.

Figure 4a shows the temperature dependence of β for a device with diameter 10 μm and PEDOT:PSS type ‘ICP1020’. A best fit to the relation from Reference 11, shown as the continuous line in Figure 4a, still results in $0.2 \leq \nu \leq 0.5$, but the fit does not reproduce the correct functional dependence. The empirical linear fit indicated by the dashed line gives a much better representation, as opposed to the data shown in Figure 3a, where the linear fit does not give a good description of $\beta(T)$. The parameters γ^{-1} and c shown in Figures 4b and 4c also have a significant downward trend. These trends do not affect the power law dependence of the Ohmic conductivity since the trends in γ^{-1} and c cancel for the power law dependence via $\sigma_{\text{Ohm}}(T)/T^\alpha \propto \gamma c$. The influence of the trends in γ^{-1} and c on the

collapse for this device, shown in Figure 1d, appears to show up as a small broadening around the crossover point, but overall a good match to Equation (1) is still obtained.

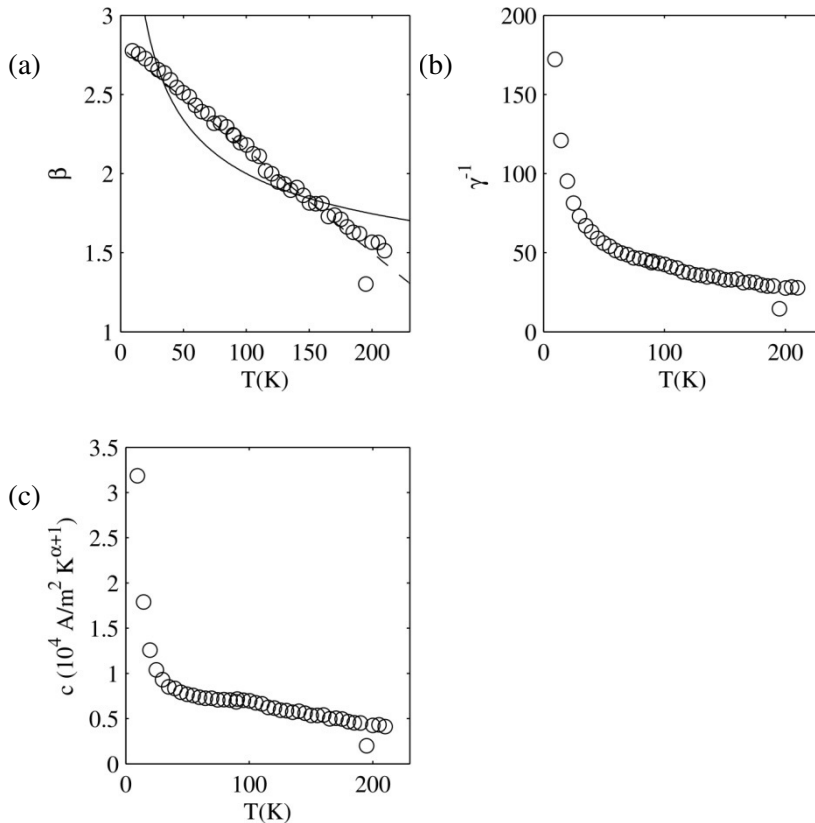


Figure 4. Scaling parameters of the universal curve determined for each temperature, (a) $\beta(T)$, (b) $\gamma^{-1}(T)$ and (c) $c(T)$, for a device with diameter $10 \mu\text{m}$ and PEDOT:PSS type ‘ICP1020’. The solid line in (a) is a fit of the form $\beta(T) = 1 + \beta_0 T^\nu$, with $\beta_0 = 7 \text{ K}^\nu$ and $\nu = 0.42$. The dashed line in (a) is a linear fit.

Discussion

The interpretational schemes that are considered below for describing the charge transport behavior presented above are selected on basis earlier studies to this particular type of PEDOT:PSS, see Chapters 4 and 5. These studies have shown that the temperature and field-dependence of the in-plane conductivity are best described by quasi-1D VRH, indicating conduction mediated by narrow filaments. The change in conductivity with PEDOT concentration shows power law behavior,

interpreted as being due to a percolating network of filaments. TEM data confirm the existence of such filaments both in solution (cryo-TEM) and in dried films and furthermore show that the filaments have lengths of $\gtrsim 200$ nm and widths of 4-5 nm. The room temperature conductivity for the out-of-plane circular via devices depends strongly on the layer thickness. Furthermore, the layer thickness is found to be different for devices of different diameter, i.e. the smaller diameter devices have thicker PEDOT:PSS layers. The strong dependence of the room temperature conductivity on layer thickness was interpreted in terms of a strongly increasing number of percolating clusters connecting the top to the bottom electrode for thinner layers.

The microstructure of the used PEDOT:PSS as summarized above implies that the model used to describe the presented data must fit with the observed charge transport through one-dimensional filaments. To our knowledge three such models exist, namely a model based on quasi-1D VRH,¹⁵ a model based on Coulomb blockade behavior in chains of quantum dots,¹³ and the Luttinger liquid (LL) model describing free, interacting electrons confined to 1D.^{8,9,12,11,19,21,22,23,24}

First, the quasi-1D VRH model by Rodin and Fogler¹⁵ will be tested against the presented data since this interpretation is the most natural extension of the work in Chapter 4 on the presented PEDOT:PSS in ratio 1:2.5, 1:6, 1:12, and 1:20. In this model, the power law behavior in the temperature dependence of the Ohmic conductivity stems from a crossover from a low temperature regime where the conductivity is determined by a large ensemble of parallel short 1-D channels to a high temperature regime where a similar ensemble with long 1-D channels determines the behavior. This crossover is caused by the typical length scale for VRH, namely the length of the critical hop, which is temperature dependent and decreases with increasing temperature. Therefore the same ensemble of 1D channels is best modeled as short at low temperatures, and as long at high temperatures. The ensemble of short channels has the property that its conductivity is dominated by a few channels with a few localized states that are aligned in both energy and space, causing high conductivity. This results in an Ohmic conductivity of which the slope of $\log(\sigma_{\text{OHM}})$ as a function of $\log(T)$ increases with temperature. The Ohmic conductivity in the high temperature VRH regime has the opposite curvature, since it is described by the typical stretched exponential temperature dependence. The crossover is therefore characterized by an inflection point in $\log(\sigma_{\text{OHM}})$ as a function of $\log(T)$, best described by a power law. A similar inflection point is found for $\log(I)$ as a function of $\log(V)$, by extending the VRH

behavior to the inflection point in the Ohmic conductivity. Numerically this was shown to result in behavior well described by Equation (1).¹⁵

The model by Rodin and Fogler¹⁵ shows that $\beta \approx \alpha + 1$, in agreement with the data presented here, and that $\gamma^{-1} \approx N^2$, where N is the number of hops needed to cross the layer at the inflection point in the temperature dependent conductivity. For the PEDOT:PSS ratios 1:2.5, 1:6, 1:12, and 1:20 this results in $N \approx 3-4$ and for PEDOT:PSS type 'ICP1020' in $N \approx 6-9$, which seems reasonable. Furthermore the model predicts $\beta(T) = 1 + \beta_0 T^\nu$ with $\nu = 0.5$, which resembles the measurements for PEDOT:PSS ratios 1:2.5, 1:6, 1:12, and 1:20. However, the model predicts $\alpha = N - 1 - 2/N$, which –given the demand that N is integer– requires $\alpha \geq 4/3$. For our data this invalidates this model. Given the close resemblance of the model to the data, there is a possibility that combining quasi 1-D VRH with another low temperature theory may yield a description which is consistent with the data.

Second, convincing evidence has been published that single nanowires^{21,25} and ensembles of nanowires¹³ can be modeled as chains of quantum dots in the Coulomb blockade regime. Due to the capacitance of an object with respect to its surroundings energy is required to charge an object. Since charge carriers are quantized, there exists a minimum charging energy required for moving a charge carrier onto a quantum dot, which can easily be of the order of few meV for a typical (segment of a) nanowire. The availability of thermal energy to overcome such a barrier causes the temperature dependence in the conductivity of such a system, while the shift of the charging levels with bias voltage causes the voltage dependence of the system. An analysis of these effects for a description of conduction through carbon nanotubes and nanowires as a chain of quantum dots presented in Reference 13 resulted in charge transport described by Equation (1). TEM results, shown in Chapter 4, for PEDOT:PSS with ratios 1:2.5 and 1:20 show filaments of similar diameters as the carbon nanotubes and nanowires in Reference 13. It is therefore likely that barriers for the conductivity along the PEDOT:PSS filaments cause quantum dots with similar charging energies as presented in Reference 13, resulting in similar charge transport behavior.

The model in Reference 13 results in $\beta = \alpha + 1$ as is the case for the presented measurements. Furthermore in the model, α is a measure for the disorder in the system causing a strong decrease in conductivity with increasing α , which is shown to be in agreement with the data presented for nanowires and carbon nanotubes with $0 < \alpha < 2.4$. Figures 2a and 2c show that a similar relation exists for the

devices with PEDOT:PSS ratios 1:6, 1:12, and 1:20, which have $0.4 < \alpha < 1.1$. Counter-intuitively the model does not predict a change in γ^{-1} for an increasing number of quantum dots, as opposed to an increase in γ^{-1} which could be expected if the voltage is divided over more and more barriers between the quantum dots. Instead the model predicts $\gamma^{-1} \approx 0.5$ in agreement with the data presented in Reference 13, but in disagreement with the values of $\gamma^{-1} = 3-80$ for the data presented here.²⁶ Therefore it is concluded that the presented measurements cannot be described as resulting from a chain of quantum dots in the Coulomb blockade regime.

Third, the observed transport behavior could be a consequence of LL behavior, as suggested in References 8, 9, and 11. The LL-model describes interacting electrons confined to one dimension, which can be argued to be the case in the PEDOT:PSS with ratios 1:2.5, 1:6, 1:12, and 1:20 for which the in-plane conductivity takes place via filaments with diameters of 4-5 nm, as discussed in Chapter 4. The LL-model was first proposed by Luttinger²⁷ to be an exactly solvable model for interacting fermions. Haldane²² later conjectured that this is the 1D analogue to the higher dimensional Landau Fermi liquid theory, generalizing the theory to a large range of one-dimensional systems. Kane *et al.* calculated the conductivity through a LL system with a single weak link which is connected on either side to a normal metal and found a result similar to Equation (1) with $\alpha = \beta + 1$ and $\gamma^{-1} = 1$.²³

In Reference 19, the conductivity through a bundle of single wall carbon nanotubes is determined to be described by Equation (1) with $\alpha = \beta + 1$, where $\alpha \approx 0.3$ for tunneling into the bulk of the nanotube and $\alpha \approx 0.6$ for tunneling into the end of the nanotube, close to theoretical estimates. The resulting $\gamma^{-1} \approx 4$ is explained by describing the connections into and out of the bundle as two tunnel junctions in series. In Reference 24 the conduction through molybdenum selenide nanowires is measured, yielding values for α and β in two groups: $\alpha \approx \beta$, interpreted as caused by a high resistive junction between a Fermi Liquid (FL) and a LL, and $\alpha \approx 2\beta$, interpreted as caused by a crossover with temperature between the conductivity being dominated by a FL-to-LL junction to being dominated by a LL-LL junction. The values of α are in the range 0.6 – 7 and for the LL-LL junctions are shown to decrease with increasing nanowire diameter, interpreted using a theoretical model for a LL with many parallel channels. Unfortunately there is not much emphasis on γ^{-1} in this work. In Reference 9 results are shown for a semiconducting polymer in a field effect device yielding $\alpha = 1-8$ depending on the gate voltage, which is interpreted in terms of the multi-channel LL model from Reference 24.

Additionally large values of $\gamma^{-1} = 600-10^4$ are found and interpreted as stemming from many equivalent junctions in series. That is, for N equivalent junctions, the bias voltage across each junction is N^{-1} times the total bias voltage, leading to a correction of the crossover point, i.e. $eV/kT \approx 2\gamma^{-1}$, such that, combined with the result from Reference 23, $\gamma^{-1} \approx N$. In Reference 11 measurements on polymer nanowires are presented, where the full dataset of I - V curves at different temperatures can be described by Equation (1) with $\alpha = \beta + 1$, but fitting the individual I - V curves reveals a temperature dependence $\beta(T) = 1 + \beta_0 T^\nu$, where β_0 and $\nu = 0.2-0.5$ are fit parameters.

The data presented here fits well with the measurements from literature interpreted as stemming from LL behavior. Many measurements yield values of α in or close to the range observed here, i.e. $\alpha = 0.3-1.1$ and $\alpha = \beta + 1$. The trend in α with diameter could be related to the layer thickness dependence on diameter for PEDOT:PSS in the ratios 1:6, 1:12, and 1:20. As conjectured in Chapter 5, at larger diameter corresponding to thinner layers the density of clusters connecting the top to the bottom electrode increases. With this the connections are also likely to consist of more channels and hence have smaller values of α . The lack of a similar strong trend for PEDOT:PSS in the ratio 1:2.5 corresponds to a smaller change in layer thickness with diameter as shown in Figure 2d. Furthermore for PEDOT:PSS in the ratios 1:2.5, 1:6, 1:12, and 1:20 most measurements show moderate values of γ^{-1} , corresponding to typically 10 junctions in series. Curiously there appears to be no relation between γ^{-1} and diameter/layer thickness. Naively one would expect γ^{-1} to increase with layer thickness, given a constant number of junctions per length scale. It could be that the trend is obscured by the scatter in the measurement of γ^{-1} , or that by some mechanism in the complex physics of the percolating network, the number of junctions depends much weaker on the layer thickness. The temperature dependence of β PEDOT:PSS in the ratios 1:2.5 and 1:6, 1:12, and 1:20 is also in good agreement with Reference 11, where the presented data is interpreted as stemming from LL behavior.

The interpretation of PEDOT:PSS type 'ICP1020' in a similar manner as above is difficult. Strangely, despite the constant layer thickness with diameter, α has the same dependence on diameter as for the non-HBS-treated PEDOT:PSS in the ratios 1:6, 1:12, and 1:20. The measured values of γ^{-1} for PEDOT:PSS type 'ICP1020' would indicate as many as 40 to 80 junctions, while the layer thickness has increased roughly a factor 2.5. Furthermore, the temperature dependence of β shows much different behavior than that of the non-HBS treated PEDOT:PSS in

the ratios 1:2.5 and 1:6, 1:12, and 1:20. Interpreting these results is hindered by a lack of knowledge of the microscopic structure of PEDOT:PSS type 'ICP1020'. If indeed this microscopic structure is not consisting of filaments, the interpretation as LL behavior would be incorrect for this PEDOT:PSS type. In that case, however, the observation of the same trend in α with diameter as PEDOT:PSS in the ratios 1:6, 1:12, and 1:20 is difficult to explain.

In summary, the VRH interpretation of the out-of-plane charge transport behavior described by Equation (1) as suggested by Rodin and Fogler¹⁵ can by its definition not explain $\alpha < 4/3$ as experimentally observed. An alternative interpretation in terms of a chain of quantum dots in the Coulomb blockade regime is not able to explain $\gamma^{-1} \neq 0.5$ as experimentally observed.¹³ The LL model can however explain most of the observations except for those of PEDOT:PSS type 'ICP1020', which may have a microstructure that differs from the non-HBS-treated PEDOT:PSS in the ratios 1:2.5 and 1:6, 1:12, and 1:20.

Conclusions

The out-of-plane conductivity vs. bias voltage and temperature for spin coated layers of PEDOT:PSS has systematically been studied by the use of interconnect structures (vias) of varying diameter. Different PEDOT:PSS ratios of 1:2.5, 1:6, 1:12, and 1:20 and an additional HBS-treated PEDOT:PSS type 'ICP1020' have been investigated. The low bias conductivity for these samples is Ohmic and has power law dependence on temperature with exponent α , which varies between 0.3 and 1.1 depending mostly on the via diameter. For most devices the diameter dependence coincides with an increase in layer thickness. Normalizing the I - V curves to $I/T^{\alpha+1}$ vs. eV/kT reveals that for each device they collapse onto a single curve, which is often referred to as universal behavior. At $eV/kT \approx 2\gamma^{-1}$ this single curve crosses over from Ohmic behavior to non-Ohmic behavior described by $I/T^{\alpha+1} \propto (eV/kT)^{\beta}$, with $\beta = \alpha + 1$. Allowing a temperature dependence for β reveals a decreasing trend for β with temperature.

Based on previous knowledge that in the samples of non-HBS-treated PEDOT:PSS in the ratios 1:2.5, 1:6, 1:12, and 1:20 the conductivity is mediated by filaments with a diameter of 4-5 nm, three interpretations of the observed behavior are highly likely, namely in terms of a quasi-1D VRH system with filaments of finite length, in terms of a chain of quantum dots in the Coulomb blockade regime, and in terms of a Luttinger Liquid which describes the quantum state of interacting free

electrons confined to one dimension. Of these three, only the LL-model is found not to contradict the presented measurements for the non-HBS-treated PEDOT:PSS materials. For these, the LL model interprets the increasing trend in α with decreasing diameter and increasing layer thickness as stemming from connections between top and bottom electrode with a decreasing number of parallel channels. The HBS-treated PEDOT:PSS type 'ICP1020' is less accurately described by the LL-model. However this material is difficult to interpret due to a lack of knowledge of its microstructure.

Experimental

PEDOT:PSS emulsions were obtained from AGFA-Gevaert N.V. The emulsion used to prepare the samples is PEDOT:PSS ratio 1:2.5 and is commercially available as ICP-1050. PEDOT:PSS ratios 1:6, 1:12, and 1:20 were prepared using the stock dispersion of PEDOT:PSS in ratio 1:2.5. The PEDOT:PSS ratio was adapted by adding PSS. Where necessary, water was added to obtain a solid content of (0.90 ± 0.04) w%. To obtain homogeneous emulsions we sonicated the solutions. This procedure for preparing the emulsions is the same as used in Chapters 4 and 5. Additionally, as a reference sample, the commercially available PEDOT:PSS material ICP-1020, from the same manufacturer has been used. To this sample 5 vol-% dimethyl sulfoxide (DMSO) was added as a high boiling point solvent.

The out-of-plane conductivity measurements of PEDOT:PSS were performed using the technology previously developed for molecular junctions. The devices were prepared according to the procedure described in Reference 28 and Chapter 5. In the following we will briefly summarize this procedure. For the substrates a 4-inch silicon wafer with a 500 nm thermally grown silicon oxide was used. On this wafer, a 1 nm layer of chromium was thermally evaporated through a shadow mask, followed by 60 nm of gold. The root-mean-square (RMS) roughness of the bottom contact is about 0.7 nm over an area of $0.25 \mu\text{m}^2$. The two terminal junctions were photolithographically defined in an insulating matrix of photoresist, ma-N 1410 (Micro Resist Technology GmbH). After a pre-bake step to remove any remaining solvents, the layer was exposed to UV light with a Karl Süss MA1006 mask aligner to define the vertical interconnects, 'vias', with diameters of 5, 10, 20, 50, and 100 μm . After development the film was hard baked at 200 °C for at least 1 h. The wafer was subsequently cut in several pieces using a diamond tip pen. This allowed the simultaneous processing of different PEDOT:PSS compositions on a

single wafer, thereby eliminating processing variations that can affect device performance. A last step before layer deposition was cleaning of the bottom gold contacts with a PDC plasma cleaner (Harrick plasma) to remove any photoresist residuals. To obtain an equal layer thickness for all PEDOT:PSS ratios, the following spin coat parameters were used. The ramp-rate was 1000 RPM/s and the first spin coating step is 500 RPM for 5 s followed by 120 s of 2000 RPM (for 1:2.5), 1700 RPM (1:6), 1500 RPM (1:12), 1500 RPM (1:20) or 1500 RPM (ICP1020). On planar test substrates these parameters led to layer thicknesses around 40 nm for PEDOT:PSS ratios 1:2.5, 1:6, 1:12, and 1:20 and to a thickness of around 100 nm for the ICP 1020 material. After spin coating, the wafer was then immediately transferred to a vacuum oven to dry the film for at least 1 h. As top electrode, 100 nm of gold was evaporated through a shadow mask. This gold layer, apart from providing electrical contact with the measurement probes, also serves as a self-aligned mask for the removal of redundant PEDOT:PSS by reactive ion etching (O_2 plasma). This step eliminates any parasitic currents from top to bottom electrode.

Measurements were performed in a high-vacuum probe-station (Janis research) at controlled temperatures between 5 and 300 K. Two type of I - V curves have been determined using a Keithley 2636a source-measure unit: (i) non-pulsed bias sweeps between -0.5 V and 0.5 V and (ii) pulsed bias sweeps similar to those in Reference 29, between -2.5 V and 2.5 V with a 0.01 % duty cycle. Measurements often show transient changes, usually as irreversible steps in the conductivity with temperature. The measurements used for analysis were selected to contain no such transient changes.

References

- ¹ N. F. Mott, E. A. Davis, *Electronic Processes in Non-Crystalline Materials*; Oxford University Press, 2012.
- ² B. I. Shklovskii, A. L. Èfros, *Electronic properties of doped semiconductors*; Springer-Verlag, 1984.
- ³ Larkin, A.I., *Sov. Phys. JETP* **1982**, 56, 647.
- ⁴ J. Y. Kim, J. H. Jung, D. E. Lee, J. Joo, *Synth. Met.* **2002**, 126, 311.
- ⁵ J. L. Duvail, P. Rétho, V. Fernandez, G. Louarn, P. Molinié, O. Chauvet, *J. Phys. Chem. B* **2004**, 108, 18552.
- ⁶ A. J. Kronemeijer, I. Katsouras, E. H. Huisman, P. A. van Hal, T. C. T. Geuns, P. W. M. Blom, D. M. de Leeuw, *Small* **2011**, 7, 1593–1598.
- ⁷ Z. Zhou, K. Xiao, R. Jin, D. Mandrus, J. Tao, D. B. Geohegan, S. Pennycook, *Appl. Phys. Lett.* **2007**, 90, 193115.
- ⁸ A. N. Aleshin, H. J. Lee, Y. W. Park, K. Akagi, *Phys. Rev. Lett.* **2004**, 93, 196601.
- ⁹ J. D. Yuen, R. Menon, N. E. Coates, E. B. Namdas, S. Cho, S. T. Hannahs, D. Moses, A. J. Heeger, *Nat. Mater.* **2009**, 8, 572.
- ¹⁰ A. J. Kronemeijer, E. H. Huisman, I. Katsouras, P. A. van Hal, T. C. T. Geuns, P. W. M. Blom, S. J. van der Molen, D. M. de Leeuw, *Phys. Rev. Lett.* **2010**, 105, 156604.
- ¹¹ A. Rahman, M. K. Sanyal, *J. Phys. Condens. Matter* **2010**, 22, 175301. The parameter denoted as β in used by Rahman et al. equals $\beta-1$, with β the parameter used in this article.
- ¹² V. V. Deshpande, M. Bockrath, L. I. Glazman, A. Yacoby, *Nature* **2010**, 464, 209.
- ¹³ J.-F. Dayen, T. L. Wade, G. Rizza, D. S. Golubev, C.-S. Cojocaru, D. Pribat, X. Jehl, M. Sanquer, J.-E. Wegrowe, *Eur. Phys. J. Appl. Phys.* **2009**, 48, 10604.
- ¹⁴ M. M. Fogler, S. V. Malinin, T. Nattermann, *Phys. Rev. Lett.* **2006**, 97, 096601.
- ¹⁵ A. S. Rodin, M. M. Fogler, *Phys. Rev. Lett.* **2010**, 105, 106801.
- ¹⁶ C. S. Suchand Sangeeth, M. Jaiswal, R. Menon, *J. Phys. Condens. Matter* **2009**, 21, 072101.
- ¹⁷ A. Aleshin, R. Kiebooms, R. Menon, A. J. Heeger, *Synth. Met.* **1997**, 90, 61.
- ¹⁸ Larkin, A.I., Khmel'nitskii, D.E. *Sov. Phys. JETP* **1982**, 56, 647.
- ¹⁹ M. Bockrath, D. H. Cobden, J. Lu, A. G. Rinzler, R. E. Smalley, L. Balents, P. L. McEuen, *Nature* **1999**, 397, 598. The γ used by Bockrath *et al.* is a factor of 2 smaller than the γ in Equation (1) presented here.
- ²⁰ In the Ohmic limit, i.e. $eV/kT \rightarrow 0$ the current density is described by: $J/T^{1+\alpha} = J_0\gamma \left| \Gamma((1+\beta)/2) \right|^2 (eV/kT)$, and in the non-Ohmic limit, i.e. $eV/kT \rightarrow \infty$ the current density is described by: $J/T^{1+\alpha} = J_0\pi^{1-\beta} (\gamma eV/kT)^\beta$. These functions intersect at $eV/kT = \gamma^{-1}\pi \left| \Gamma((1+\beta)/2) \right|^{2/(\beta-1)}$ which varies between $eV/kT = 2.0\gamma^{-1}$ and $eV/kT = 2.5\gamma^{-1}$ for the values of α measured in this article, i.e. between $\beta = 1.3$ and $\beta = 2.1$.
- ²¹ M. Bockrath, W. Liang, D. Bozovic, J. H. Hafner, C. M. Lieber, M. Tinkham, H. Park, *Science* **2001**, 291, 283.
- ²² F. D. M. Haldane, *J. Phys. C* **1981**, 14, 2585.
- ²³ C. L. Kane, M. P. A. Fisher, *Phys. Rev. Lett.* **1992**, 68, 1220.
- ²⁴ L. Venkataraman, Y. S. Hong, P. Kim, *Phys. Rev. Lett.* **2006**, 96, 076601. The γ used by Venkataraman *et al.* is a factor of 2 smaller than the γ in Equation (1) presented here and β

used by Venkataraman *et al.* is equal to β^{-1} with β the parameter used in Equation (1) presented here.

²⁵ A. C. Bleszynski, F. A. Zwanenburg, R. M. Westervelt, A. L. Roest, E. P. A. M. Bakkers, L. P. Kouwenhoven, *Nano Lett.* **2007**, *7*, 2559.

²⁶ Reference 13 does not make explicit statements about γ^{-1} , instead by combining Equations (5) and (6) of Reference 13 to determine the intersection between the Ohmic and the non-Ohmic part, and using Reference 20, it can be calculated that $\gamma^{-1} \approx 0.5$.

²⁷ J. M. Luttinger, *J. Math. Phys.* **1963**, *4*, 1154.

²⁸ I. Katsouras, V. Geskin, A. J. Kronemeijer, P. W. M. Blom, D. M. de Leeuw, *Org. Electron.* **2011**, *12*, 857.

²⁹ I. Katsouras, A. J. Kronemeijer, E. C. P. Smits, P. A. van Hal, T. C. T. Geuns, P. W. M. Blom, D. M. de Leeuw, *Appl. Phys. Lett.* **2011**, *99*, 013303.

Summary

The Influence of Structure on the Electronic Properties of π -Conjugated Systems

Cell-phones, computers, displays and lighting are an important part of everyday life. To increase the efficiency, functionality and to reduce production costs of these devices, the development of new functional electronic materials is essential. Carbon-based materials have the potential to provide many of the needed functionalities. That is, organic chemistry is able to provide a large number of different molecules consisting of primarily carbon which offer tunable electronic properties. This way, molecules can be used to make organic light emitting diodes (OLEDs) for lighting and displays, organic solar cells for energy harvesting and even micro electrical mechanical systems (MEMS) that tell your smart phone which side is up. Carbon can also be grown in single layers called graphene. Graphene offers the potential of high-speed logic and may be the basis of completely new types of switching devices such as (pseudo)-spintronic devices.

The key to creating functional electronic materials from carbon is getting the right structure. Therefore this thesis focusses on the influence of the structure on the electronic properties of π -conjugated systems (i.e. graphene, electronic functionalized molecules, etc.). In the first part of this thesis this influence is studied for a graphene layer grown on silicon carbide (SiC), in which the graphene/SiC interface has a strong influence on the electronic properties, and for the formation of a graphene layer by decomposing C₆₀ on a Pt(111) surface, where the exact process of decomposition results in a particular graphene/Pt(111) interface structure. The second part of this thesis deals with the polymer system poly(3,4-ethylenedioxy-thiophene):poly(styrenesulfonate) (PEDOT:PSS). PEDOT:PSS is a transparent conducting material which can be used in OLEDs and organic solar cells, where it is typically applied by spin coating from emulsion. Here PEDOT and PSS are found to form filaments, resulting in a spaghetti-like

morphology of the spin cast layer, which has important consequences for the charge transport.

In Chapter 2, graphene grown by thermal decomposition of SiC is studied by atomically resolved scanning tunneling microscopy and spectroscopy (STM/STS). At small bias voltages STM images reveal the graphene lattice structure, as expected. However, at increased bias voltages bright features are revealed which, by comparing STS to angular resolved photo emission spectroscopy (ARPES), are shown to be localized states of the interface layer between the graphene and the SiC. Additionally, close to structural defects in the graphene layer a giant inelastic tunneling process, caused by electron-phonon coupling, is observed. This process accounts for half the total tunneling current. A map of this inelastic current shows that these inelastic contributions are strongest at the localized states of the interface layer. Therefore it is expected that the localized states of the interface layer have an important yet complicated influence on the electronic properties of graphene on SiC.

In Chapter 3, the full pathway from room temperature deposition of C_{60} on Pt(111) to the formation of graphene at high temperatures is presented. Using in-situ low temperature STM, a submonolayer of C_{60} on Pt(111) is studied after heating steps at increasing temperatures. We are able to identify the molecular orientations of the C_{60} molecules at each step. Changes in the apparent height of C_{60} molecules in combination with a change in their orientation show that C_{60} molecules adopt a subsurface missing-atom configuration. By studying the graphene layer formed upon an additional high temperature heating step, both by STM and by density functional theory (DFT) calculations, we show that $\sqrt{3} \times \sqrt{3} R30^\circ$ domains of the formed graphene layer are also in a subsurface missing-atom configuration. It is shown that the transition toward the subsurface missing-atom configuration takes place at the edges of C_{60} islands and could be assisted by the instability of the Pt(111) surface.

In Chapter 4, the mechanism and magnitude of the in-plane conductivity of PEDOT:PSS thin films is determined using temperature dependent conductivity measurements for various PEDOT:PSS weight ratios. For all studied weight ratios the conductivity of PEDOT:PSS is well described by quasi 1D variable range hopping (VRH). The experimentally determined conductivity varies over three orders of magnitudes and follows a power law with power 3.5 as a function of the weight fraction of PEDOT in PEDOT:PSS in the range 0.04–0.3. Analysis of the

field dependent conductivity shows a behavior that is consistent with quasi-1D VRH. Combined, these observations suggest that conductance takes place via a percolating network of quasi-1D filaments. Using transmission electron microscopy (TEM) filamentary structures are indeed observed both in vitrified solutions and in dried films. For PEDOT:PSS films that were processed with a high boiling solvent, the temperature dependence of the Ohmic conductivity suggests a quasi-1D VRH system, but the low characteristic temperature indicates that the system is close the critical regime between a metal and an insulator. In this case, the conductivity scales linearly with the weight fraction of PEDOT in PEDOT:PSS, indicating the conduction is no longer limited by a percolation of filaments. The lack of observable changes in TEM upon addition of the high boiling solvent suggests that the changes in conductivity are due to a smaller spread in the conductivities of individual filaments, or a higher probability for neighboring filaments to be connected, rather than being due to morphological modification of the filaments.

In Chapter 5, the room temperature out-of-plane conductivity of spin coated PEDOT:PSS films is studied. Although important for its application as transparent conductor in light emitting and photovoltaic devices, studies to the conductivity of PEDOT:PSS rarely address the out-of-plane conductivity and those that do report widely varying results. In the presented experiment, the out-of-plane charge transport in thin films of PEDOT:PSS is systematically studied by varying its composition. To this end, small vias between metallic contacts are used. An unexpected, but strong dependence of the conductivity on via diameter is observed. The change in conductivity correlates with a diameter dependent change in PEDOT:PSS layer thickness. The more than three orders of magnitude variation in out-of-plane conductivity with only a 3-4-fold layer thickness variation can quantitatively be explained on basis of a percolating cluster model. This model describes the probability for conductive paths between the top and bottom electrode to be formed from randomly placed conductive elements in an insulating matrix, and shows that for thin layers this probability strongly decreases with increasing layer thickness. The results also rationalize previously unexplained findings in molecular junctions where PEDOT:PSS is used as contact electrode.

In Chapter 6, the out-of-plane conductivity of spin coated PEDOT:PSS films is studied for varying temperatures, electric fields and composition. Recent measurements of the out-of-plane conductivity of PEDOT:PSS, and of the conductivity of a semiconducting polymer in a field effect device reveal a curious

power law dependence of the conductivity on field and temperature in both the Ohmic and non-Ohmic regimes. This is referred to as universal scaling. Connecting this behavior to a particular microscopic model has proven to be difficult. Here we have performed a systematic study of the temperature and bias voltage dependence of the out-of-plane conductivity of PEDOT:PSS through the use of interconnect structures (vias) for varying via diameters and various PEDOT:PSS formulations. The measurements indeed show universal scaling. By use of explicit knowledge of the microscopic structure of the used PEDOT:PSS materials the number of possible underlying models can be narrowed down to only three models: a model for finite size effects in quasi one-dimensional variable range hopping, a model for a chain of quantum dots in the Coulomb blockade regime and a model for connected Luttinger liquids. The presented measurements seem at odds with all but the latter model.

Summarizing, this thesis characterizes the relationship between the electronic properties of π -conjugated systems and their structural properties for two systems, graphene and PEDOT:PSS. For graphene, this is shown for two individual cases, one discusses the influence of localized states of an interface layer below graphene on SiC, the other discusses the formation of a missing atom interface structure of the Pt(111) surface below a graphene layer. The second part of this thesis presents a concerted effort studying the charge transport properties of PEDOT:PSS. Starting from its structure, which is found to consist of a random (percolating) network of filaments, a very complete set of measurements could be accurately described. This includes the in- and out-of-plane conductivity of PEDOT:PSS as a function of temperature, electric field and PEDOT:PSS ratio. The uncovered filamentary structure differs from the current literature which typically describes PEDOT:PSS as consisting of grains with a PEDOT-rich core and PSS-rich shell. Given the lower percolation threshold for filaments than for grains, filamentary PEDOT:PSS is likely to have a higher conductivity than grain-like PEDOT:PSS. It is therefore not unlikely that with the efforts to increase the conductivity of PEDOT:PSS, changes have been made in the synthesis of commercial PEDOT:PSS to produce filamentary instead of grain-like PEDOT:PSS. The presented model for the conductivity of PEDOT:PSS offers a good starting point for further rational optimization of the properties of PEDOT:PSS.

Samenvatting

Mobiele telefoons, computers, beeldschermen en verlichting spelen een belangrijke rol in het dagelijkse leven. Om de efficiency en functionaliteit van deze apparaten te verbeteren en om de productiekosten terug te brengen is het ontwikkelen van nieuwe functionele elektronische materialen essentieel. Op koolstof gebaseerde materialen hebben de potentie om in veel van de nodige functionaliteiten te voorzien. Dat wil zeggen, met organische chemie is het mogelijk een groot aantal verschillende moleculen te vervaardigen die voornamelijk uit koolstof bestaan en waarvan de elektronische eigenschappen aanpasbaar zijn. Op deze manier kunnen moleculen gebruikt worden om organische lichtemitterende diodes (OLEDs) te maken voor gebruik in verlichting en beeldschermen, om organische zonnecellen te vervaardigen voor energieomzetting en om micro-elektronische mechanische systemen (MEMS) te vervaardigen die bijvoorbeeld een smart phone vertellen welke kant boven is. Koolstof kan ook als een enkele laag grafeen gegroeid worden. Grafeen zou de basis kunnen zijn voor logische schakelingen met hoge verwerkingssnelheid en zou eveneens de basis kunnen vormen van geheel nieuwe types van apparaten zoals (pseudo-)spintronische schakelaars.

De truc om functionele elektronische materialen uit koolstof te vervaardigen is het verkrijgen van de juiste structuur. Daarom focust deze thesis zich op de invloed van structuur op de elektronische eigenschappen van π -geconjugeerde materialen (d.w.z. grafeen, gefunctionaliseerde moleculen, etc.). In het eerste deel van dit proefschrift wordt dit onderzocht voor een enkele grafeenlaag gegroeid op siliciumcarbide (SiC). In dit systeem heeft het grafeen/SiC grensooppervlak sterke invloed op de elektronische eigenschappen van het grafeen. Eveneens wordt grafeen bestudeerd dat gevormd wordt door het ontbinden van C_{60} moleculen op een Pt(111) oppervlak. Hierbij zorgen de eigenschappen van het proces van het ontbinden van de C_{60} moleculen voor een bijzonder grafeen/Pt(111) grensooppervlak. In het tweede deel van deze thesis wordt het polymeersysteem poly(3,4-ethyleendioxythiofeen):poly(styreen-sulfonaat) (PEDOT:PSS) behandeld. PEDOT:PSS is een transparant geleidend materiaal dat gebruikt wordt in OLEDs en organische zonnecellen, waarin het typisch wordt aangebracht middels een

proces dat spin coating heet. We vinden dat in dit materiaal PEDOT en PSS samen filamenten vormen, wat resulteert in een spaghetti-achtige morfologie van de gevormde laag. Deze morfologie heeft belangrijke consequenties voor het ladingstransport.

In Hoofdstuk 2 wordt grafeen, gegroeid door de thermische ontbinding van SiC, onderzocht met behulp van *scanning-tunneling microscopy* en *spectroscopy* (STM/STS). Bij lage voltages laat STM zoals verwacht de roosterstructuur van grafeen zien. Bij hogere voltages laat STM echter stippen zien die door hun STS respons te vergelijken met *angular resolved photo emission spectroscopy* (ARPES) geïdentificeerd kunnen worden als gelokaliseerde toestanden uit de grenslaag tussen het SiC en het grafeen. Tevens wordt in de buurt van structurele defecten in de grafeenlaag een gigantisch inelastisch tunnelproces waargenomen dat veroorzaakt wordt door elektron-phonon koppeling. Dit proces kan een inelastische stroom tweeweg brengen met een grootte van de helft van de totale tunnelstroom. Door de intensiteit van deze inelastische stroom plaatsopgelost te bepalen wordt aangetoond dat de inelastische bijdragen aan de tunnelstroom het sterkst zijn in de buurt van de gelokaliseerde toestanden uit de grenslaag. Hierdoor is de verwachting dat de gelokaliseerde toestanden uit de grenslaag een belangrijke, doch gecompliceerde, invloed hebben op de elektronische eigenschappen van grafeen op SiC.

In Hoofdstuk 3 wordt het volledige, thermisch-gedreven omvormingsproces van bij kamertemperatuur gedeponeerde C_{60} moleculen op Pt(111) tot grafeen gepresenteerd. Gebruikmakend van *in-situ* lage-temperatuur STM wordt een sub-monolaag van C_{60} op Pt(111) onderzocht na het toepassen van verhittingsstappen bij steeds hogere temperaturen. Bij iedere stap is het gelukt de moleculaire oriëntaties van de C_{60} moleculen te identificeren. Veranderingen in de met STM bepaalde hoogtes van de C_{60} moleculen in combinatie met een verandering in oriëntatie laat zien dat de C_{60} moleculen een configuratie aannemen met een missend atoom onder het oppervlak. Door het bestuderen van het grafeen dat is gevormd bij een laatste verhittingsstap op zeer hoge temperatuur, met zowel STM als met dichtheidsfunctionaal-theorie (DFT) berekeningen, laten we zien dat de $\sqrt{3}\times\sqrt{3}R30^\circ$ domeinen van het gevormde grafeen tevens een configuratie aannemen met een missend atoom onder het oppervlak. Er wordt aangetoond dat de formatie van de onder-het-oppervlak-missend-atoom-configuratie plaatsvindt aan de randen van C_{60} eilanden en dat het goed mogelijk is dat een instabiliteit van het Pt(111) oppervlak deze formatie mogelijk maakt.

In Hoofdstuk 4 worden het mechanisme en de grootte van de in-het-vlak gemeten geleiding van dunne lagen PEDOT:PSS bepaald als functie van temperatuur voor PEDOT:PSS in verschillende gewichtsverhoudingen. De gemeten geleidingen van alle onderzochte PEDOT:PSS gewichtsverhoudingen kunnen zeer goed verklaard worden middels quasi-1D *variable range hopping* (VRH) theorie. De experimenteel bepaalde geleiding varieert met drie ordes van grootte en gedraagt zich als de gewichtsfractie PEDOT tot de macht 3,5, waarbij de gewichtsfractie tussen de 0,04 en 0,3 ligt. Een analyse van de veldafhankelijkheid van de geleiding laat zien dat deze consistent is met quasi-1D VRH. Bij elkaar suggereren deze observaties dat de geleiding plaatsvindt in een percolerend netwerk van quasi-1D filamenten. Transmissie elektron microscopie (TEM) laat inderdaad filamenten zien, zowel in oplossing als in gedroogde lagen. Voor PEDOT:PSS verwerkt met een hoogkokend oplosmiddel vertoont de temperatuursafhankelijke geleiding nog steeds het gedrag van een quasi-1D VRH systeem, maar duidt de lage karakteristieke temperatuur erop dat het systeem zich dichtbij het kritieke regime tussen een metaal en een isolator bevindt. Voor deze PEDOT:PSS lagen schaalde de geleiding lineair met de gewichtsfractie PEDOT, wat aangeeft dat de geleiding in dit geval niet gelimiteerd is door een percolerend netwerk van filamenten. TEM laat geen significante verschillen zien tussen PEDOT:PSS verwerkt met of zonder hoogkokend oplosmiddel. Dit suggereert dat het verschil in de geleiding niet zozeer optreedt door morfologische veranderingen, maar eerder door een kleinere spreiding in de geleiding van de individuele filamenten, of door een grotere kans dat filamenten met elkaar verbonden zijn.

In Hoofdstuk 5 wordt de uit-het-vlak geleiding van dunne PEDOT:PSS lagen bestudeerd. Hoewel de uit-het-vlak geleiding belangrijk is voor de toepassing van PEDOT:PSS als transparante geleider in OLEDs en zonnecellen, wordt zij zelden meegerekend in studies naar de geleiding van PEDOT:PSS. De studies die dat wel doen laten een grote spreiding in de resultaten zien. In het hier gepresenteerde experiment wordt de uit-het-vlak geleiding van PEDOT:PSS systematisch onderzocht voor PEDOT:PSS in verschillende gewichtsverhoudingen. Hiertoe wordt de PEDOT:PSS aangebracht in kleine vias met zowel onder als boven een metallisch contact. De geleiding blijkt onverwachts zeer afhankelijk van de diameter van de via te zijn. Deze geleidingsverschillen gaan gepaard met laagdikteverschillen als functie van de viadiameter. De meer dan drie ordes variatie in geleiding bij slechts een drie- a viervoudige laagdikteverandering kan worden

verklaard op basis van een percolatie-clustermodel. Dit model beschrijft dat kans dat willekeurige geplaatste geleidende elementen in een isolerende matrix aaneengesloten paden vormen tussen de bovenste en onderste electrode en laat zien dat voor dunne lagen deze kans sterk afneemt bij toenemende laagdikte. Tevens schept dit een kader om een eerdere meting aan moleculaire juncties te verklaren, waar PEDOT:PSS als contactelektrode is gebruikt.

In Hoofdstuk 6 wordt de uit-het-vlak geleiding van dunne PEDOT:PSS lagen bestudeerd als functie van temperatuur, voltage en de PEDOT:PSS gewichtsverhouding. Recentelijke metingen aan de uit-het-vlak geleiding van PEDOT:PSS lagen evenals metingen aan de geleiding van een halfgeleidend polymeer in een *field effect device* onthullen een opmerkelijk gedrag waarbij de geleiding zich gedraagt als de temperatuur of het voltage tot een zekere macht. Dit geldt voor zowel de Ohmse als de niet-Ohmse regimes. Dit gedrag wordt ook wel universele schaling genoemd. Het blijkt lastig om zulk gedrag toe te schrijven een specifiek microscopisch model. Hiertoe hebben we de temperatuurs- en voltageafhankelijkheid van de uit-het-vlak geleiding van PEDOT:PSS bepaald voor verschillende viadimeters en voor PEDOT:PSS in verschillende gewichtsverhoudingen. Deze metingen laten inderdaad universele schaling zien. Door expliciet gebruik te maken van kennis over de microscopische structuur van het gebruikte PEDOT:PSS kan het aantal modellen dat van toepassing is worden gereduceerd tot drie: een model voor quasi 1D VRH systemen van eindige grote, een model voor een keten van quantum dots in het Coulomb blokkade regime en een model voor aaneengesloten Luttinger liquids (LL). De gemeten resultaten zijn inconsistent met alle behalve het laatste model.

Samengevat wordt in dit proefschrift het verband tussen de elektronische eigenschappen van π -geconjugeerde systemen en hun structuur bestudeerd voor twee systemen, te weten grafeen en PEDOT:PSS. Voor grafeen wordt dit verband onderzocht voor twee gevallen: voor grafeen op SiC, waar de invloed van gelokaliseerde toestanden van de grenslaag onder het grafeen is onderzocht en voor grafeen gevormd uit C₆₀ op Pt(111), waar een bijzondere onder-het-oppervlak-missend-atoom-configuratie is onderzocht. Het tweede deel van dit proefschrift is een uitvoerig onderzoek naar de ladingstransporteigenschappen van PEDOT:PSS. Aan de hand van de morfologie, welke blijkt te bestaan uit een percolerend netwerk van filamenten, kan een erg complete verzameling aan data beschreven worden. Deze verzameling bevat de in- en uit-het-vlak geleiding van PEDOT:PSS als functie van temperatuur, elektrisch veld en PEDOT:PSS gewichtsverhouding. De

ontrafelde morfologie, bestaande uit filamenten, onderscheidt zich van de huidige literatuur waarin PEDOT:PSS doorgaans beschreven wordt als bestaande uit korrels met een PEDOT-rijke kern en een PSS-rijke schil. Aangezien de percolatiedrempel hoger is voor korrels dan voor filamenten, is het waarschijnlijk dat een systeem bestaande uit filamenten een hogere geleiding heeft dan een systeem bestaande uit korrels. Het is daarom niet onwaarschijnlijk dat met de inspanningen om de geleiding van PEDOT:PSS te verbeteren, de commerciële synthese van dit materiaal zo is aangepast dat er filament-achtig in plaats van korrelachtig PEDOT:PSS geproduceerd wordt. Het hier gepresenteerde model kan als een uitgangspunt dienen voor verdere doelgerichte optimalisatie van de eigenschappen van PEDOT:PSS.

Curriculum vitae

Kevin van de Ruit was born on the fifth of September 1982 in Dordrecht. He obtained his pre-university secondary education at the Willem de Zwijger College in Papendrecht in 2000. In the same year he started to study Applied Physics and Applied Mathematics at the Eindhoven University of Technology. He obtained both bachelor degrees in 2006 and obtained his master degree in Applied Physics in 2007. His master thesis describes the influence of the substrate on the electronic properties of graphene grown on silicon carbide. In 2008 he started his PhD research on graphene grown on silicon carbide under the supervision of dr.ir. C.F.J. Flipse in the group Molecular Materials and Nanosystems (M2N) of prof.dr.ir. R.A.J. Janssen. The results of this work are described in chapters 2 and 3 of this thesis. In 2010 he shifted his interest towards studying the charge transport properties of PEDOT:PSS under the supervision of dr.ir. M. Kemerink, also in the group M2N. The results of this work are described in chapters 4, 5, and 6 of this thesis. At present he works as a design engineer, for designing and analyzing overlay tests at ASML in Veldhoven.



List of publications

Kevin van de Ruit, Racheli Itzhak Cohen, Dirk Bollen, Ton van Mol, Rachel Yerushalmi–Rozen, René A. J. Janssen, Martijn Kemerink, Quasi-one dimensional in-plane conductivity in filamentary films of PEDOT:PSS, *submitted to Advanced Functional Materials*.

Kevin van de Ruit, Ilias Katsouras, Dirk Bollen, Ton van Mol, René A. J. Janssen, Dago M. de Leeuw, Martijn Kemerink, The curious out-of-plane conductivity of PEDOT:PSS, *submitted to Advanced Functional Materials*.

Kevin van de Ruit, Ilias Katsouras, Dirk Bollen, Ton van Mol, René A. J. Janssen, Dago M. de Leeuw, Martijn Kemerink, A systematic study to universal scaling of the out-of-plane conductivity of thin films of PEDOT:PSS, *manuscript in preparation*.

A. L. Pinardi, K. van de Ruit, C. F. J. Flipse, J. A. Martín-Gago, The electronic structure of C₆₀ on Pt(111), *manuscript in preparation*

G. Otero, C. González, A. L. Pinardi, P. Merino, S. Gardonio, S. Lizzit, M. Blanco-Rey, K. van de Ruit, C. F. J. Flipse, J. Méndez, P. L. de Andrés, J. A. Martín-Gago, Ordered Vacancy Network Induced by the Growth of Epitaxial Graphene on Pt(111), *Phys. Rev. Lett.* **2010**, *105*, 216102

J. Červenka, K. van de Ruit, C. F. J. Flipse (2010) Giant inelastic tunneling in epitaxial graphene mediated by localized states. *Phys. Rev. B* **2010**, *81*, 205403

J. Červenka, K. van de Ruit, C. F. J. Flipse (2010), Local enhancement of inelastic tunnelling in epitaxial graphene on SiC(0001). *Phys. Status Solidi B* **2010**, *247*, 2992

Dankwoord / Acknowledgements

Doordat de geslaagde experimenten wat oververtegenwoordigd zijn in mijn thesis, lijkt het haast alsof de afgelopen jaren zonder tegenslagen zijn verlopen. In werkelijkheid zijn er echter periodes geweest waarin experimenten om onduidelijke reden faalden, waarin nieuwe resultaten alleen maar tot grotere verwarring leidden en waarin het zeer onduidelijk was hoe het een en ander samen zou komen in een artikel of hoofdstuk. Klaarblijkelijk ben ik over die moeilijke momenten heen gekomen en dat is te danken aan de mensen die mijn project hebben begeleid.

Martijn, zonder jou was dit boekje niet tot stand gekomen. Met jouw positieve instelling en constructieve aanpak is het gelukt om binnen zeer korte tijd mijn promotie op de rails te krijgen. Onder jouw begeleiding was het mogelijk om het project zo te sturen dat ik de dingen kon doen die ik leuk vind en waar ik goed in ben. Vooral je snelle reacties en opbouwende kritiek bij het schrijven hebben mij enorm geholpen. Dank je.

René wil ik bedanken voor zijn kunde om van moeilijke situaties een overzichtelijk geheel te maken en natuurlijk ook voor zijn onstuitbare optimisme. Ook ben ik dankbaar voor de hulp van Kees; zijn grote interesse in diepgaande fysica mij altijd heeft geïnspireerd.

Ook wil ik graag Jose Angel Martin Gago, Dago de Leeuw, Paul Koenraad en Peter Bobbert bedanken voor hun deelname aan mijn commissie.

Daarnaast ben ik mijn collega's enorm dankbaar; dankzij hen heb ik veel gelachen, heb ik interessante discussies gehad, ben ik geweest op dingen die ik eigenlijk toch minder goed wist dan ik dacht en werd ik geholpen met de dingen die zoveel tijd zouden kosten als je ze zelf zou moeten uitvoeren. Als eerste daarin is Erwin, mijn paranimf, oud-huisgenoot, oud-bestuursgenoot en kantoorgenoot. Zijn optimisme en werklust, zelfs op moeilijke dagen, zijn een voorbeeld voor mij. Daarnaast had ik zonder de technische kennis van Gerard Wijers, Wijnand Dijkstra en Marco van der Sluis slechts theoretisch werk kunnen verrichten. Natuurlijk ben ik de andere M2N'ers ook erg dankbaar; Veronique, Sandra, Jiri, Rik, Wijnand, Erik, Siebe, Klara, Marta, Juan, Friso, Marije, Augusta, Stephan, Alexander, Zuhail, Richard, Christian, Niels, Mikhail, Peter, Koen, Stefan, Dimitri, Ron, Jan, Rein, Marco,

Nick, Jos, Seva, Igor, Simon, Andrzej, Yinxin, Dominique, Willem, Alice, Serkan, Joris, Benjamin, Dhritiman, Arpan, Gijs, Tom, Ameneh en Andre, enorm bedankt voor alle hulp en lol de afgelopen jaren.

As important as the help offered to me at my own university was the help I've received at other groups and institutes, for which I am thankful. Ilias Katsouras together with Dago de Leeuw helped me with sample preparation and data interpretation for the out-of-plane measurements on PEDOT:PSS (chapters 5 and 6). Rachel Yerushalmi–Rozen and Cheli Itzhak Cohen provided me with the TEM data confirming the filamentary structure of PEDOT:PSS (chapter 4). Anna Lisa Pinaridi and Jose Angel Martin Gago cooperated with me for the study of the decomposition of C_{60} on Pt(111) (chapter 3). Thomas Seyller, helped to make the work on graphene on SiC possible (chapter 2). Erik van Elferen, Evgenia Kurganova, Uli Zeitler, Mikhail Katsnelson, Serhiy Vasnyov, Raoul van Gastel, Paul van der Schoot, Oleg Kornusikov, Nando Harmsen, Jos Bremmers, Hans Dalderop, Ramon Groote, Bob Jacobs and Joris Keizer have been of great help during many experiments. I also very much enjoyed working with Georg Götz, Ton van Mol and Jo Wilson at the Holst Centre, and Dirk Bollen at AGFA –Geveart.

Ik heb alleen zo ver kunnen komen omdat ik thuis altijd de rust en steun kon vinden die ik nodig had. Dat heb ik natuurlijk te danken aan mijn vader, mijn moeder en mijn zus. In het bijzonder wil ik mijn zus bedanken voor haar rol als paranimf. Met zoveel natuurkundige en didactische kennis aan mijn zijde durf ik die verdediging zeker aan!

Jennifer, dankzij jou kan ik me op moeilijke dagen herinneren dat werk niet het belangrijkste is in mijn leven. Jij bent het lichtpuntje aan het einde van mijn dag. Ik hou van je.

